General Disclaimer

One or more of the Following Statements may affect this Document

- This document has been reproduced from the best copy furnished by the organizational source. It is being released in the interest of making available as much information as possible.

- This document may contain data, which exceeds the sheet parameters. It was furnished in this condition by the organizational source and is the best copy available.

- This document may contain tone-on-tone or color graphs, charts and/or pictures, which have been reproduced in black and white.

- This document is paginated as submitted by the original source.

- Portions of this document are not fully legible due to the historical nature of some of the material. However, it is the best reproduction available from the original submission.

CR-134997

Optimization of Suppression for Two-Element Treatment Liners for Turbomachinery Exhaust Ducts

Final Technical Report

by

General Electric

R.E. Motsinger
R.E. Kraft
J.W. Zwick
S.I. Vukelich

NASA-Lewis

G.L. Minner
K.J. Baumeister

GENERAL ELECTRIC COMPANY

Prepared For

National Aeronautics and Space Administration

NASA Lewis Research Center
Contract NAS 3-18555

1. Report No.	2. Government Accession No.	3. Recipient's Catalog No.
CR-134997		

4. Title and Subtitle	5. Report Date
Optimization or Suppression for Two-Element Treatment Liners for Turbomachinery Exhaust Ducts	April, 1976
	6. Performing Organization Code

7. Author(s)	8. Performing Organization Report No.
R.E. Motsinger, R.E. Kraft, J.W. Zwick, S.I. Vukelich G.L. Minner, K.J. Baumeister	R76AEG256
	10. Work Unit No.

9. Performing Organization Name and Address	11. Contract or Grant No.
General Electric Company Advanced Engineering and Technology Programs Department Aircraft Engine Group Cincinnati, Ohio 45215	NAS3-18555
	13. Type of Report and Period Covered
12. Sponsoring Agency Name and Address	Final Aug 74 - Dec 75
National Aeronautics and Space Administration Washington, D.C. 20548	14. Sponsoring Agency Code

15. Supplementary Notes

Project Manager: Dr. C. Feiler
NASA-Lewis Research Center
Cleveland, Ohio 44135

16. Abstract

Sound wave propagation in a soft-walled rectangular duct with steady uniform flow was investigated at exhaust conditions. An analysis was developed incorporating the solution equations for sound wave propagation in a rectangular duct with multiple longitudinal wall treatment segments and uniform flow. Modal analysis was employed to find the solution equations. The analysis was used to study the effectiveness of a uniform and of a two-sectional liner in attenuating sound power in a treated rectangular duct without flow (M = 0) and with uniform flow of Mach 0.3.

Two-segment liners were shown to increase the attenuation of sound as compared to a uniform liner. The predicted sound attenuation was compared with measured laboratory results for an optimized two-segment suppressor. Good correlation was obtained between the measured and predicted suppressions when practical variations in the modal content and impedance were taken into account.

The analysis was then employed in parametric optimization studies, first, of the effect of the ratio of duct height-to-wavelength, η, on the optimum sound suppression in an acoustically lined rectangular duct and, second, of the effect of variation of liner segment length ratio on optimum sound suppression when the total length of the two-element treatment is kept constant.

17. Key Words (Suggested by Author(s))	18. Distribution Statement
Duct Acoustics Modal Analysis Eigenvalue Treatment Optimization Noise Suppression	Unlimited

19. Security Classif. (of this report)	20. Security Classif. (of this page)	21. No. of Pages	22. Price*
Unclassified	Unclassified	123	

* For sale by the National Technical Information Service, Springfield, Virginia 22151

NASA-C-168 (Rev. 6-71)

TABLE OF CONTENTS

LIST OF ILLUSTRATIONS

LIST OF ILLUSTRATIONS (Continued)

LIST OF ILLUSTRATIONS (Continued)

LIST OF ILLUSTRATIONS (Continued)

LIST OF ILLUSTRATIONS (Concluded)

LIST OF TABLES

SUMMARY

Sound wave propagation in a soft-walled rectangular duct with steady uniform flow was investigated at exhaust conditions. An analysis was developed incorporating the solution equations for sound wave propagation in a rectangular duct with multiple longitudinal wall treatment segments and uniform flow. Modal analysis was employed to find the solution equations. The analysis was used to study the effectiveness of a uniform (one-segment) and of two-sectional liner in attenuating sound power in a treated rectangular duct without flow (M = 0) and with uniform flow of Mach 0.3. The optimization studies were made for a duct height-to-wave length ratio of 1.535 and wall treatment length-to-duct height ratio of 3.43. The optimum predicted sound attenuation was compared with measured laboratory results.

Several two-element treatment configurations were designed to reproduce the optimization conditions and then tested. Good correlation was obtained between the measured and predicted suppressions when practical variations in the modal content and impedance were taken into account. Maximum suppression was found to be very sensitive to the impedance components of the liners: a variation of any one of the normalized resistance or reactance components by $\pm$ 0.1 can lower the predicted peak suppression of 35 dB by 5 to 10 dB.

The analysis was then employed in a series of parametric optimization studies, first, of the effect of the ratio of duct height-to-wavelength, η, on the optimum sound suppression in an acoustically lined rectangular duct and, second, of the effect of variation of liner segment length ratio on optimum sound suppression when the total length of the two-element treatment is kept constant. Two-segment optimized liners were shown theoretically to increase the attenuation of sound as compared to an optimized uniform liner. That suppression increase depends upon the η value, i.e., upon the frequency, and incident source mode distribution. The most practical use of this enhancement occurs over an approximate range of frequency parameter η (H/λ) from 1 to 5. Maximum sound attenuation due to a two-segment liner of a given length depends upon the relative length of the liner segments. Optimum suppression increases with increase from zero to slightly over one in the ratio of the length of the upstream liner segment to that of the downstream segment. Maximum optimized suppression is attained at, or slightly above, the segment length ratio of 1.0; i.e., when the two liner segments are approximately of the same length.

SECTION 1.0

INTRODUCTION

Substantial noise reductions for modern turbofan engines have been accomplished with the use of acoustic treatment, or sound absorbent liners, on the walls of the engine inlet and exhaust ducts. The state of the art of acoustic treatment design has developed to the point where, if further gains are to be achieved, it is necessary to investigate detailed flow duct acoustic phenomena which cause one engine configuration to differ from another. These effects include the nature of noise generation mechanisms, acoustic propagation through flowing air, and the optimization of liner sections, among others. Such phenomena are not susceptible to the empirical approaches which have served to develop past designs. An excellent survey of current jet engine acoustics is presented by Nayfeh, Kaiser, and Telionis[1].*

The basic theory of acoustic propagation in ducts with airflow has been known for sometime, but the correlation of the theory with experiment has been scarce. The emphasis of this study is on the application of modal analysis of wave propagation in ducts, with uniform airflow, to design acoustic liners which are optimized for maximum suppression under a given set of constraints. A design method is developed and the theory is tested by comparing analytically predicted suppressions with measurements made in a laboratory duct.

The model for the theory and experiment was chosen to be a rectangular duct. This simplifies the analysis and allows experimentation under controlled conditions. It is not without practical application, as well, since propagation in a high radius ratio annulus is approximated closely by propagation in a rectangular duct[2]. A major objective of the investigation is to determine how detailed the analysis must be to predict accurately the physical phenomena.

1.1 PROGRAM OBJECTIVES

The primary objective of the program was the analytical and experimental evaluation of the multielement suppressor concept. The evaluations were conducted at conditions of aeroacoustic flowfields representative of engine fan exhaust ducts. The program was accomplished in two major Tasks, Task I being an analytical study and Task II an experimental program.

---

*Superscript numbers refer to references contained in Section 7.0.

1.2 TASK I OBJECTIVES AND SCOPE

The objective of the analytical study in Task I was to develop a method for finding the optimum design of a two-panel-element exhaust duct suppressor employing step discontinuities in the wall impedance, given a set of specific, but arbitrary, initial conditions. The method makes use of the theory of modal propagation with airflow in an acoustically treated rectangular duct; specific conditions for the analytical method are: (1) the duct is two-dimensional, (2) sound propagates with airflow of uniform velocity across the duct, and (3) the sound source consists of a discrete frequency, statistically stationary with time. A further objective was to use the resulting analysis to determine an optimum liner configuration under a specified set of conditions, to build and test the design in a laboratory duct (under Task II), and to compare predicted with the measured suppression results. Finally, the scope of this task included using the analysis in two parametric studies to determine the amount of suppression that can be obtained with two panels having optimized impedance components, one to investigate the effects of the duct-height/wavelength ratio, η, and the other to determine the effect of the ratio of the lengths of the two liner sections.

1.3 TASK II OBJECTIVES AND SCOPE

The objective of the experimental program in Task II was to demonstrate experimentally the optimized treatment design determined in Task I and provide data for correlation with the analysis. The test program was accomplished in two main phases, with a short preliminary test preceding both of these.

Prior to the initiation of the parametric design optimization in Task I, it was necessary to measure the modal source characteristics of the duct under the optimization conditions. This was accomplished in a preliminary duct test in a hardwall configuration.

Upon completion of the design optimization in Task I, the Phase I test program was initiated. Six treatment panel hardware designs were determined which would "bracket" the desired impedance components. These configurations were then tested in the duct for third octave transmission loss over a wide range of frequencies and for narrowband transmission loss at the design frequency. The treatment configuration showing the best suppression was then subjected to detailed modal measurements.

The objective of the Phase II test program was to improve upon the results of the Phase I testing, based on evaluation of the Phase I test results. This led to an analytical reoptimization based on revised source modal characteristics and test of the revised design. In addition, such effects as sensitivity to source modal characteristics and wall impedance were investigated in detail as part of Phase II.

SECTION 2.0

ANALYSIS

Starting with the wave equation in Cartesian coordinates, modal analysis is employed to find the solution for the wave propagation in a soft-walled, multisectional rectangular duct with flow.

2.1 BASIC EQUATIONS

The sound field in a homogeneous medium with uniform steady flow is described by the following linearized wave equation[3].

$$\nabla^2 p = \frac{1}{c^2}\frac{\partial^2 p}{\partial t^2} + \frac{2M}{c}\frac{\partial^2 p}{\partial x \partial t} + M^2 \frac{\partial^2 p}{\partial x^2} \qquad (1)$$

where

∇^2 = the Laplacian operator

$p(x,z,t)$ = the acoustic pressure

c = the speed of sound

M = uniform steady flow Mach number in the positive axial direction, z

Two-dimensional duct geometry is assumed, i.e., the rectangular duct is modelled in two dimensions as shown in Figures 1 and 2 for a single acoustic treatment segment. The sound pressure waves enter the treated portion of the duct at z = 0 and propagate in the positive z-direction. A positive flow Mach number indicates steady uniform flow in the positive z-direction and thus simulates exhaust conditions. A negative Mach number indicates flow opposite to that of the propagation of sound, i.e., simulates inlet conditions.

The elimination of time dependence, which is assumed to be of the form $e^{-i\omega t}$, yields the two-dimensional, time-independent wave equation.

$$(1-M^2)\frac{\partial^2 p}{\partial z^2} + i\,(2kM)\frac{\partial p}{\partial z} + \frac{\partial^2 p}{\partial x^2} + k^2 p = 0 \qquad (2)$$

where

x and z are Cartesian coordinates (See Figure 1)

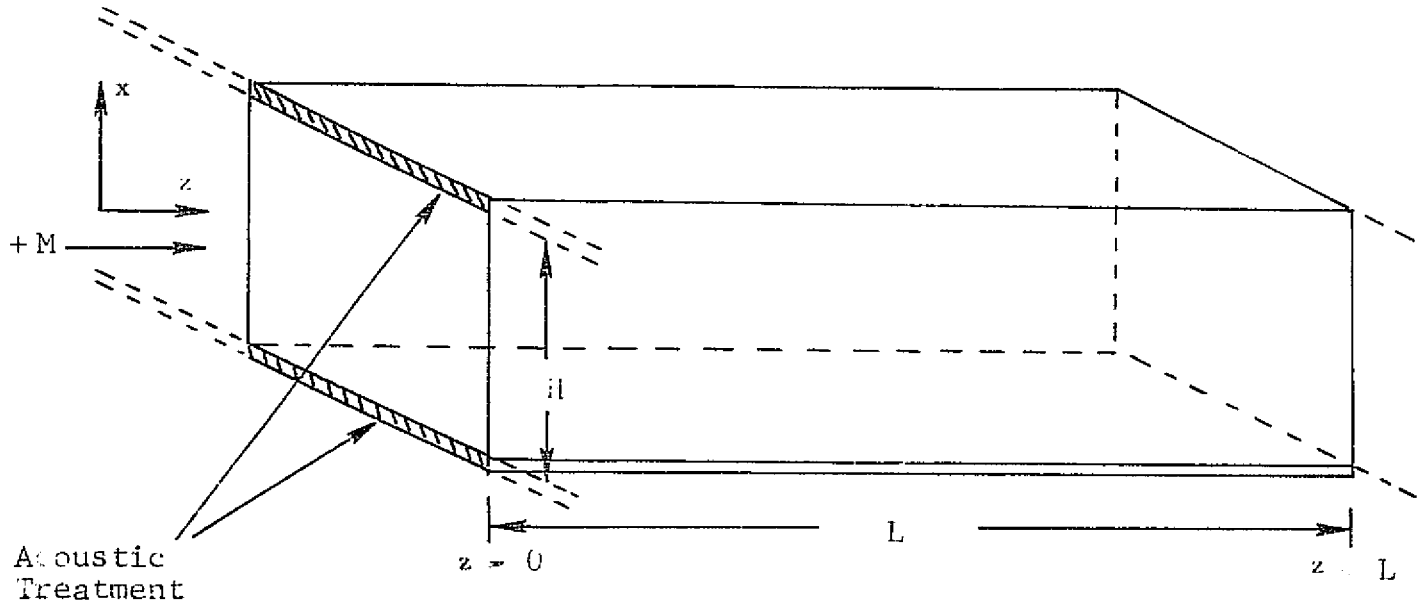

Figure 1. Semi-Infinite Rectangular Duct Geometry.

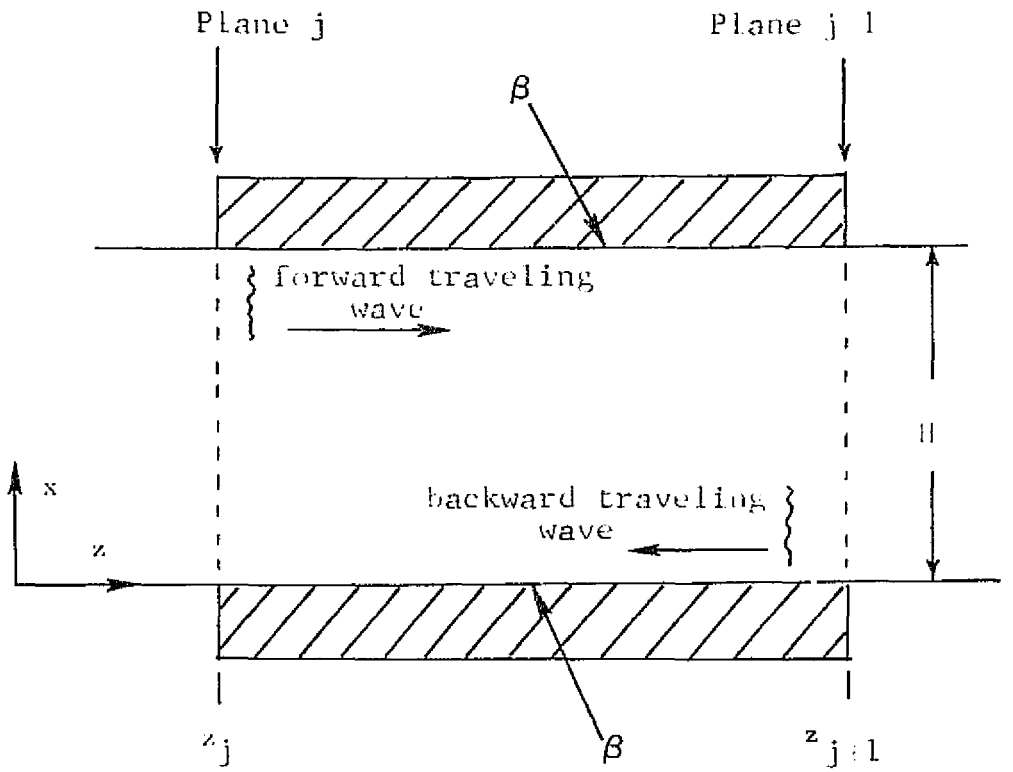

Figure 2. Geometry of Duct Section.

$k = \frac{\omega}{c}$ is the wave number in free space

$\omega = 2\pi f$ is the angular frequency

f = frequency, Hz.

The solution of Equation 2 for the m-th mode of the acoustic pressure in a single uniform duct section is given by the sum of the incident and reflected waves for that mode, i.e.,

$$p_m(x,z) = \left[A_m^{+j} \; e^{j\kappa_m^{+}(z-z_j)} \; \phi_m(\gamma_m^{+} \frac{x}{H}) + A_m^{-(j+1)} \; e^{i\kappa_m^{-}(z-z_{j+1})} \phi_m(\gamma_m^{-} \frac{x}{H}) \right] \qquad (3)$$

The first term in the brackets represents the forward traveling (incident) wave, while the second one is the backward traveling (reflected) wave. The + sign on the superscripts refers to the former, the - sign is associated with the latter.

The spatial part of the complete solution for the acoustic pressure is the sum of the characteristic solutions

$$p(x,z) = \sum_{m=1}^{NM} \left[A_m^{+j} \; e^{j\kappa_m^{+}(z-z_j)} \; \phi_m(\gamma_m^{+} \frac{x}{H}) + A_m^{-(j+1)} \; e^{i\kappa_m^{-}(z-z_{j+1})} \phi_m(\gamma_m^{-} \frac{x}{H}) \right] \qquad (4)$$

where

x = the transverse distance

γ_m = transverse mode eigenvalue

m = transverse mode number

NM = number of transverse modes in the expansion

j, j+1 = axial station indices

H = duct height

A_m = modal expansion coefficient

ϕ_m = eigenfunction for the m-th mode

$\pm$ = superscipt signs denoting the direction of wave propagation

The axial propagation constants $\kappa^{\pm}$ for the forward and backward propagating mode m are related to the flow Mach number M and transverse eigenvalues $\gamma_m^{\pm}$ by

$$\kappa_m^{\pm} = k \left[\frac{-M \pm \sqrt{1 + (M^2 - 1)\left(\frac{\gamma_m^{\pm}}{kH}\right)^2}}{1-M^2} \right] \tag{5}$$

The normalized symmetric modes are given by

$$\phi_m(x) = \frac{(1+\cos \gamma_m) \cos(\gamma_m \frac{x}{H}) + \sin \gamma_m \sin(\gamma_m \frac{x}{H})}{\sqrt{H(1+\cos\gamma_m)\left(1+\frac{\sin\gamma_m}{\gamma_m}\right)}} \tag{6}$$

and the normalized antisymmetric modes are given by

$$\phi_m(x) = \frac{-(1-\cos \gamma_m) \cos(\gamma_m \frac{x}{H}) + \sin \gamma_m \sin(\gamma_m \frac{x}{H})}{\sqrt{H(1-\cos\gamma_m)\left(1-\frac{\sin\gamma_m}{\gamma_m}\right)}} \tag{7}$$

The expressions in the denominators of Equation 6 and 7 are the normalization factors obtained from the integral

$$CNORM_m = \int_0^H p_m^2(x)\, dx \tag{8}$$

For symmetric modes, it yields

$$CNORM_m = \sqrt{H(1 + \cos\gamma_m)(1 + \sin\gamma_m/\gamma_m)} \tag{9}$$

and for antisymmetric modes

$$CNORM_m = \sqrt{H(1 - \cos\gamma_m)(1 - \sin\gamma_m/\gamma_m)} \tag{10}$$

The eigenvalues γ_m and the eigenvectors are determined from the wall boundary conditions which can be expressed in terms of impedance ratios or admittance ratios.

The boundary condition to be satisfied by the symmetric modes is

$$\beta kH = \frac{i\gamma_m^{\pm}}{\left(1-M\frac{\kappa_m^{\pm}}{k}\right)^n} \quad \frac{1 - \cos\gamma_m^{\pm}}{\sin\gamma_m^{\pm}} \tag{11}$$

and by the antisymmetric modes is

$$\beta kH = \frac{-i\gamma_m^{\pm}}{\left(1-M\frac{\kappa_m^{\pm}}{k}\right)^n} \quad \frac{1 + \cos\gamma_m^{\pm}}{\sin\gamma_m^{\pm}} \tag{12}$$

where,

β is the duct wall admittance ratio (based on the $e^{-i\omega t}$ time periodicity).

n = exponent depending on the type of boundary condition

We set n = 1 for the particle velocity continuity wall boundary condition

and n = 2 for particle displacement continuity wall boundary condition.

2.2 RECTANGULAR DUCT EIGENVALUE DETERMINATION

The determination of the transverse eigenvalues requires finding the roots of two complex transcendental Equations, (11) and (12). This can be done by graphical or analytical methods. The mapping of the variable βkH in the complex eigenvalue plane for symmetric and antisymmetric modes, at Mach number M = 0.0, is shown in Figures 3 and 4, respectively.

For every (physically possible) value of βkH there is a corresponding sequence of symmetric and antisymmetric eigenvalues. Each eigenvalue

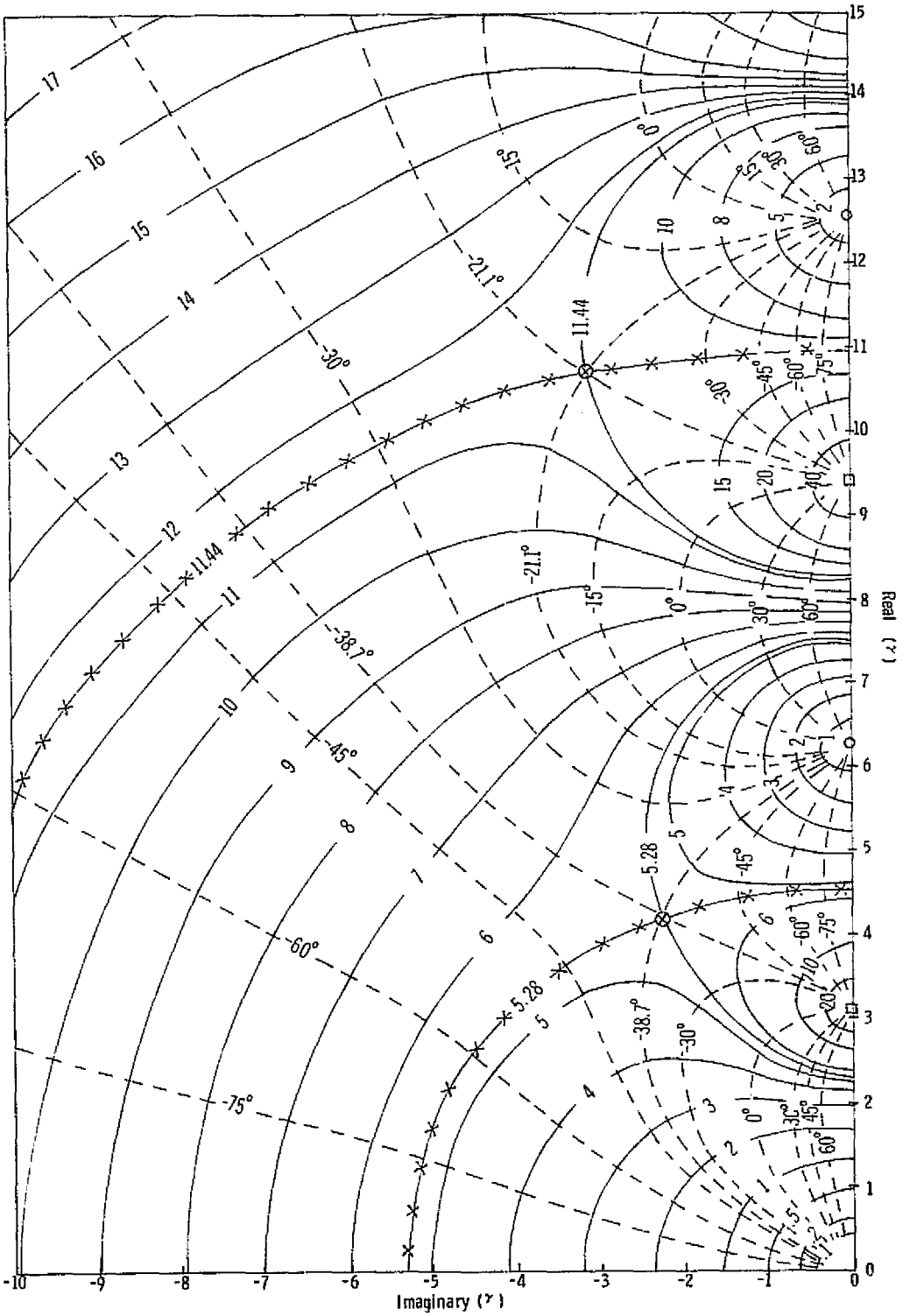

Figure 3. Complex Admittance-Eigenvalue Contour Mapping for Symmetric Modes in a Rectangular Duct at Mach 0.0. Solid Lines are Constant Magnitude βkH, Broken Lines are Constant Phase βkH. Assumes $e^{-i\omega t}$ Time Dependance.

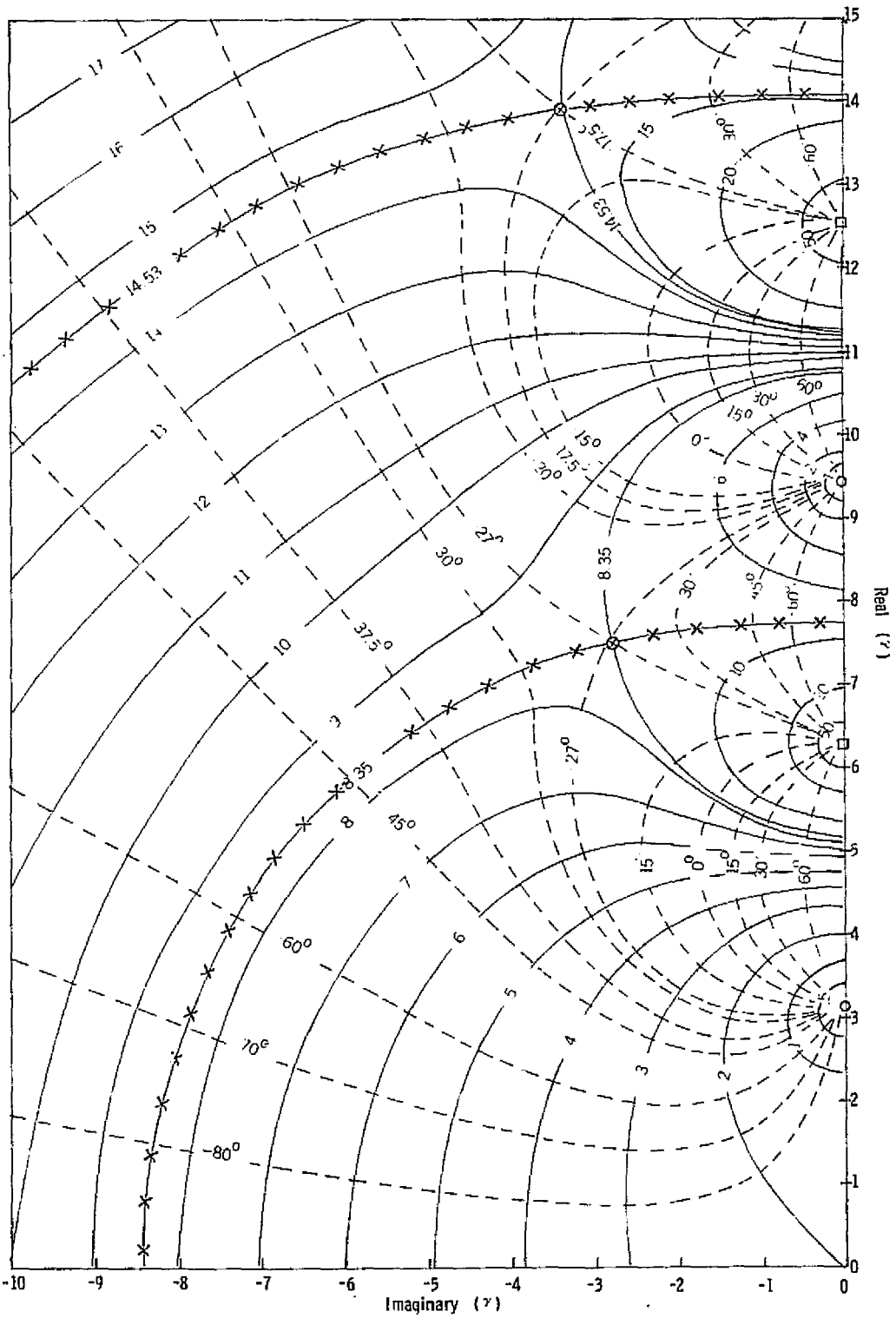

Figure 4. Complex Admittance-Eigenvalue Contour Mapping for Anti-symmetric Modes in a Rectangular Duct at Mach 0.0. Solid Lines are Constant Magnitude βkH, Broken Lines are Constant Phase βkH. Assumes $e^{-i\omega t}$ Time Dependance.

in the sequence falls within one of the regions delineated by the cross-hatched lines separating the mode orders. While for Mach 0.0 the map applies to all kH values, for Mach numbers different from zero a separate mapping is required for each Mach number and every value of kH.

The roots of Equations (11) and (12) are determined analytically by employing an iteration procedure referred to as Bailey's iteration method[4].

Given an estimate γ_j of a root of the equation

$$F(\gamma_j) = 0 \tag{13}$$

Bailey's iterative formula for computing a refined approximation γ_{j+1} of the root from the approximation γ_i is

$$\gamma_{j+1} = \gamma_j - \left[\frac{F(\gamma_j)}{F'(\gamma_j) - \frac{F(\gamma_j)F''(\gamma_j)}{2F'(\gamma_j)}} \right] \tag{14}$$

where j is the iteration index, and the primes denote derivatives with respect to γ.

Bailey's method is similar to the more familiar Newton-Raphson iteration technique but it has a higher order of convergence, i.e., it converges at a faster rate than the former.

The success of an iteration scheme such as this is measured by its ability to rapidly converge to the correct eigenvalues. In the present case the eigenvalues are multivalued functions of the wall admittance and the convergence to the correct root is critically dependant upon the assumed initial value of the root at the start of the iteration. In the past, it has been customary to start the iteration from the sequence of hard wall roots on the real axis of the complex eigenvalue plane. Although these initial values start in the correct modal regions, there is no guarantee that the iteration path of convergence will not cross a branch cut separating modal regions. This may lead to double eigenvalues and/or missed eigenvalues, since the technique always converges to the eigenvalue nearest to the starting point, regardless of the branch cuts.

It is important that the eigenvalue routine be as accurate as possible in a program used as an optimization design tool, particularly when many cases are to be run in succession. A special effort was therefore made to develop an eigenvalue routine free of problems usually encountered in programs of this type.

The adopted procedure consists of dividing the modal regions in the eigenvalue mapping plane into subregions, and choosing an initial value for each mode in the appropriate subregion. The subregion boundaries are either lines of constant magnitude of βkH or lines of constant phase of βkH. Typical examples of the partitioning and initial values are shown in Figures 5 and 6 for the lower part of the symmetric and antisymmetric mode planes. Using these initial values, the iteration procedure is then performed at $M = 0$ until convergence criteria are met. For a nonzero Mach number, the Mach number is then increased from zero to its final value in small increments, using the converged eigenvalues from the previous Mach number as initial values in the next step. This is done for both positive and negative Mach numbers at the same time, since the respective eigenvalues are needed for both forward and backward traveling waves.

The assumption used in the above procedure is that the eigenvalues shift continuously as a function of Mach number. Results of the program and previous experience in modal mapping appear to confirm this continuity even though the mapping of cases with the flow may be different from the $M = 0$ case, particularly for low values of kH and continuity of particle displacement boundary condition. Checkout of the eigenvalue routine for several βkH values and flow Mach numbers has indicated it to be a reliable, accurate, and rapidly convergent calculation. It is not infallible, however, and certain combinations of parameters may still cause convergence problems. Since the accuracy of the solution is very sensitive to the eigenvalues, each case must individually be checked for convergence or the occurrence of double eigenvalues.

2.3 DUCT SOURCE DETERMINATION

The duct propagation analysis requires knowledge of the pressure modal distribution over at least one plane in the duct. The complex modal coefficients must be obtained, such that they contain both relative phase and magnitude information.

If it is desired to compare the results of the program with a rectangular flow duct experiment, it is necessary to perform a modal measurement at the planes designated as source planes. This consists of measuring acoustic pressure cross-spectra between a stationary reference microphone and a microphone which can be traversed across the duct. The cross-spectral density, at a given frequency, as a function of distance across the duct, is then expanded in duct modes as

$$S(\omega,x) = \sum_{j=1}^{NM} \left[A_j^+ \phi_j (\gamma_j^+ \frac{x}{H}) + A_j^- \phi_j (\gamma_j^- \frac{x}{H}) \right] \qquad (15)$$

If the modal measurement is performed over a hardwall section of the duct, the forward and backward eigenvalues are the same, so that Equation (15) can be written

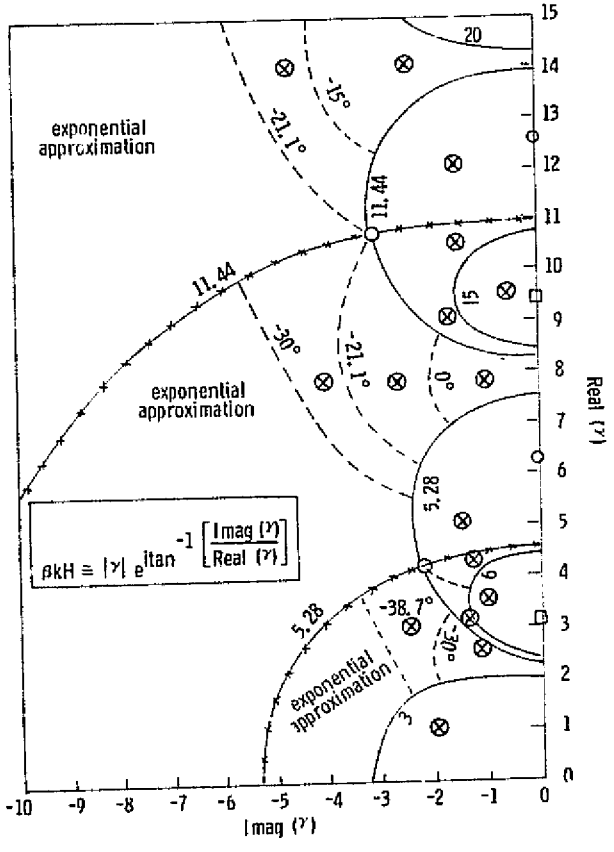

Figure 5. Initial Eigenvalues for Symmetric Modes.

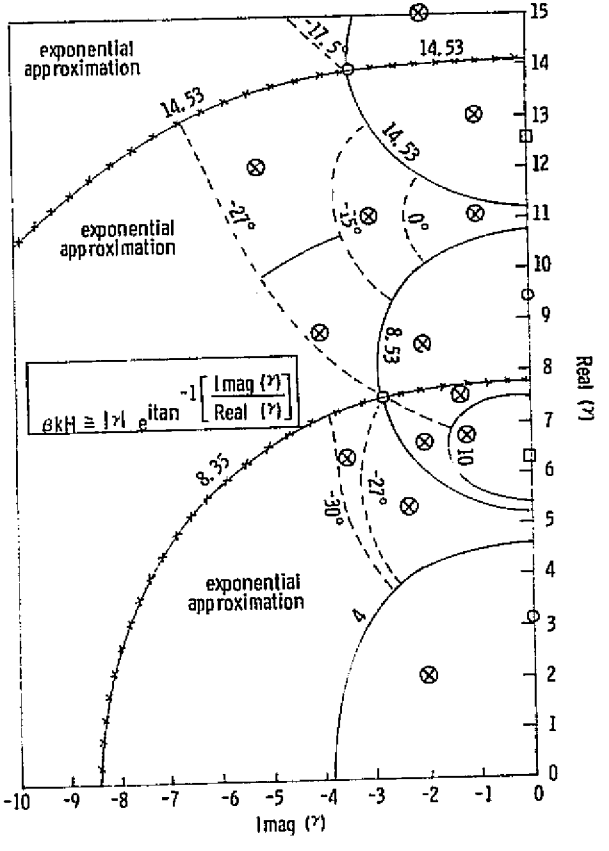

Figure 6. Initial Eigenvalues for Antisymmetric Modes.

$$S(\omega,x) = \sum_{j=1}^{NM} (A_j^+ + A_j^-)\, \phi_j \left(j\pi \frac{x}{H}\right) \tag{16}$$

Thus, the coefficients which present the sum of forward and backward traveling waves can be determined by standard Fourier methods.

The system matrix can be written to allow this interpretation of the source vector as a superposition of forward and backward traveling waves.

The eigenvalues with flow over a softwall section of duct are different in the forward and backward direction, so that in this case a variation of the procedure is required. We multiply Equation (15) successively by

$$\phi_\ell \left(\gamma_\ell^+ \frac{x}{H}\right) \quad \text{and} \quad \phi_\ell \left(\gamma_\ell^- \frac{x}{H}\right) \tag{17}$$

and integrate from zero to H. This gives two sets of equations,

$$\int_0^H S(\omega,x)\phi_\ell\left(\gamma_\ell^+ \frac{x}{H}\right)dx = \sum_{j=1}^{NM}\left[A_j^+ \int_0^H \phi_j\left(\gamma_j^+ \frac{x}{H}\right)\phi_\ell\left(\gamma_\ell^+ \frac{x}{H}\right)dx + A_j^- \int_0^H \phi_j\left(\gamma_j^- \frac{x}{H}\right)\phi_\ell\left(\gamma_\ell^+ \frac{x}{H}\right)dx\right] \tag{18}$$

and

$$\int_0^H S(\omega,x)\phi_\ell\left(\gamma_\ell^- \frac{x}{H}\right)dx = \sum_{j=1}^{NM}\left[A_j^+ \int_0^H \phi_j\left(\gamma_j^+ \frac{x}{H}\right)\phi_\ell\left(\gamma_\ell^- \frac{x}{H}\right)dx + A_j^- \int_0^H \phi_j\left(\gamma_j^- \frac{x}{H}\right)\phi_\ell\left(\gamma_\ell^- \frac{x}{H}\right)dx\right] \tag{19}$$

which can be solved for the A_j^+ and the A_j^-, since the integrals can be carried out.

The theory behind the modal measurement requires the experimental determination of the complex acoustic pressure profile as a function of x across the duct at given frequencies of interest. At a given frequency, the modal coefficients are determined by a modal decomposition of $S(\omega,x)$ in Equation (15) using standard Fourier analysis-type techniques. The magnitude and phase of $S(\omega,x)$ are determined at a number of immersions by measuring the cross-spectral density between a moveable probe in the duct and a reference microphone fixed in the wall of the duct. The experimental setup for a rectangular duct is shown schematically in Figure 7.

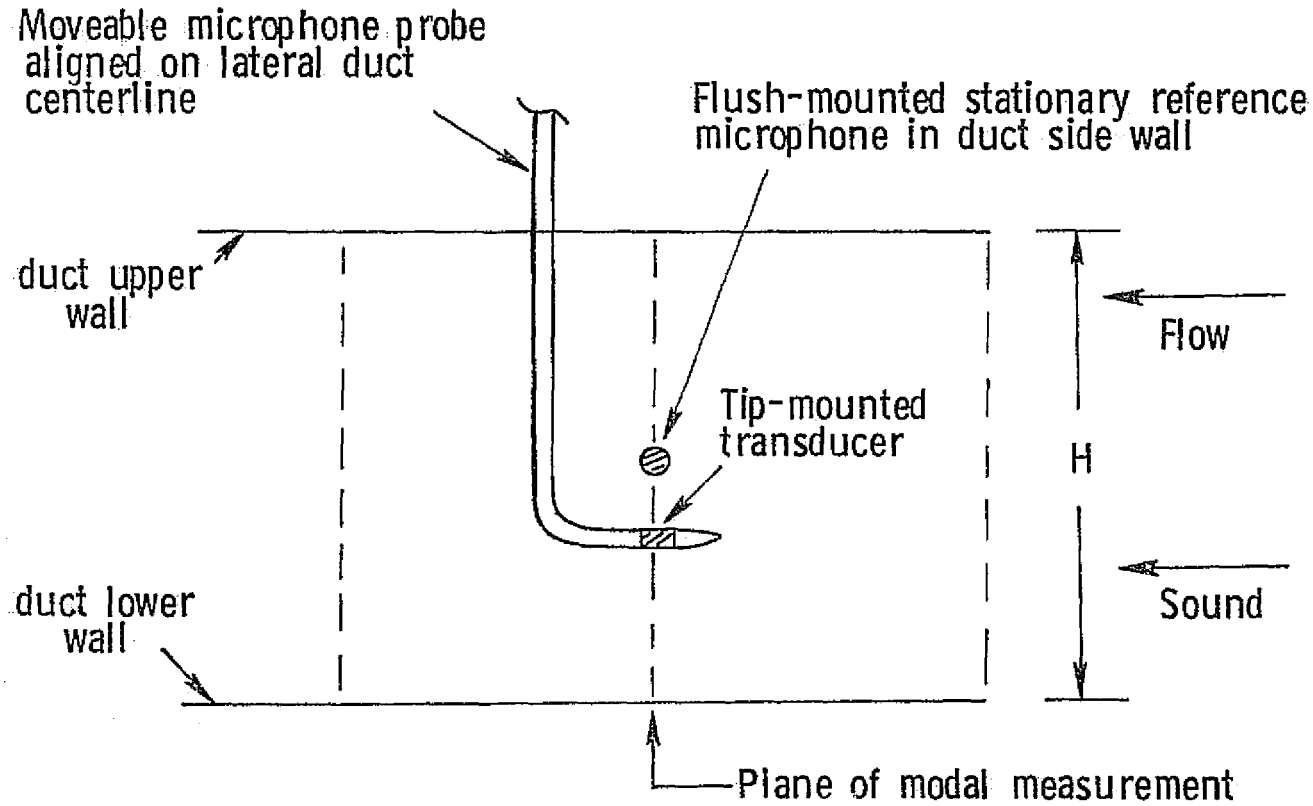

Figure 7. In-Duct Modal Measurement Probe Configuration.

The cross-spectral density of two signals is the product of the Fourier (time) transforms of the two signals in the form

$$S_{rp}(\omega,x_r,x_p) = \overline{p_r(x_r,\omega)}^{*}\,\overline{p_p(x_p,\omega)} \tag{20}$$

where

$p_r(x_r,\omega)$ = reference microphone pressure signal

$p_p(x_p,\omega)$ = probe pressure signal

x_r,x_p = positions of reference microphone and probe

ω = angular frequency, radians/second

The bar denotes Fourier transform with respect to time, and the asterisk denotes complex conjugate. If we make the modal measurement in a hardwall section of duct, the Fourier transform of Equation (16) gives

$$\overline{p(x,\omega)} = \sum_{j=0}^{\infty} C_j(\omega)\ \phi_j\left(\gamma_j \frac{x}{H}\right) \tag{21}$$

where

$$C_j = A_j^{+} + A_j^{-} \tag{22}$$

Combining this with Equation (20), we get

$$S_{rp}(\omega,x) = \left[\sum_{n=0}^{\infty} C_n^{*}(\omega)\right]\left[\sum_{j=0}^{\infty} C_j(\omega)\ \phi_j\left(\gamma_j \frac{x}{H}\right)\right] \tag{23}$$

The first sum on the right hand side is constant with respect to x, so that, if we let

$$B_j(\omega) = C_j(\omega)\left[\sum_{n=0}^{\infty} C_n^{*}(\omega)\right] \tag{24}$$

we can write

$$S_{rp}(\omega, x) = \sum_{j=0}^{\infty} B_j \, \psi_j(\gamma_j \frac{x}{H}) \tag{25}$$

The left side of this expression is obtained from measurement, and the B_j are then obtained from analysis. Since the B_j are proportional to the C_j, the relative magnitude and phase of the modal coefficients can be determined in this manner.

2.4 MATRIX SOLUTION METHOD

The two-dimensional characteristic waves propagating in the duct combine to yield the resultant wave (Equation 4). The amplitude of the resultant wave is the complex sum of the amplitudes of the characteristic waves. It is convenient to represent multimodal acoustic propagation in a multisectioned duct in the form of matrix equations. This is similar to the approach employed by Zorumski[5,6].

In the multielement duct, the finite duct sections are interconnected. Correspondingly, the characteristic duct solution (Equation 4) applied to each finite section must include acoustic coupling effects between the respective duct sections, i.e., the propagating wave must include transmission and reflection effects at the appropriate transverse planes of longitudinal wall impedance discontinuities. Figure 8 shows schematically a two-element duct with the indicated transverse planes.

The condition for acoustic pressure continuity across a plane of axial impedance discontinuity at $z_j = z_{j+1}$ is, in vector form,

$$\{\phi^{-j}\}^T \{A^{-j}\} + \{\phi^{+j}\}^T \{A^{+j}\} = \{\phi^{+(j+1)}\}^T \{A^{+(j+1)}\} + \{\phi^{-(j+1)}\}^T \{A^{-(j+1)}\} \tag{26}$$

For the axial component of acoustic velocity, the continuity condition is

$$\{\phi^{+j}\}^T [\beta_z^{+j}] \{A^{+j}\} + \{\phi^{-j}\}^T [\beta_z^{-j}] \{A^{-j}\} = \{\phi^{+(j+1)}\}^T [\beta_z^{+(j+1)}] \{A^{+(j+1)}\} + \{\phi^{-(j+1)}\}^T [\beta_z^{-(j+1)}] \{A^{-(j+1)}\} \tag{27}$$

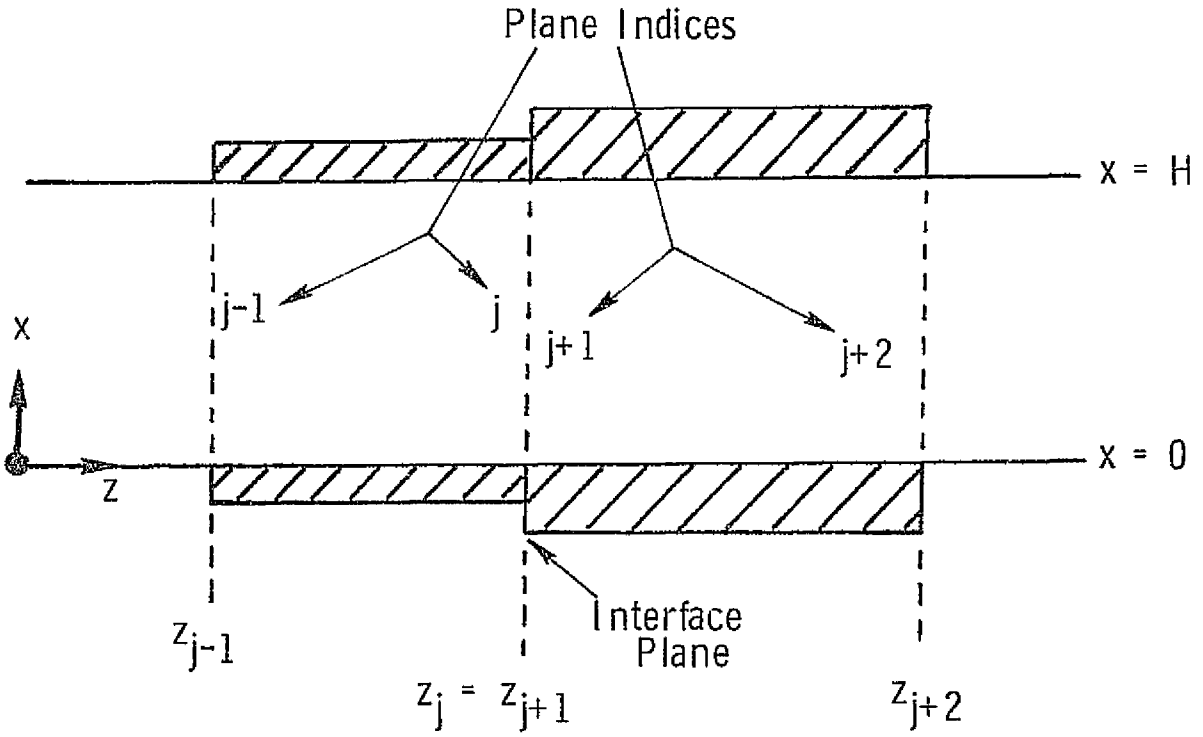

Figure 8. Plane Designation Convention.

where, with the sign of the superscripts indicating direction of wave propagation,

$\{\phi^{\pm j}\}$ = vector of eigenfunctions, plane j

$\{A^{\pm j}\}$ = modal solution vector at plane j

T = superscript designating the transpose of a matrix.

The elements of the axial impedance matrices are given by

$$\beta_z^{\pm j}(I,J) = \frac{\kappa_J^{\pm}}{k - M\kappa_J^{\pm j}} \delta_{IJ} \tag{28}$$

where δ_{IJ} is the Kronecker delta.

$\delta_{IJ} = 1$, for $I = J$

δ_{IJ} 0, for $I \neq J$

By multiplying Equations (26) and (27) by

$$\{\phi^{+(j+1)}\} \tag{29}$$

and integrating across the duct, we obtain

$$\{A^{+(j+1)}\} = [T^{+(j+1),+j}]\ \{A^{+j}\} + [R^{+(j+1),-(j+1)}]\ \{A^{-(j+1)}\} \tag{30}$$

where [T] is a transmission matrix from planes j to j+1 and [R] is a reflection matrix at plane j+1. Thus, this equation relates the forward traveling wave at plane j+1 to the combination of the forward traveling wave transmitted through the discontinuity from plane j and the reflection of the discontinuity from the backward traveling wave at plane j+1.

Similarly, by multiplying Equations (26) and (27) by

$$\{\phi^{-j}\} \tag{31}$$

and integrating across the duct, we obtain

$$\{A^{-j}\} = [T^{-j,-(j+1)}]\ \{A^{-(j+1)}\} + [R^{-j,+j}]\ \{A^{+j}\} \tag{32}$$

Equation (32) relates the backward traveling wave at plane j to the backward traveling wave at plane j+1 transmitted through the discontinuity and the forward traveling wave at plane j reflected from the discontinuity.

The forward traveling mode at plane j and the backward traveling wave at plane j+1,

$$\{A^{+j}\},\ \{A^{-(j+1)}\} \tag{33}$$

are determined by considering the propagation through uniform sections to the left and to the right of the plane of discontinuity.

The matrix equation relating the solution at plane j-1 to the solution at plane j, in the forward direction, is (referring to Figure 8).

$$\{A^{+j}\} = [\ U^{+j,+(j-1)}]\ \{A^{+(j-1)}\} \tag{34}$$

where the elements of the uniform section transmission matrix [U] are given by

$$U^{+j,+(j-1)}(I,J) = \delta_{IJ}\ e^{i\kappa_J^{+}(z_j - z_{j-1})} \tag{35}$$

The matrix equation relating the solution at plane j+2 to the solution at plane j+1, in the backward direction, is

$$\{A^{-(j+1)}\} = [\ U^{-(j+1),-(j+2)}]\ \{A^{-(j+2)}\} \tag{36}$$

where,

$$U^{-(j+1),-(j+2)}(I,J) = \delta_{IJ}\ e^{i\kappa_J^{-}(z_{j+1} - z_{j+2})} \tag{37}$$

Similar equations apply to the backward-traveling wave in the left section and the forward-traveling wave in the right section.

By combining Equations such as (30), (32), (34), and (35), one obtains a set of matrix equations which interrelate the solutions at all planes (note that each uniform section has two planes, one at each end) between the source and duct termination. If, in addition, two equations are written establishing the modal source input and reflection matrix at the source plane, and the reflection matrix at the termination plane, one obtains a complete set of equations for the solution vectors at each plane. By stacking the solution vectors at each plane into one large overall solution vector, a matrix equation is obtained relating the solution vector to the source vector in the form

$$[S]\ \{A\} = \{Q\} \tag{38}$$

where [S] is the system matrix comprised of transmission, reflection, and uniform section matrices stacked into the appropriate blocks, {A} is the stacked modal solution vector, and {Q} is the stacked modal source vector. It is not necessary to locate the source plane at the end of the duct; it can be arbitrarily located by stacking the source modal participation into the appropriate partition of the source vector.

The solution of Equation (38), indicated symbolically by

$$\{A\} = [S]^{-1}\ \{Q\} \tag{39}$$

provides the modal participation at each plane, for both forward and backward traveling waves. The order of the system of equations to be solved is the number of planes multiplied by the number of modes used in the expansion (held constant at each plane) times two (for forward and backward traveling waves). Complex arithmetic is used throughout.

Two indicators can be used to gauge the accuracy of the solution. First, the acoustic pressure or velocity profiles can be reexpanded at planes adjacent to an axial discontinuity to check for continuity. Second, the energy flux at adjacent planes can be calculated to check for energy balance.

2.5 ENERGY FLUX

The expression for the acoustic energy flux in a duct with uniform subsonic mean flow ($|M|<1$) contains terms representing the no-flow acoustic energy flux and convected kinetic and potential acoustic energies. The axial component of the acoustic intensity, i.e., the acoustic power flux per unit area, is given by[7]

$$I_z = \langle pv_z \rangle + \frac{U}{\rho_o c^2} \langle p^2 \rangle + \frac{U^2}{c^2} \langle pv_z \rangle + \rho_o U \langle v_z^2 \rangle \tag{40}$$

where

v_z = axial component of acoustic velocity

U = mean flow velocity in the axial direction

ρ_o = density of air

The brackets <> designate time averages.

Making use of the momentum equation relating acoustic pressure and velocity and considering modal acoustic intensity, one gets expressions for the intensity for the cases of

a. the forward traveling wave modes

$$I_z^+(m,n) = \mathrm{Re}\left\{ \frac{p_m^+(p_n^+)^*}{2\rho_o c} \left[\frac{(\kappa_n^+)^*}{k} (1+M^2+M \frac{\kappa_m^+}{k}) + M \right] \right\} \tag{41}$$

b. the backward traveling wave modes

$$I_z^-(m,n) = \mathrm{Re}\left\{ \frac{p_m^-(p_n^-)^*}{2\rho_o c} \left[\frac{(\kappa_n^-)^*}{k} (1+M^2+M \frac{\kappa_m^-}{k}) + M \right] \right\} \tag{41}$$

where m and n are modal indices and the asterisk denotes the complex conjugates.

The corresponding modal energy fluxes, $E_z^+(m,n)$ and $E_z^-(m,n)$ are obtained by integrating the respective modal intensities (41) and (42) over the duct cross-sectional area, i.e.,

$$E_z^+(m,n) = \int_o^h I_z^+(m,n)\,dx \tag{43}$$

and

$$E_z^-(m,n) = \int_o^h I_z^-(m,n)\,dx \tag{44}$$

The total energy flux in the forward and backward direction is calculated from Equation (43) and (44) by performing double summations over all modes. The net energy flux at any cross-sectional duct plane is the algebraic sum of the total forward and backward energy flux.

The analysis determines the modal energies for forward- and backward-traveling waves at the planes of discontinuity, as well as the modal energy sums and the net energy flux. This allows investigation of energy transmission and reflection effects at duct section interfaces.

The overall suppression is composed of the combined attenuation of individual modes, each at a particular level of participation. The individual mode attenuation rates are given by the imaginary part of the propagation constant, Equation (5), which can be written as

$$\kappa_m = \sigma_m + i\,\tau_m \tag{45}$$

The attenuation rate for each mode is, then,

$$\text{Att} = -8.686\,\tau_m H \tag{46}$$

where the units are dB per unit duct height.

SECTION 3.0

PRELIMINARY OPTIMIZATION STUDIES

The analysis was applied to optimize the design of a two-element suppressor for test in a laboratory duct test facility. The method used was to determine the impedance components of each element, both resistance and reactance, which would yield the maximum suppression for the test conditions to be imposed in the experiment.

3.1 SPECIFIED CONDITIONS

The conditions used for the optimization study were as follows:

- Rectangular duct geometry as shown schematically in Figure 9 The height between treated sections was 26.7 cm (10.5 in.); the duct width was 10.2 cm (4 in.); the total treated length was 91.4 cm (36 in.), equally divided for each of the two treatment panels. This resulted in a total treatment length/duct height ratio of 3.43.

- Design frequency of 2000 Hz with input modal energy distribution as determined by measurement in the test facility. This included both no-flow and flow at 0.3 Mach number.

  This choice of design frequency resulted in a duct height/wavelength ratio of 1.535 so that at least two higher-order modes were cut-on for the no-flow condition; at least one more was cut-on with flow. Thus, counting the lowest order mode, four modes could propagate with flow in the hardwall duct. More could propagate depending upon the treatment impedance components (to be determined by the analysis). As noted in Section 4.1, the sound source was deliberately set off-axis to excite higher order modes.

- Input modal energy distributions (modal expansion coefficients) shown in Figure 10 for no-flow and in Figure 11 for flow at 0.3 Mach number. These distributions were determined experimentally for the untreated, hardwall duct. Note that the distributions are substantially different with and without flow. Thus, the optimized impedance components derived from the analysis include more than simple flow convection of the acoustic wave. Also note that some energy in cut-off modes is present at the source, but the cut-on modes dominate in both cases.

In the analysis, seven modes were included in the energy balance. Continuity of particle displacement was used for the wall boundary. Since the tests were conducted with an air supply at room temperature, standard atmospheric conditions were assumed.

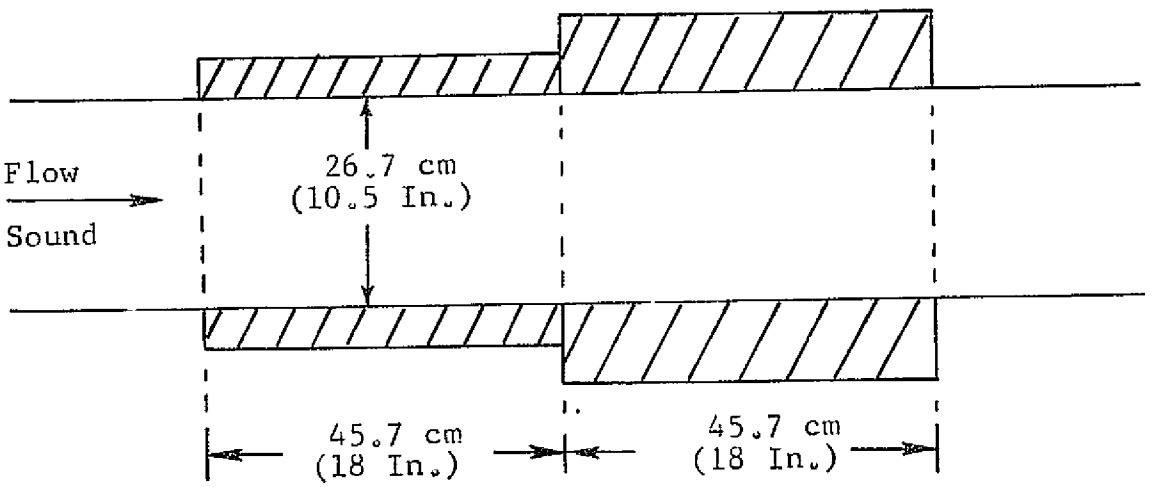

Figure 9. Schematic View of the Rectangular Duct.

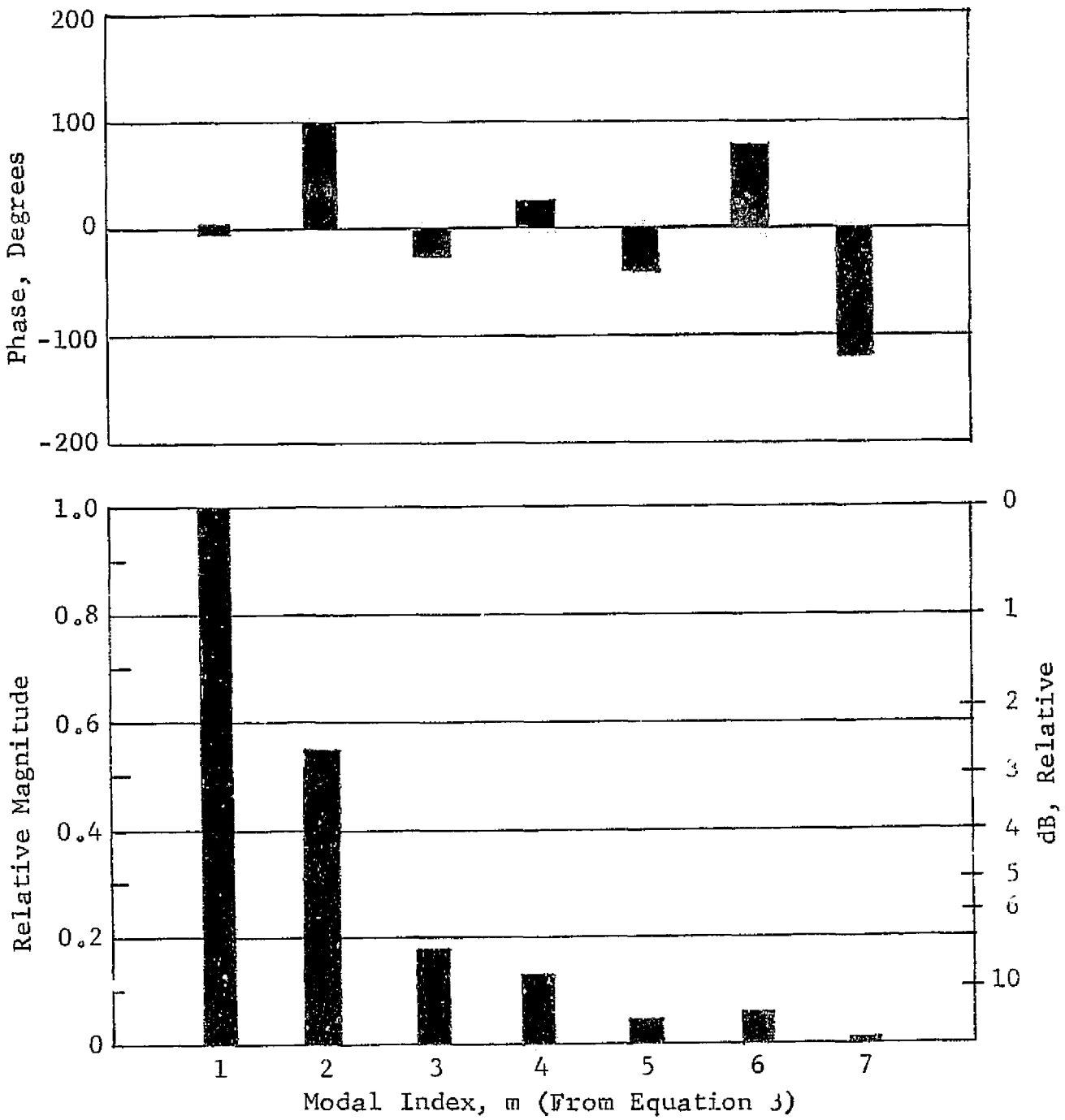

Figure 10. Source Modal Coefficients for 2000 Hz Signal, Mach 0.0.

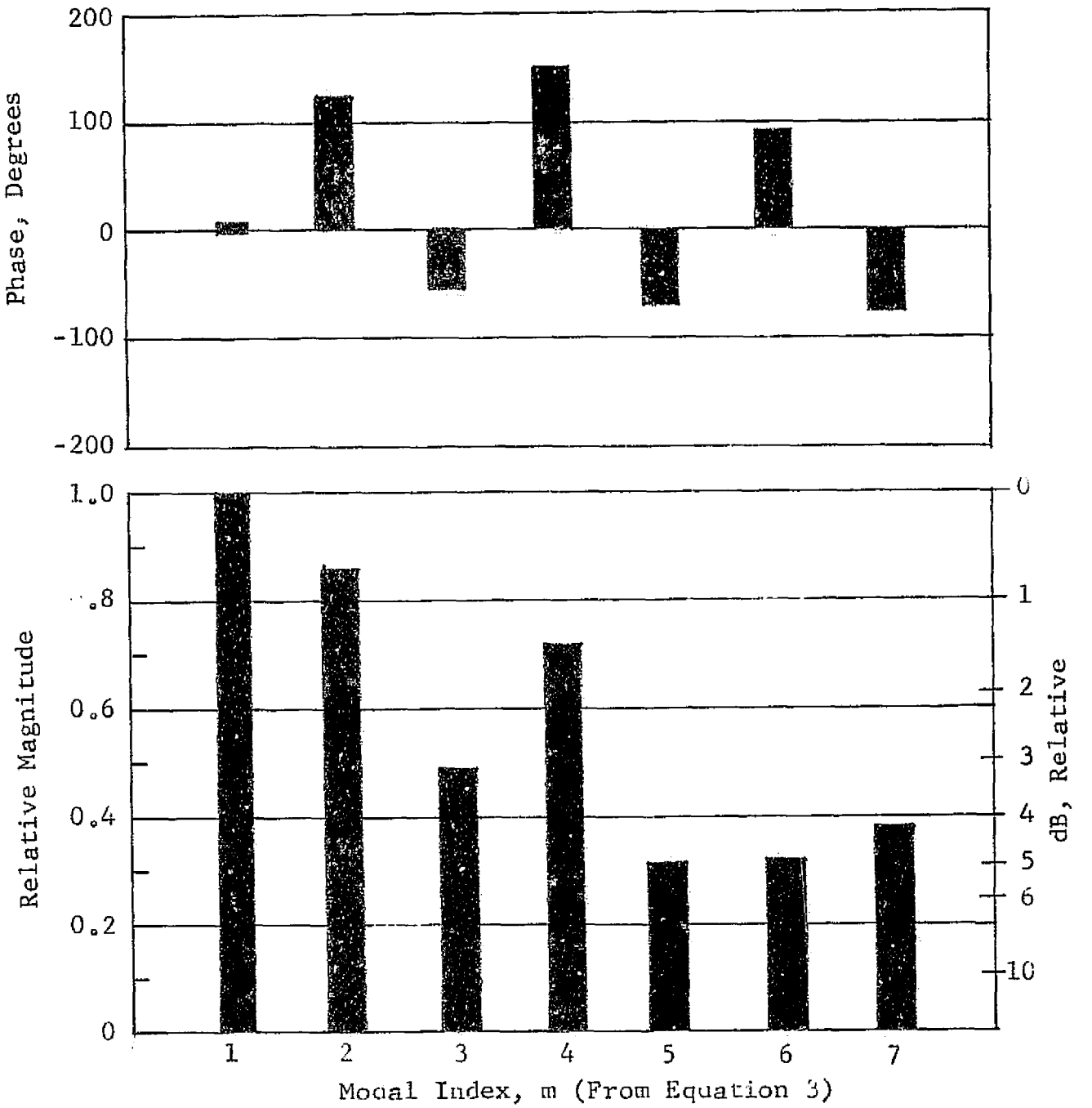

Figure 11. Source Modal Coefficients for 2000 Hz Signal, Mach 0.3.

3.2 ITERATIVE OPTIMIZATION PROCEDURE

The analysis was used to estimate the optimum effectiveness first, of a uniform liner, and then, of a two-segment liner for the specified geometry, frequency, and source conditions. The uniform treatment involves only two parameters (the two impedance components), but the two-sectional liner requires that four parameters (two impedance components for each liner segment) be varied.

An iterative optimization procedure was used, as outlined below:

- The best uniform liner was found by parametrically varying its impedance components.

  Figures 12 and 13 show the calculated suppression as a function of normalized reactance and resistance respectively, for the no-flow case; maximum attenuation of about 28.2 dB occurs for $Z/\rho c = 1.25 - 1.65i$.*

  Figure 14 shows contour plots of constant attenuation in the uniform liner impedance plane at Mach 0.3 flow; maximum attenuation of about 21.6 dB occurs for $Z/\rho c = 0.9 - 1.0i$. This is markedly less than that predicted for no-flow conditions.

- Using the impedance of the optimized single-element liner for the downstream segment, the impedance components (resistance and reactance) of the upstream liner segment were varied until peak suppression was attained.

  At M = 0, a maximum attenuation of 29.2 dB is predicted (first segment impedance ratio $Z_1/\rho c = 1.15 - 1.8i$, followed by $Z_2 = 1.25 - 1.65i$). At flow of Mach 0.3, the maximum attenuation is predicted to be 22.4 dB ($Z_1/\rho c = 0.9 - 1.2i$ and $Z_2/\rho c = 0.9 - 1.0i$). The associated contour plots of constant attenuation of the two-segment liner in the impedance plane of the first segment are shown in Figure 15.

- The impedance of the upstream liner segment was unchanged while the impedance components of the downstream segment were varied.

  In this step for the no-flow case, a peak suppression of 32.2 dB was calculated ($Z_1/\rho c = 1.15 - 1.8i$ and $Z_2/\rho c = 1.33 - 1.35i$). Correspondingly, a peak suppression of 25.2 dB was predicted for the case with Mach 0.3 flow. ($Z_1/\rho c = 0.9 - 1.2i$ and $Z_2/\rho c = 0.9 - 0.8i$) as shown in Figure 16.

---

*Note: The normalized impedances given in this report are all referred to the more conventional $e^{+i\omega t}$ form. This is the complex conjugate of the value which is used in the theoretical analysis.

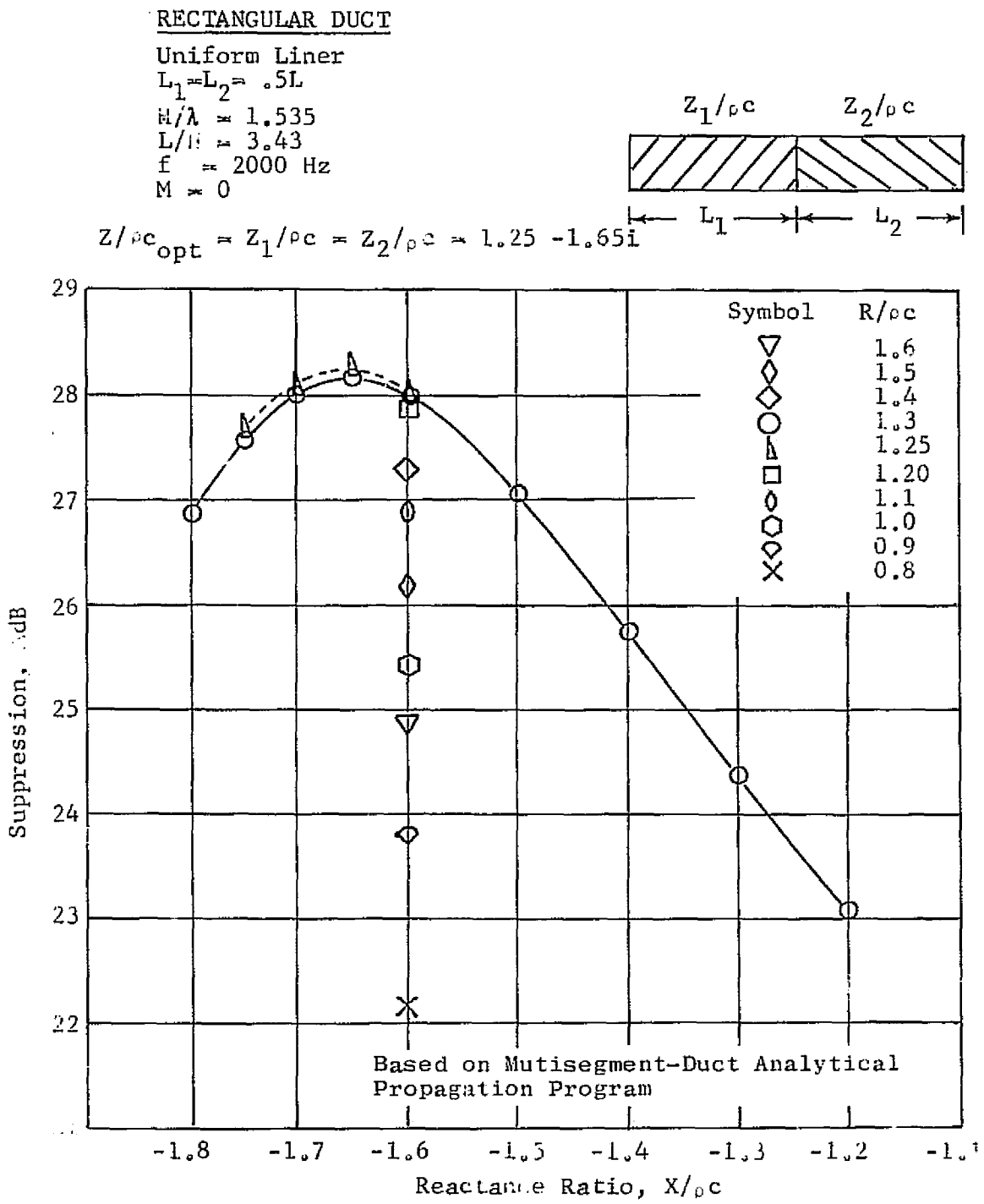

Figure 12. Calculated Suppression for a Uniform Liner as a Function of Liner Reactance Ratio.

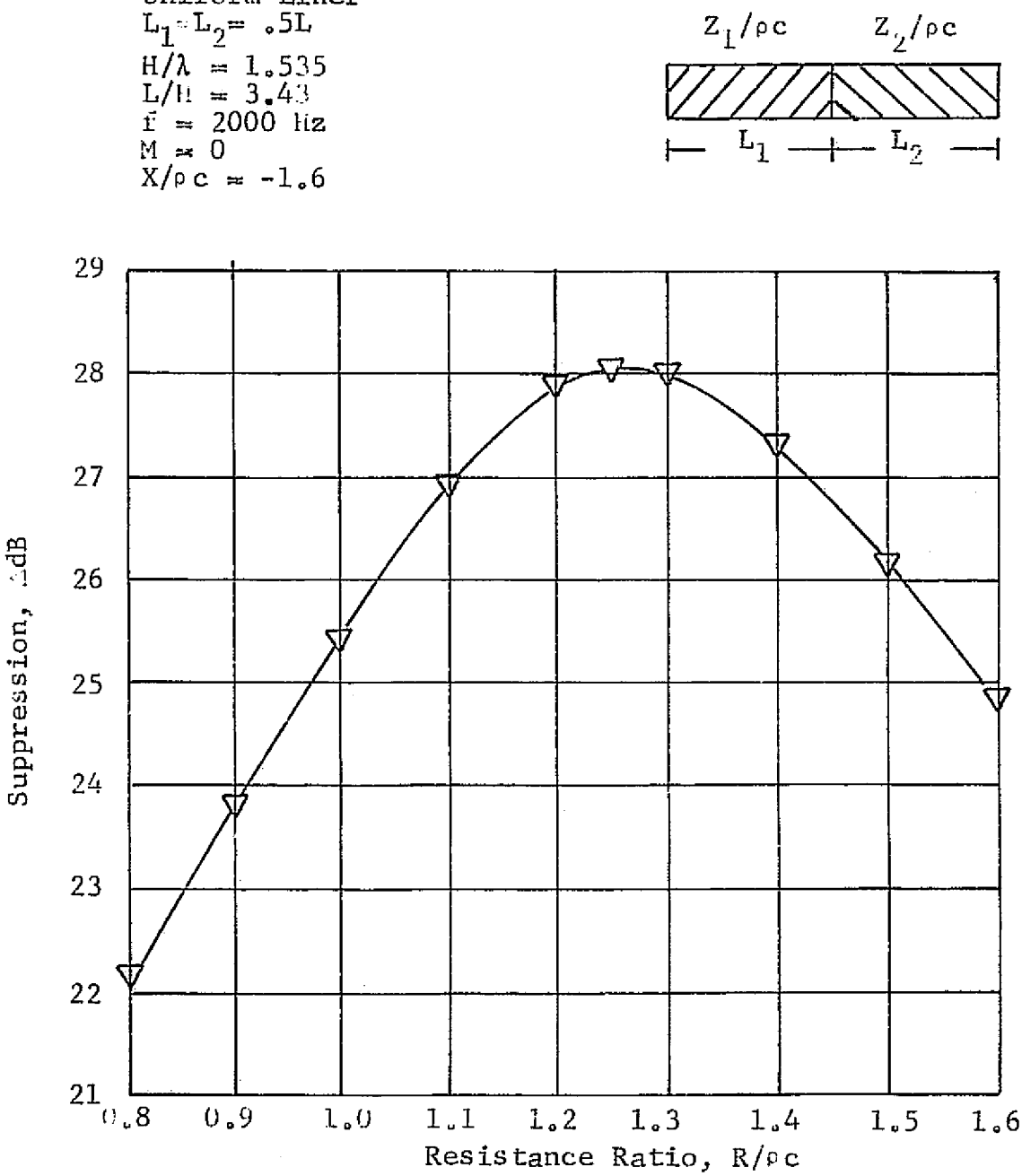

Figure 13. Calculated Suppression for a Uniform Liner as a Function of Liner Resistance Ratio.

RECTANGULAR DUCT

Uniform Liner
$L_1=L_2=.5L$
$H/\lambda = 1.535$
$L/H = 3.43$
$f = 2000$ Hz
$M = 0.3$
Cont. Part. Displ.

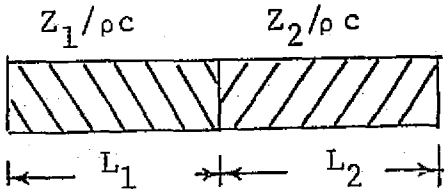

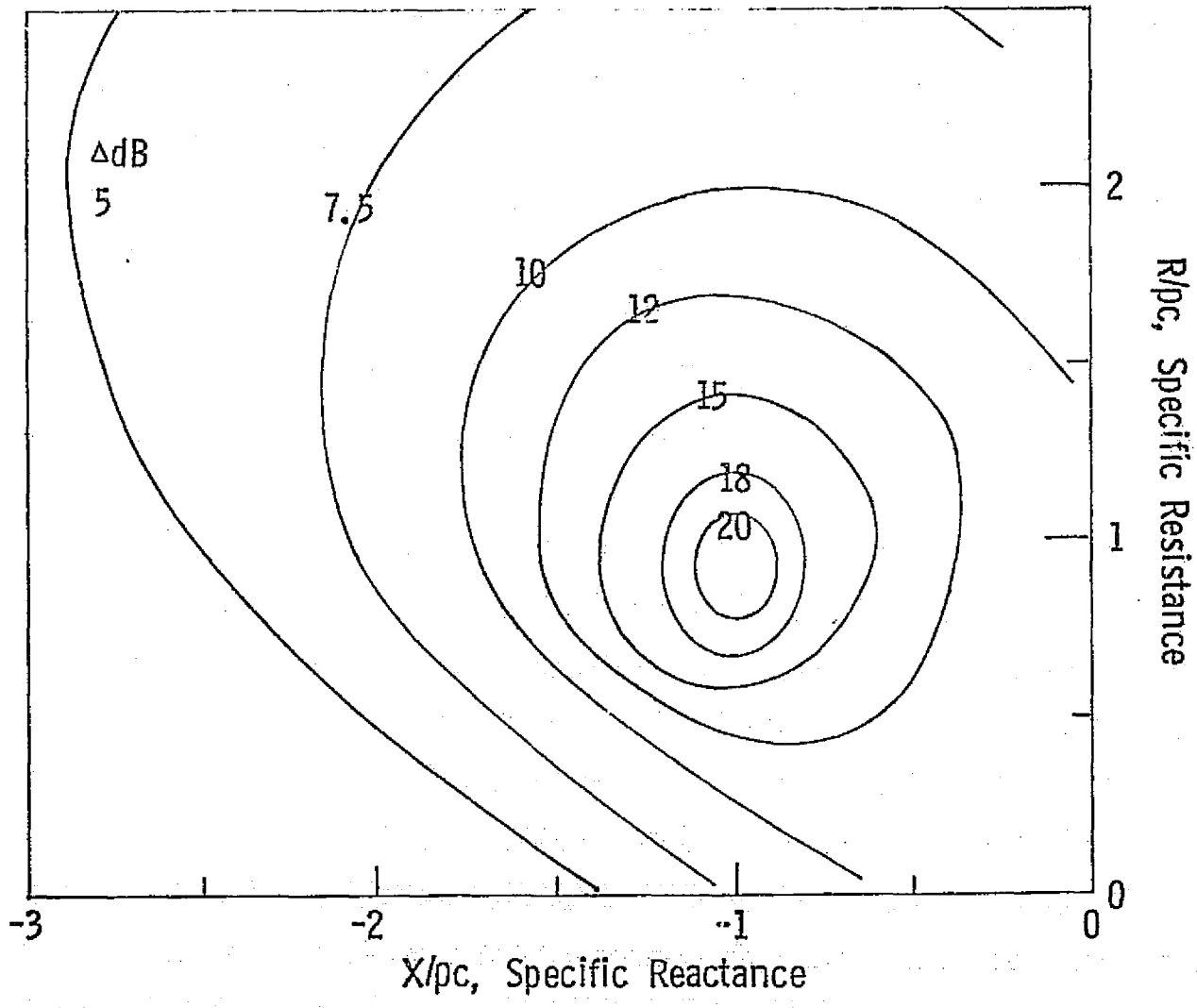

Figure 14. Contours of Constant Attenuation in Impedance Plane Single-Element Liner, Rectangular Duct.

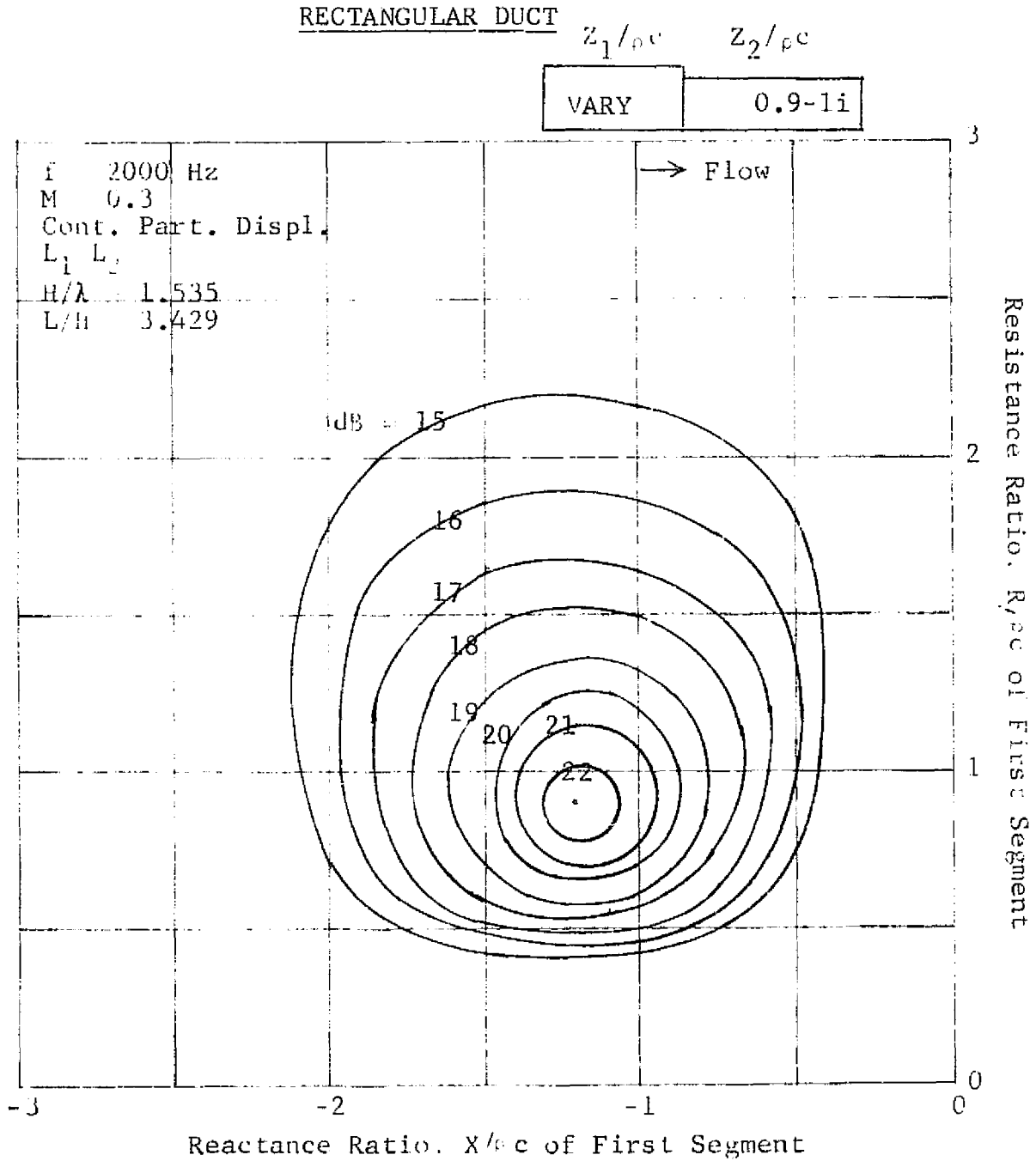

Figure 15. Contour Plot of Two-Segment Liner Attenuation for Various Values of the Acoustic Impedance Ratio of the First Liner Segment.

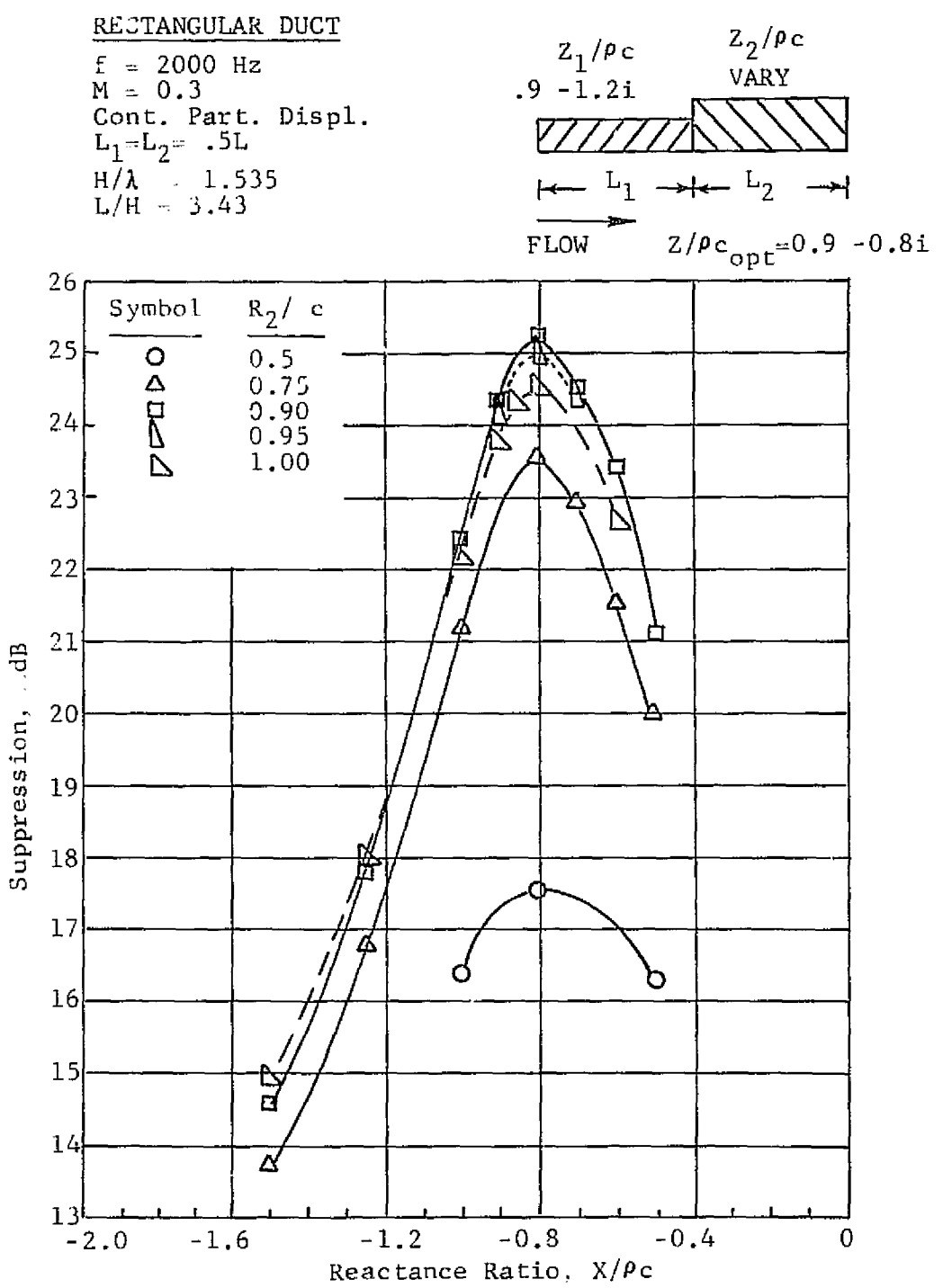

Figure 16. Calculated Suppression for a Two-Segment Liner as a Function of the Impedance Ratio of the Second Liner Segment.

- The alternating iterative procedure of the preceding two steps was repeated until the impedance changes yielded less than one dB increase in suppression.

- Having achieved the latter, the corresponding values of the resistance and reactance ratios were varied by ± 0.1 each to ascertain that the predicted suppression was indeed near or at a maximum.

3.3 RESULTS OF OPTIMIZATION

The predicted peak suppressions, and the associated impedance components, at the conclusion of each iteration without and with flow are listed in Tables I and II, and shown graphically in Figures 17 and 18, respectively. Bar graphs of the predicted peak suppressions from each iterative step are shown in Figures 19 and 20.

The final result for the optimized two-segment liner without flow is about 39.0 dB, an increase of 10.8 dB over the optimized uniform liner suppression of 28.2 dB. With flow the result is 29.3 dB versus 21.6 dB for the uniform liner.

In all cases considered, maximum suppression occurred at negative reactances of both liner segments. In the course of the iteration for the case without flow, the resistance ratio of the first liner segment decreased from the single-element optimum value of 1.25 to 0.85. Its reactance also decreased from -1.65 to -1.85 (an increase in absolute value). The resistance and reactance of the second liner segment increased. The former underwent a moderate increase from 1.25 to 1.35, while the latter changed more rapidly from -1.65 to -1.04 (a decrease in absolute value from 1.65 to 1.04).

For the case with flow of Mach 0.3, the changes in the liner segment impedance ratio components followed similar trends as in the case of M = 0. This is shown in Figure 21.

While the resistance of the first liner segment decreased somewhat (from 0.9 to 0.7) in the course of the iterations, the absolute value of its reactance increased (from 1 to 1.37). The resistance of the second segment remained unchanged (0.9), the absolute value of its reactance decreased from 1.0 to 0.7.

Although the approximate design procedure of dividing the respective resistance and reactance values at M = 0 by the factor (1+M), with M = 0.3, does not yield the corresponding exact values of the liner segment resistances and reactances at M = 0.3, it produces the expected trends. The $1/(1+M)$ factor would be obtained from the continuity of particle velocity assumption, and is also the value obtained from empirical results. Based on continuity of particle displacement, a factor of $1/(1+M)^2$ would be chosen.

For an optimized two-element treatment arrangement, the final value of impedance requires a thinner liner element with a higher faceplate porosity for the first liner segment than for the second one.

Table I. Summary of Rectangular Duct Propagation Program Liner Optimization, Mach 0.0.

f = 2000 Hz M = 0.0 $L_1 = L_2 = 45.72$cm (18") $L = L_1 + L_2$ $H/\lambda = 1.535$ $L/H = 3.43$

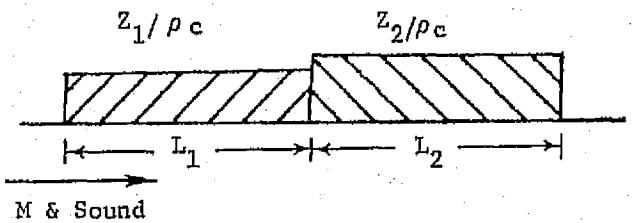

Iteration Number	Upstream Section Impedance Ratio $Z_1/\rho c$	Downstream Section Impedance Ratio $Z_2/\rho c$	Total ΔdB	
1	1.25 - 1.65i	1.25 - 1.65i	-28.2	(Single Element Optimum)
2	1.15 - 1.80i	1.25 - 1.65i	-29.2	(Iterate on $Z_1/\rho c$)
3	1.15 - 1.80i	1.33 - 1.35i	-32.2	(Iterate on $Z_2/\rho c$)
4	1.0 - 1.83i	1.33 - 1.35i	-34.2	(Iterate on $Z_1/\rho c$)
5	1.0 - 1.83i	1.35 - 1.15i	-36.2	(Iterate on $Z_2/\rho c$)
6	0.93 - 1.85i	1.35 - 1.15i	-37.8	(Iterate on $Z_1/\rho c$)
6A	0.93 - 1.85i	1.35 - 1.04i	-38.55	(Iterate both $Z_1/\rho c$ and $Z_2/\rho c$)
6B	0.85 - 1.85i	1.35 - 1.04i	-38.95	(Iterate on $Z_1/\rho c$)

Table II. Summary of Rectangular Duct Propagation Program Liner Optimization, Mach 0.3.

f = 2000 Hz M = 0.3 n = 2 $L_1=L_2=$ 45.72cm (18") $L = L_1+L_2$ H/λ = 1.535 L/H = 3.43

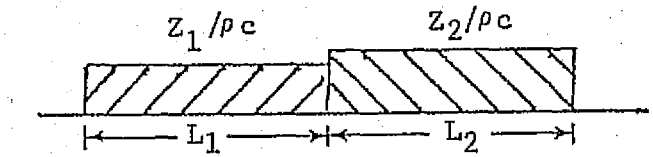

Iteration Number	Upstream Section Impedance Ratio $Z_1/\rho c$	Downstream Section Impedance Ratio $Z_2/\rho c$	Total ΔdB	
1	0.9-1i	0.9-1i	-21.6	(Single Element Optimum)
2	0.9-1.2i	0.9-1i	-22.4	(Iterate on $Z_1/\rho c$)
3	0.9-1.2i	0.9-0.8i	-25.2	(Iterate on $Z_2/\rho c$)
4A	0.8-1.3i	0.9-0.8i	-26.9	(Iterate on $Z_1/\rho c$)
4B	0.8-1.3i	0.9-0.7i	-28.1	(Iterate on $Z_2/\rho c$)
5A	0.7-1.3i	0.9-0.7i	-28.46	(Iterate both $Z_1/\rho c$ and $Z_2/\rho c$)
	0.8-1.4i	0.9-0.7i	-28.66	
5B	0.7-1.37i	0.9-0.7i	-29.31	

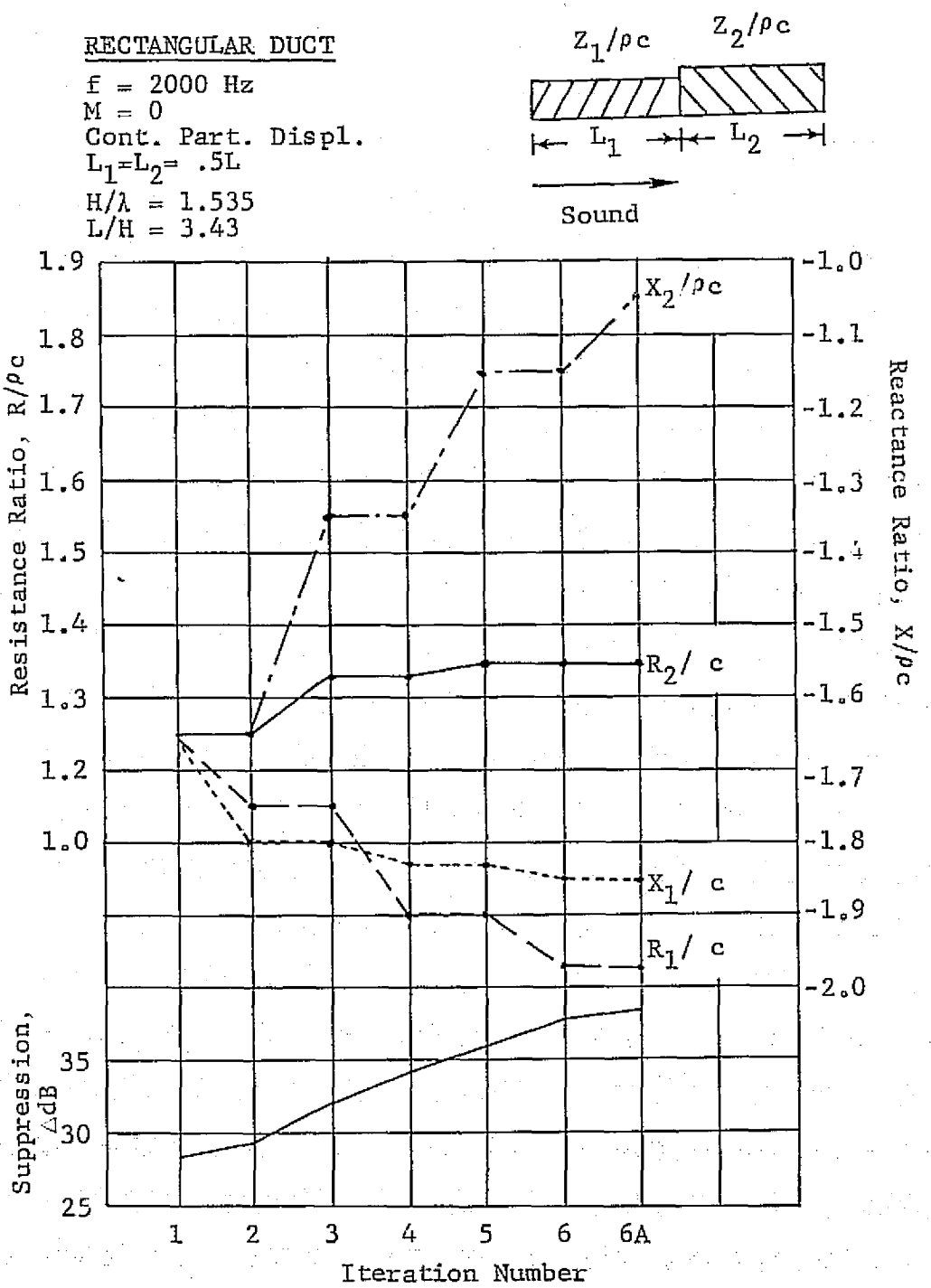

Figure 17. Optimum Impedance Components and Associated Suppression in a Lined Rectangular Duct without Flow.

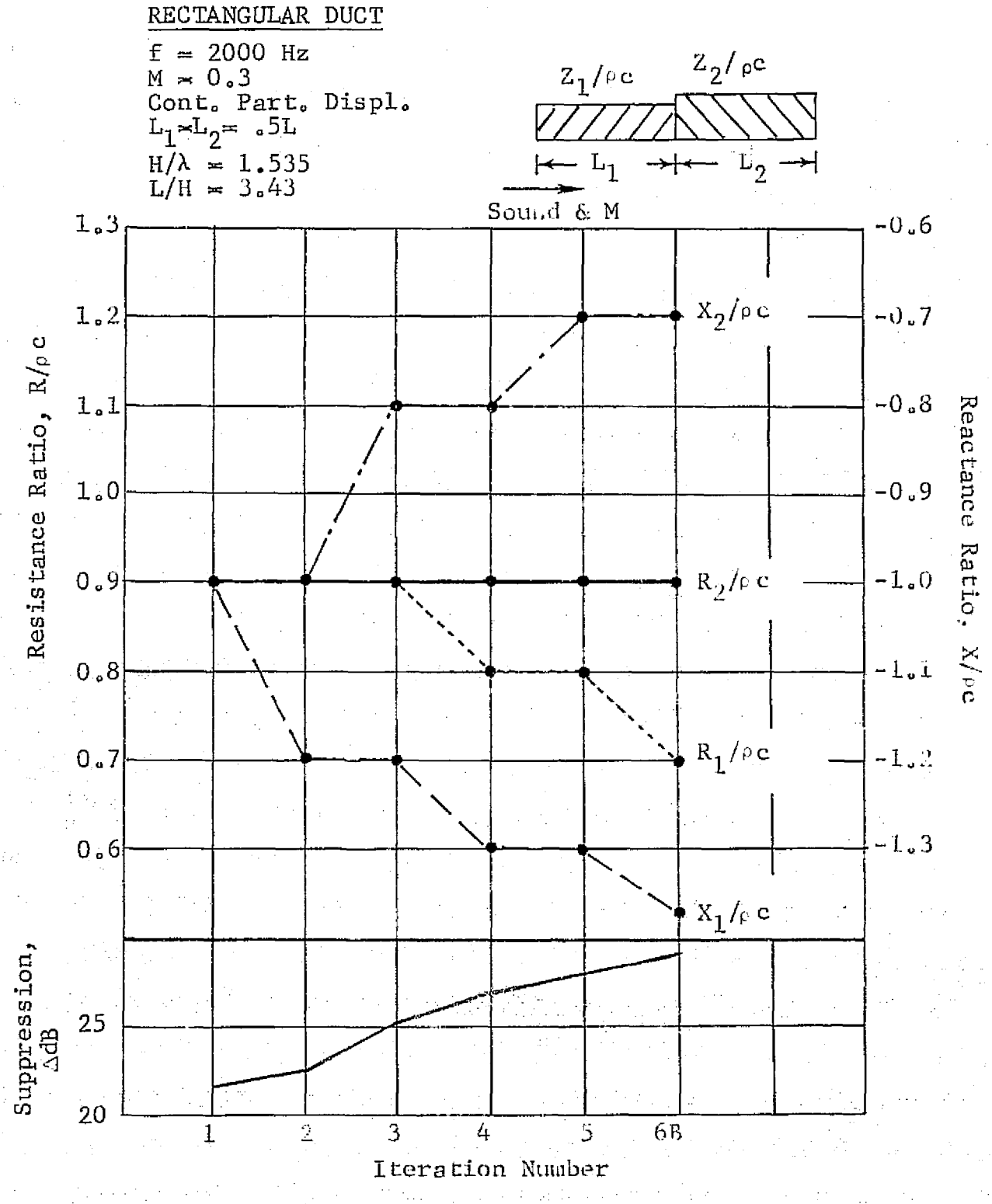

Figure 18. Optimum Impedance Components and Associated Suppression in a Lined Rectangular Duct with Flow.

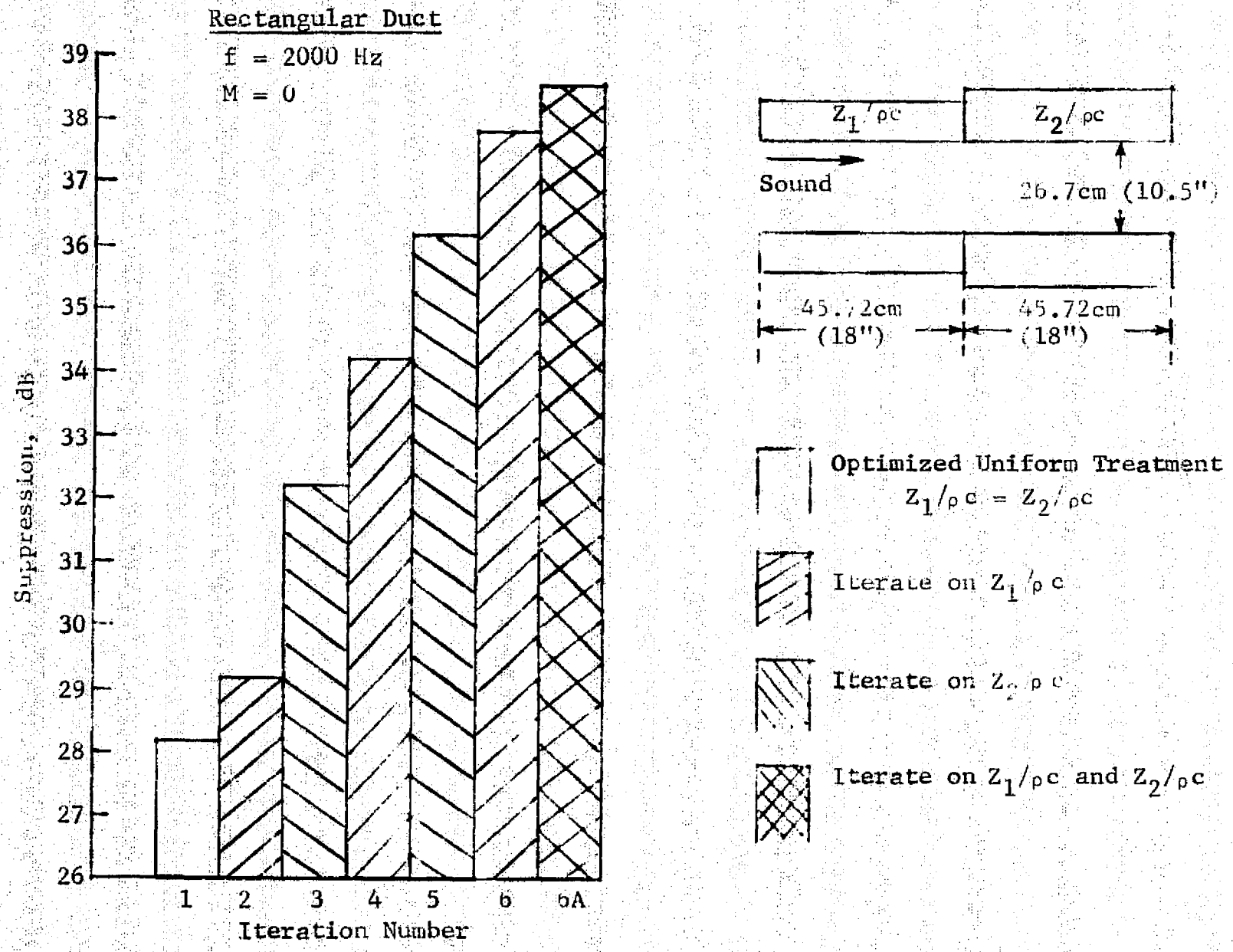

Figure 19. Uniform and Two-Section Treatment Maximum Predicted Sound Power Attenuation Versus Iteration Number, No Flow.

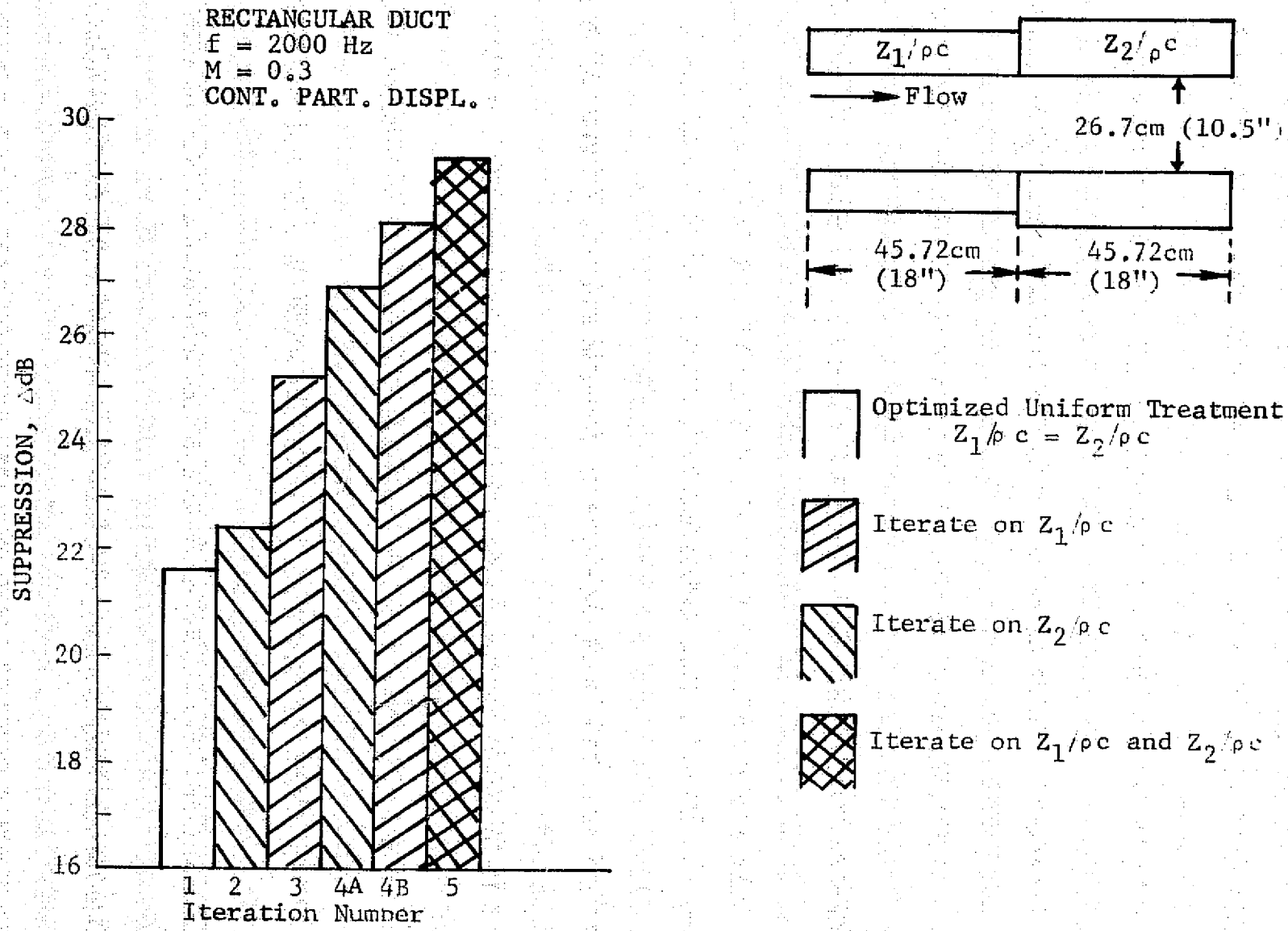

Figure 20. Uniform and Two-Section Treatment Maximum Predicted Sound Power Attenuation Versus Iteration Number, Mach 0.3.

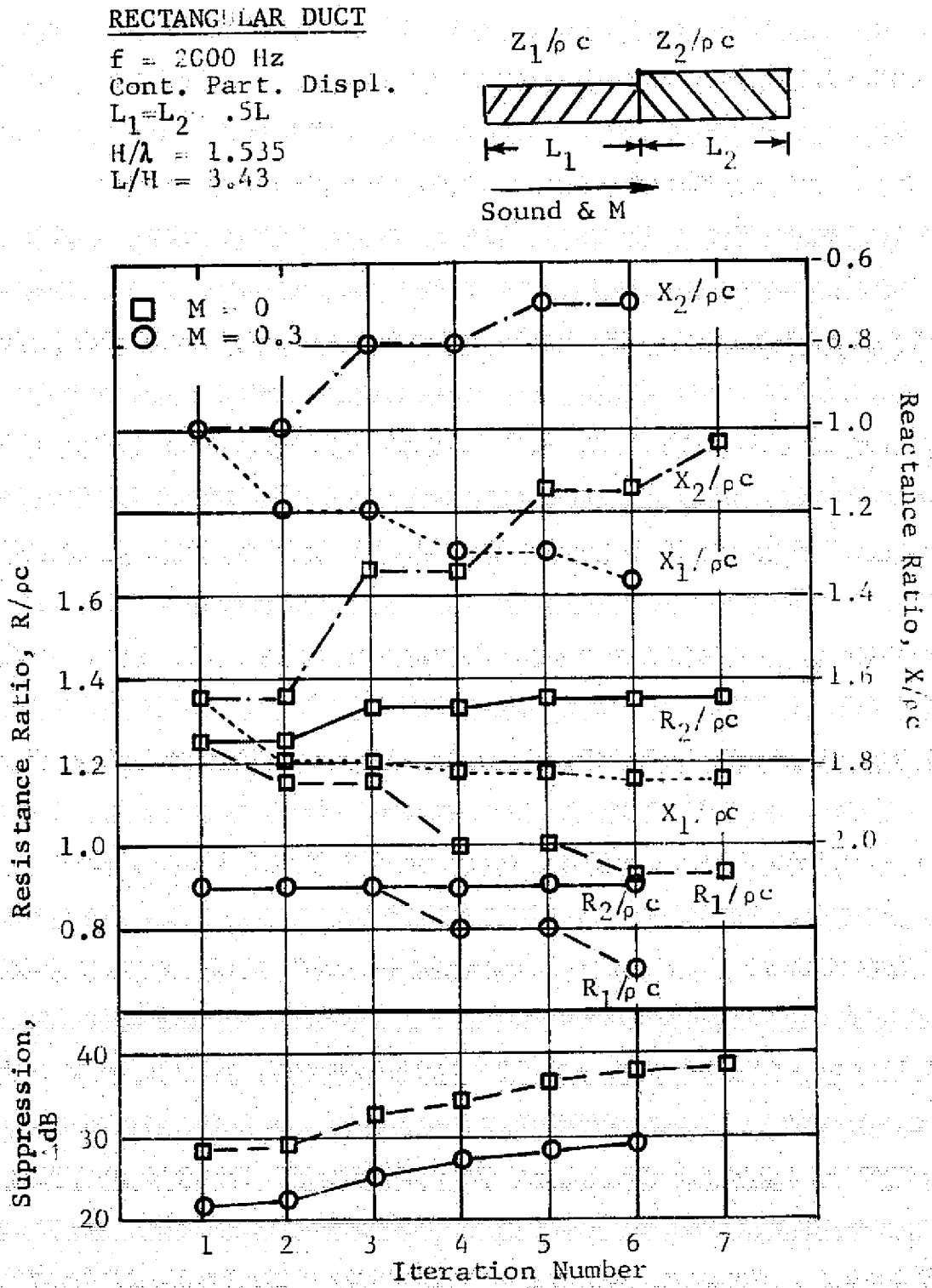

Figure 21. Optimum Impedance Components and Associated Suppressions in a Lined Rectangular Duct without Flow, and with Flow (M = 0.3).

Figure 22 shows the results of iteration 6B (See Table I). The objective of that iteration was to explore the effect of the resistance, particularly very low resistance, of the first liner segment on the suppression. Thus, the resistance of the first (upstream) segment was varied from very low values to high values, while its reactance and the impedance of the second segment obtained in the preceding iteration (6A) were kept constant.

The second liner segment was found, in all optimized cases, to cause more suppression than the first one of equal length. An example at Mach 0.0 is shown in Figure 22. The figure shows, in addition to the total suppression (due to both liner elements), the attenuation due to the first segment only. The latter attenuation is close to zero for near-zero resistances of the first liner segment; it increases with resistance and attains a broad maximum for a resistance ratio of 0.85. Beyond that, it decreases very slowly. The total attenuation of both segments peaks at the same resistance as the first segment. Its increase and decrease, however, are characterized by steeper slopes than the attenuation by the first liner segment.

For very similar conditions, Baumeister[8] has found optimized two-element configurations for very low resistances of the first section. During the convergence process in the search for the optimum, special effort was made to check for maximum suppression conditions which decreased the first liner resistance. There was no indication of any trend toward low first liner resistances in this case. In fact, all indications were that the optimum suppression occurs at a unique value of impedance (holding η, the panel lengths, and the modal content constant). When the particular optimum cases run by Baumeister were attempted by the modal analysis, numerical convergence problems were encountered in most cases, leading to indeterminate results. As will be shown in a later section, there are optimization conditions (in particular, higher η values) which lead to low resistances in the first section.

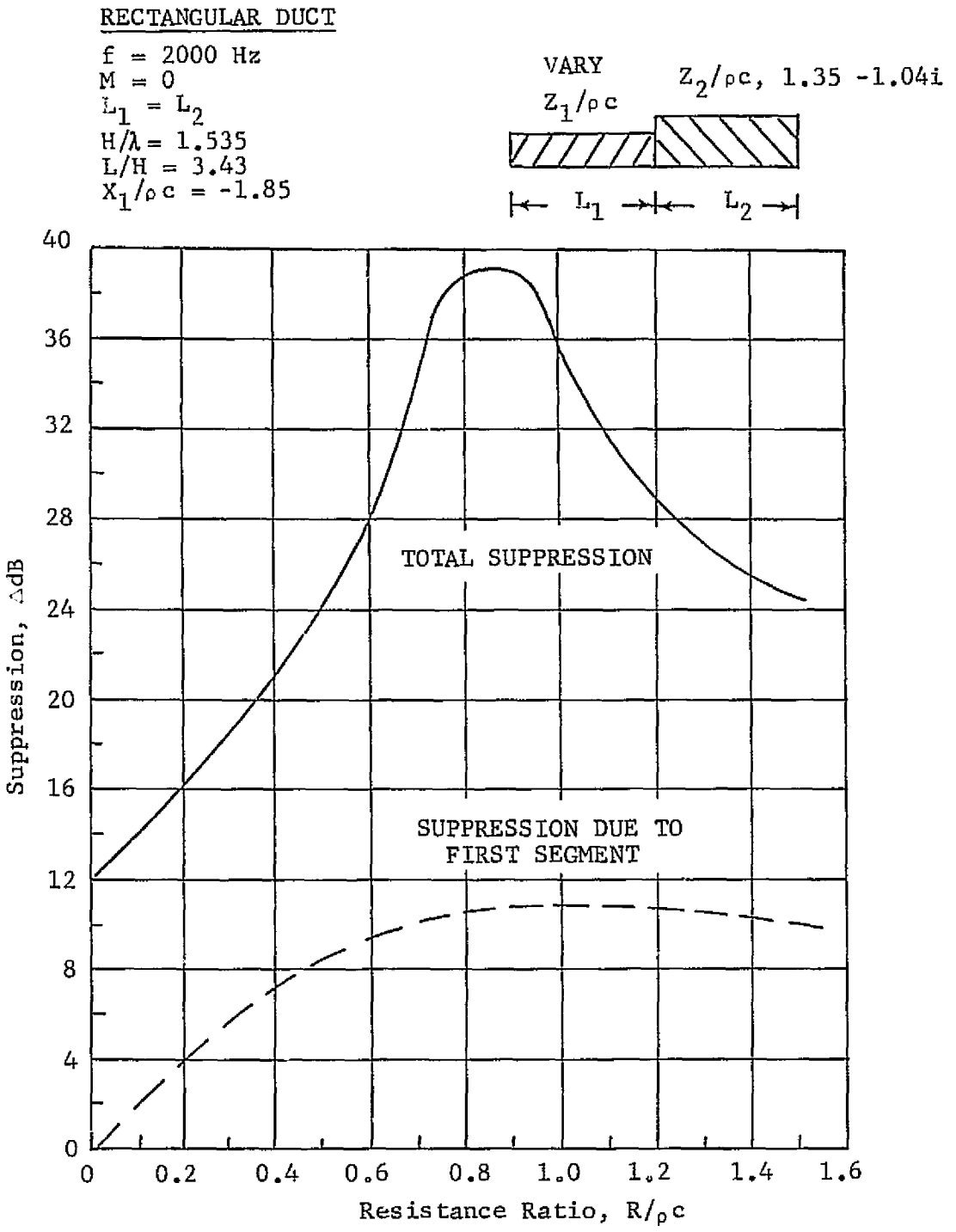

Figure 22. Calculated Suppression for a Two-Segment Liner as a Function of the Resistance Ratio of the First Liner Segment.

SECTION 4.0

DUCT TEST PROGRAM

The test program had as its primary objective the experimental demonstration of the suppression properties of the optimized treatment designs determined analytically in Task I of the program. The test program was accomplished in two phases. Phase I comprised the measurement of suppression for six treatment configurations using liner design parameters which were believed to bracket the desired impedance components. Phase II was a test of several treatment configurations with the objective of improving on the results of Phase I, using knowledge gained from the first series of tests.

4.1 DUCT FACILITY DESCRIPTION

The rectangular cold flow duct facility provides the capability of measuring treatment sample acoustic transmission losses under conditions of continuous flow with Mach numbers up to about 0.5. The duct is 10.2 cm (4 inches) in width with hardwall sides and allows duct heights up to 40.6 cm (16 inches) with treatment panels at the top and bottom. The treatment panels are contained in trays 91.4 cm (36 inches) in length which allows interchangeability of perforated faceplate and honeycomb backing. The treatment panels can be segmented in the trays, allowing axial variation of faceplate porosity and cavity depth in the treatment section.

The noise source for the duct is a Ling Model LPT100 electropneumatic high intensity driver which can be excited by broadband or pure-tone input signals. As shown in Figure 23, the source is mounted upstream of the treatment, providing an exhaust duct mode of operation. Note that the source input port to the duct is mounted asymmetrically with respect to the duct vertical centerline for these tests. This was done specifically to insure the presence of higher order duct modes in the treatment input signal.

The duct terminates downstream of the treatment with an unflanged end, exhausting into a reverberant room. A muffler section is included at the end of the duct to minimize end reflections and waves reentering the end of the duct.

The acoustic measurements are taken with traversing probes installed upstream and downstream of the treated section. The probes traverse vertically across the duct along a line midway between the sidewalls of the duct. The probes are specially constructed using a dynamic pressure transducer that is a 0.23 cm Kulite sensor mounted in the tip of the probe, as shown in Figure 24. The Kulite transducer is a highly linear device based on a strain gauge principle. It has lower sensitivity than the more conventional B&K condensor microphone but is much less sensitive to mechanical vibration. The low level output of the Kulite transducer requires the use of a low-noise, high-gain preamplifier for signal conditioning. Princeton Applies Research Model 113

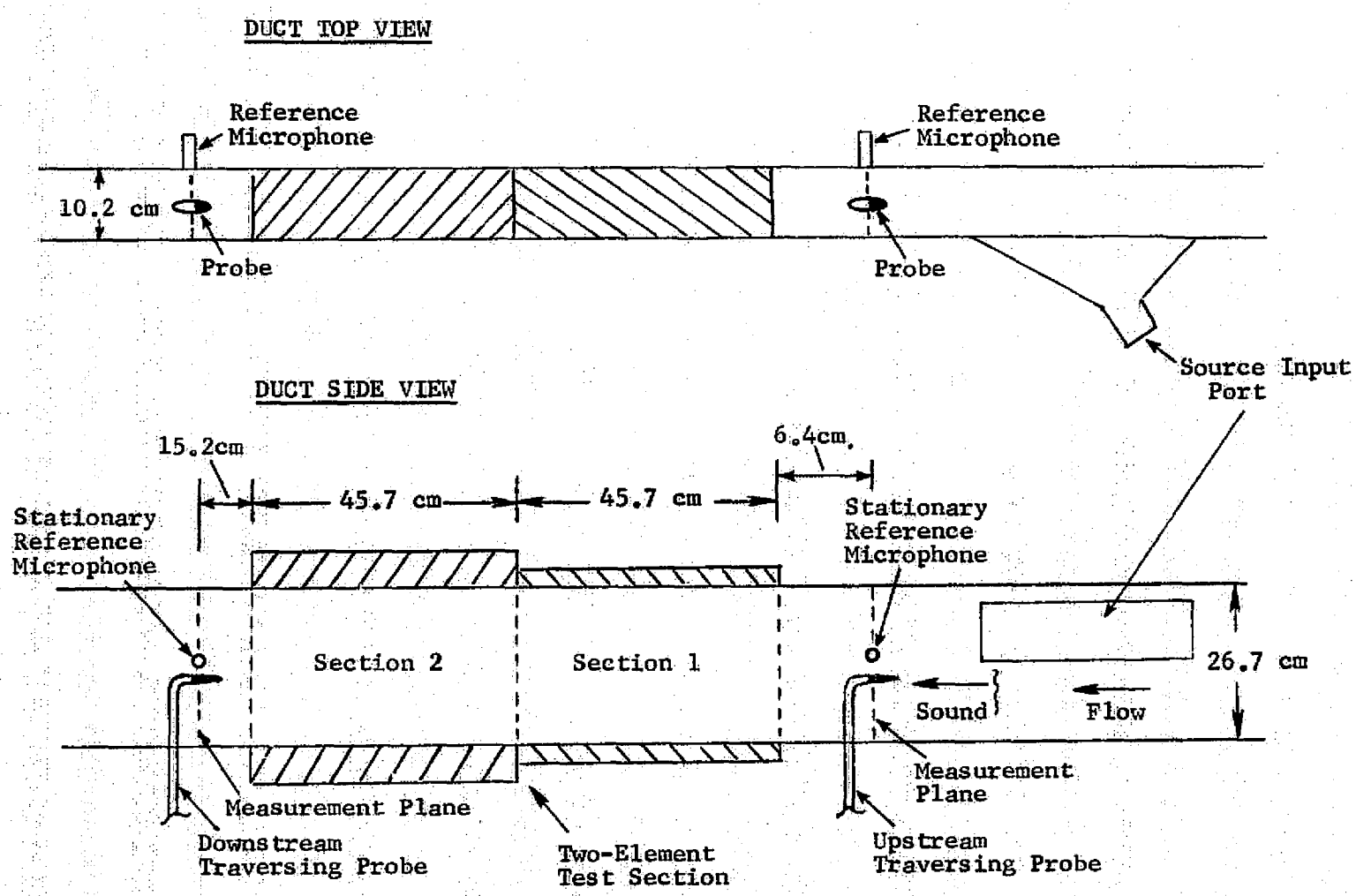

Figure 23. Rectangular Duct Test Configuration.

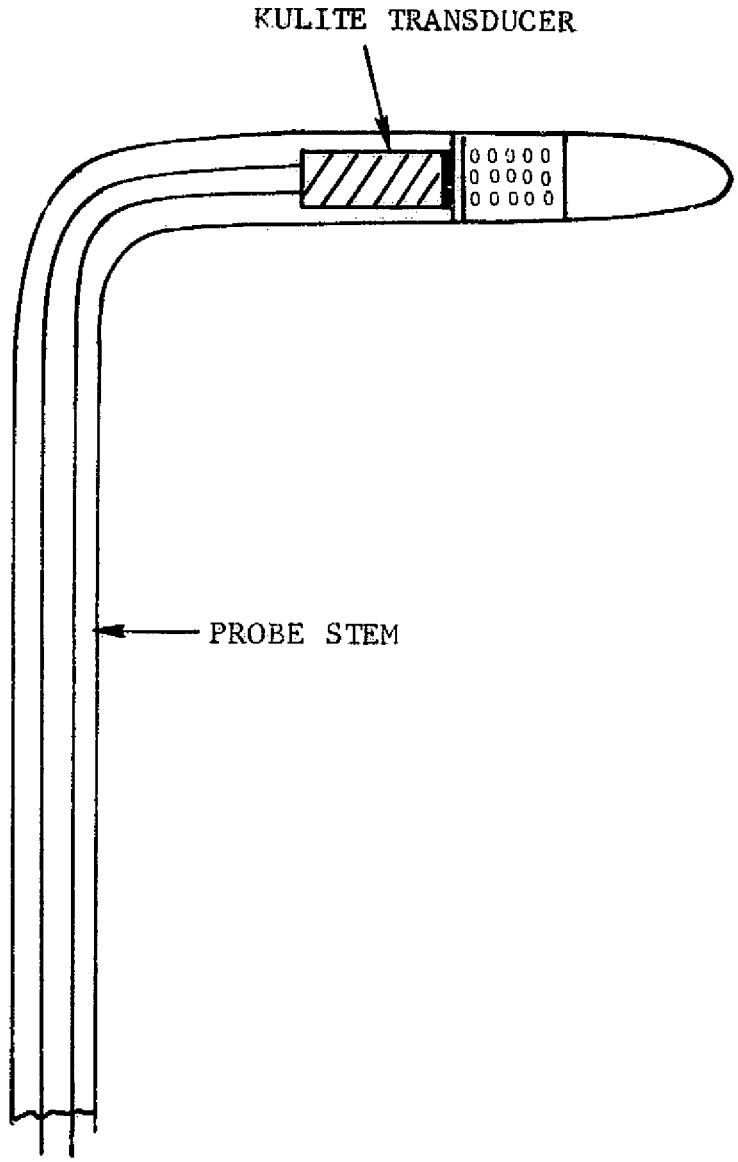

Figure 24. Schematic of Tip-Mounted Probe with Kulite Transducer.

preamplifiers were used for each Kulite. The tip-mounted Kulite probes were used for both continuous SPL traverses and modal measurements.

The modal measurements required the determination of the cross-spectral density between the probe and a reference microphone as a function of probe immersion across the duct (see Section 2.3). The reference microphones were B&K 1/4-inch (0.635 cm) microphones mounted flush in the sidewall of the duct at the same axial positions as the traversing probes (see Figure 23). The cross-spectrum was found using a Princeton Applied Research Model 101A Correlator and Model 102 Fourier Analyzer. These instruments can be set to read out the magnitude and phase of the cross-spectrum at a single frequency while the probe is traversed across the duct. Using a 20-second calculation time constant in the analyzer, the probe was slowly traversed across the duct as the analyzer continuously updated the calculation. This method allows a continuous plot of the cross-sectrum (and thus complex acoustic pressure) profile to be obtained at the frequency of interest.

4.2 PRELIMINARY TESTS

The analytical optimization study requires the modal participation at the designated source plane as input to the computation. Before initiation of the analytical study, a modal measurement was performed in the 26.7 cm high duct in a hardwall configuration to supply this input. It was assumed that the source characteristics would not change appreciably for the treatment configurations to be tested later.

Figure 25 shows the complex pressure profile obtained at 2000 Hz and Mach 0.3 in the duct. Figure 26 presents the modal decomposition of this signal in hardwall rectangular duct modes. Figures 27 and 28 show the complex profile and modal expansion for the signal at 2000 Hz and Mach 0.0, which was also measured at this time.

4.3 PHASE I TEST PROGRAM

4.3.1 Objectives

The objective of this first series of tests was to demonstrate the optimized two-element treatment design found by analysis. The analytical results indicated that attenuation would be maximized if the two treatment sections were given the following impedances (see footnote in Section 3.2):

Section 1 (Upstream) $Z/\rho c = 0.7 - 1.4i$

Section 2 (Downstream) $Z/\rho c = 0.9 - 0.7i$

This design is based on a source characterized by the modal participation given by Figure 26, at a mean flow of Mach 0.3 and a frequency of 2000 Hz. The predicted attenuation in PWL under these conditions is 29.3 dB.

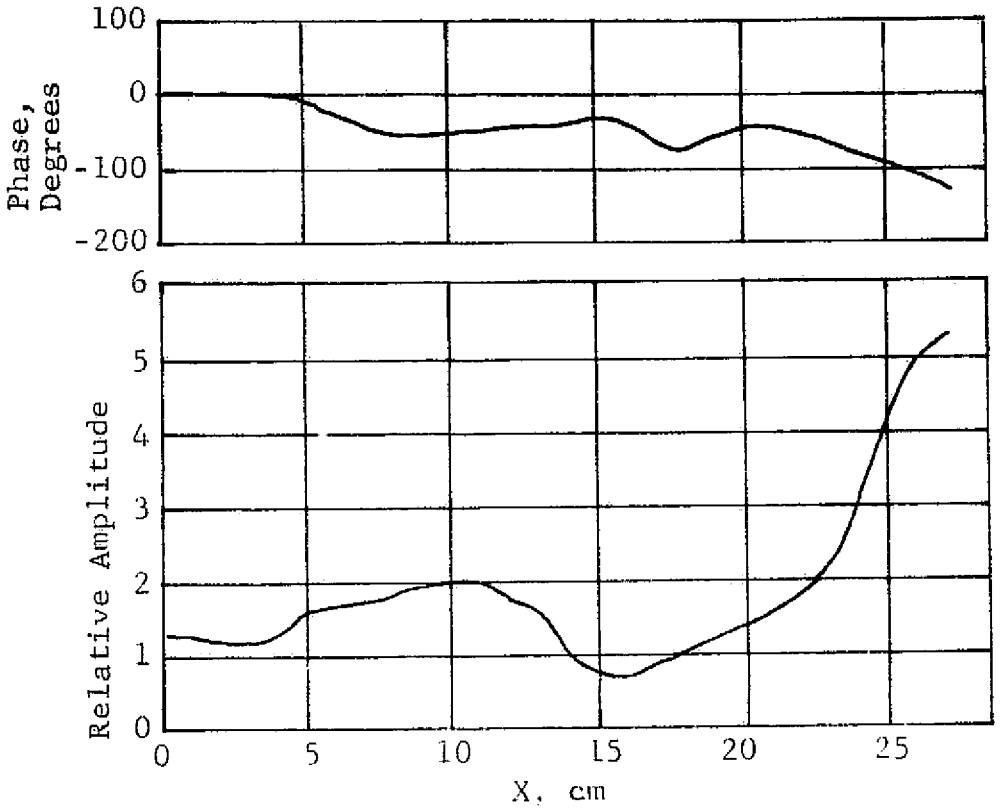

Figure 25. Complex Pressure Profile, Upstream Probe, Preliminary Experiment, Mach 0.3, 2000 Hz.

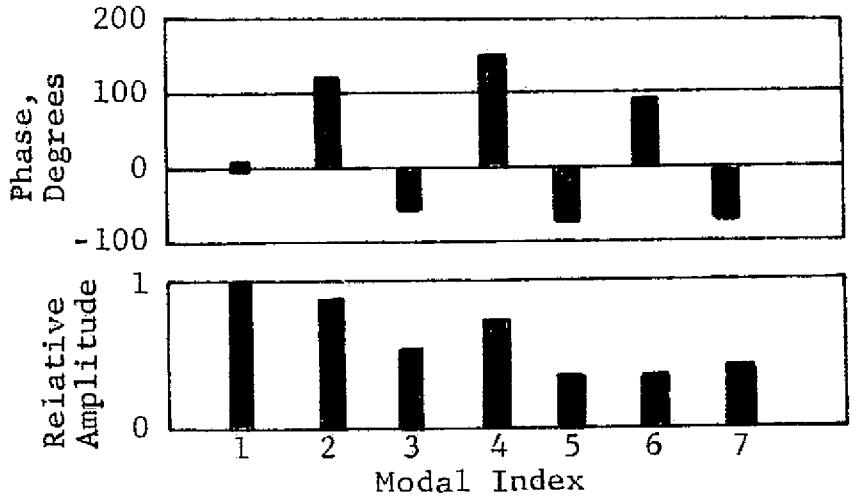

Figure 26. Modal Participation, Preliminary Experiment, Mach 0.3, 2000 Hz. (Repeat of Figure 11).

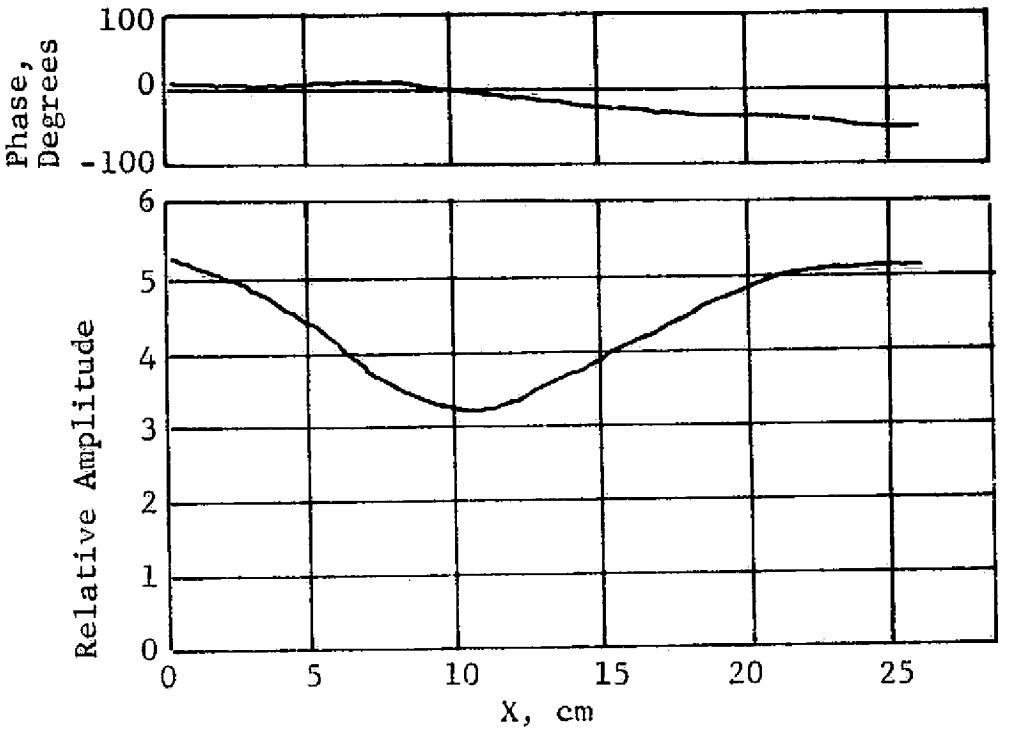

Figure 27. Complex Pressure Profile, Upstream Probe, Preliminary Experiment, Mach 0.0, 2000 Hz.

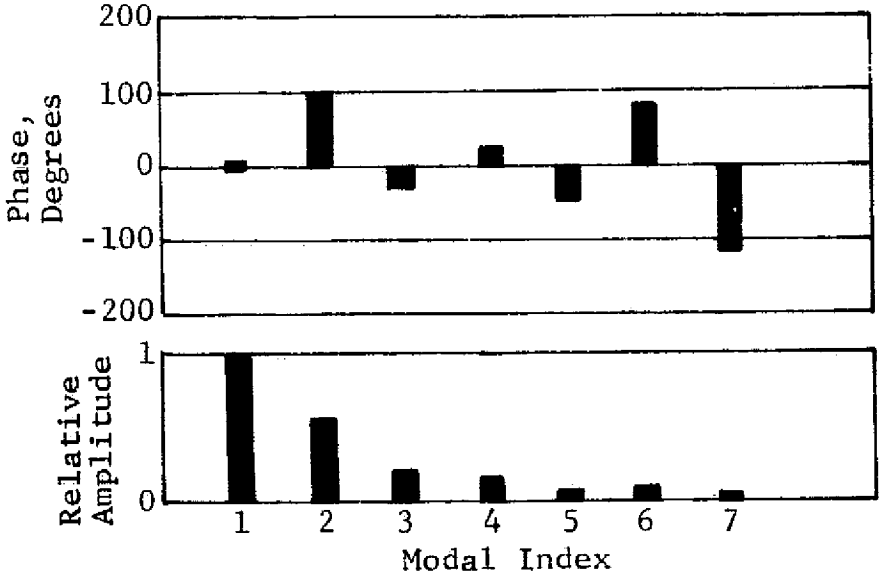

Figure 28. Modal Participation, Preliminary Experiment, Mach 0.0, 2000 Hz. (Repeat of Figure 10).

4.3.2 Treatment Design and Test Program

The type of treatment to achieve the optimum impedance components was chosen to be single-degree-of-freedom (SDOF) perforated plate - honeycomb cell sandwich panel. The acoustic properties of these SDOF panels have been established[9],[10] design parameters (faceplate porosity, thickness, hole diameter, honeycomb cavity depth) to the wall impedance. Preliminary design of the treatment was made using the following expression for resistance

$$R/\rho c = \frac{0.3M}{\sigma} \tag{47}$$

where M is duct Mach number and σ is faceplate porosity. The following expression was used for the reactance

$$X/\rho c = \frac{(t_p + \delta)\omega}{\sigma} - \cot k\ell \tag{48}$$

where t_p is faceplate thickness, ω is circular frequency, k is the wavenumber, ℓ is the cavity depth, and δ is an empirical end correction depending upon hole diameter and Mach number.[11] Using results of these impedance calculations as a guide, the six configurations listed in Table III were chosen to be tested.

For each of the configurations, ΔPWL measurements were made for third-octave bandwidths from 500 to 10,000 Hz and for a 50 Hz bandwidth narrowband at 2000 Hz. For the third-octave measurements, the duct was excited by a high intensity source signal which was filtered in a third-octave bandwidth at 800 Hz. In this case, the higher frequency noise occurs due to rich higher harmonic content of the 800 Hz signal. For the 2000 Hz narrowband, the input signal was broadband noise filtered in a third-octave bandwidth about 2000 Hz with a super-improved 2000 Hz pure tone. The treatment configuration demonstrating the greatest ΔPWL for the 2000 Hz narrowband was subjected to detailed modal measurements for correlation with analysis.

4.3.3 Test Results

Figures 29 to 34 are plots of the measured third-octave ΔPWL suppressions for the six Phase I test configurations, respectively, for Mach 0.0, 0.2, 0.3, and 0.4. Table IV lists the 2000 Hz narrowband ΔPWL's for the six configurations.

Examination of the measured third-octave suppression curves in Figures 29 to 34 indicates that in most cases a higher suppression was obtained at 2500 Hz than at 2000 Hz. This can be explained by the presence of a strongly excited higher order mode which becomes cut-on in the center of the 2500 Hz band. The treatment is very effective in attenuating this particular mode even though it is designed for 2000 Hz.

Table III. Phase I Test Configuration Definition.

	SECTION 1		SECTION 2	
	Porosity	Cavity Depth	Porosity	Cavity Depth
Config. 0	HARDWALL		HARDWALL	
Config. 1	14%	1.5 cm (0.6 In.)	10%	2.3 cm (0.9 In.)
Config. 2	14%	1.5 cm (0.6 In.)	7.5%	1.5 cm (0.6 In.)
Config. 3	10%	1.3 cm (0.5 In.)	7.5%	1.5 cm (0.6 In.)
Config. 4	10%	1.3 cm (0.5 In.)	10%	2.3 cm (0.9 In.)
Config. 5	14%	1.5 cm (0.6 In.)	14%	2.3 cm (0.9 In.)
Config. 6	22.7%	1.5 cm (0.6 In.)	10%	2.3 cm (0.9 In.)

All faceplate thicknesses .08 cm, all hole diameters .16 cm

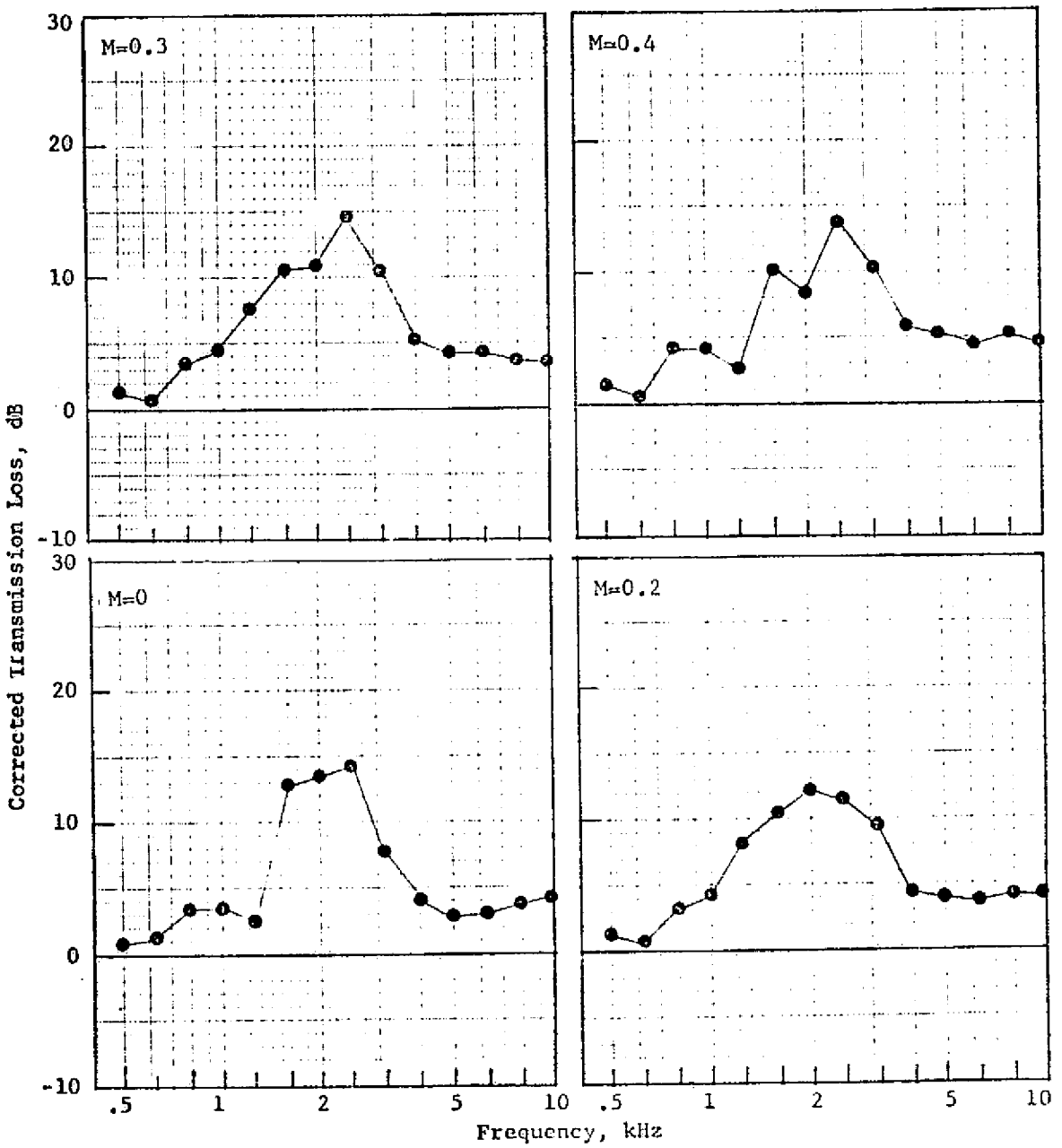

Figure 29. Measured Third-Octave Transmission Loss, Configuration 1.

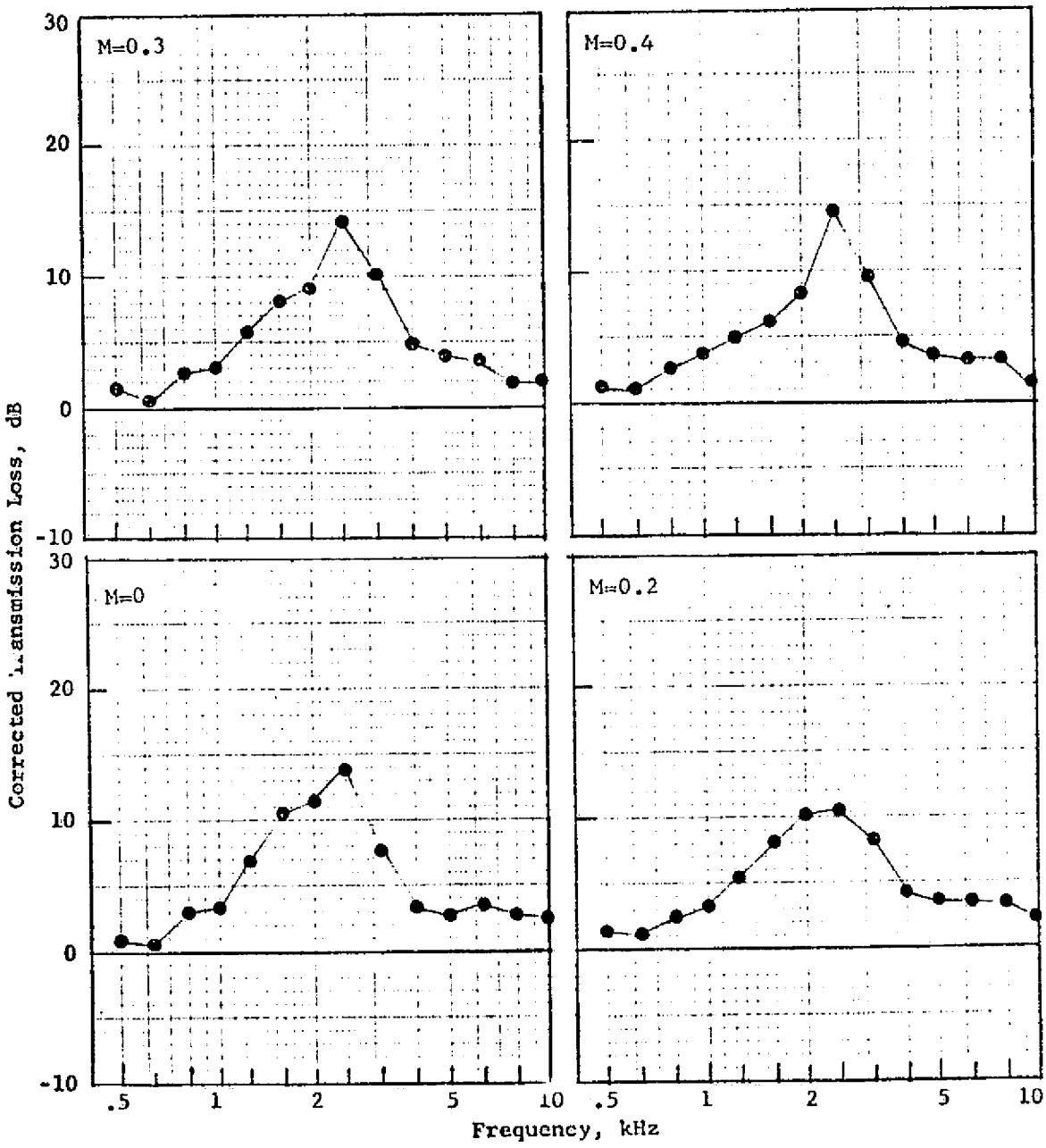

Figure 30. Measured Third-Octave Transmission Loss, Configuration 2.

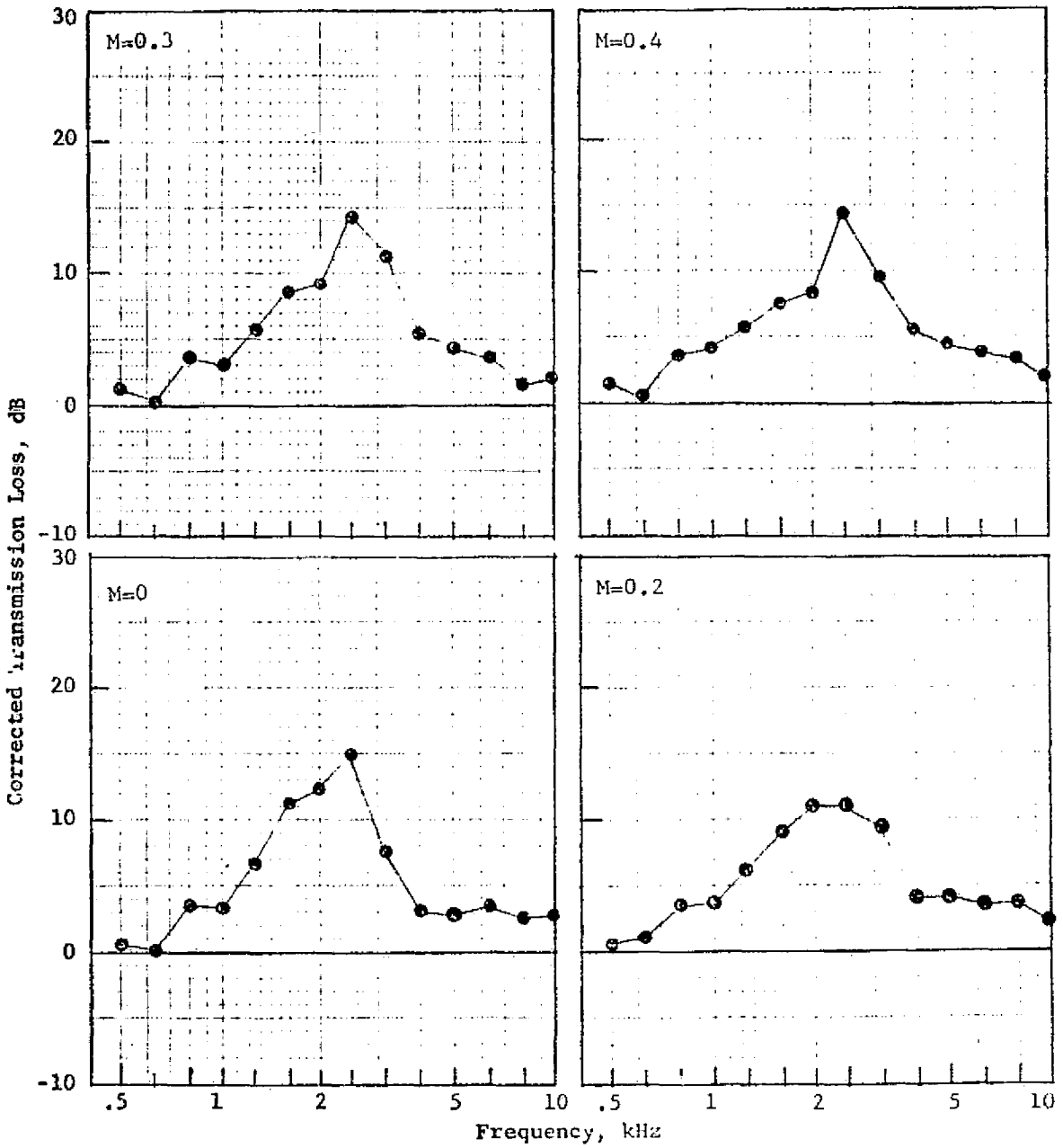

Figure 31. Measured Third-Octave Transmission Loss, Configuration 3.

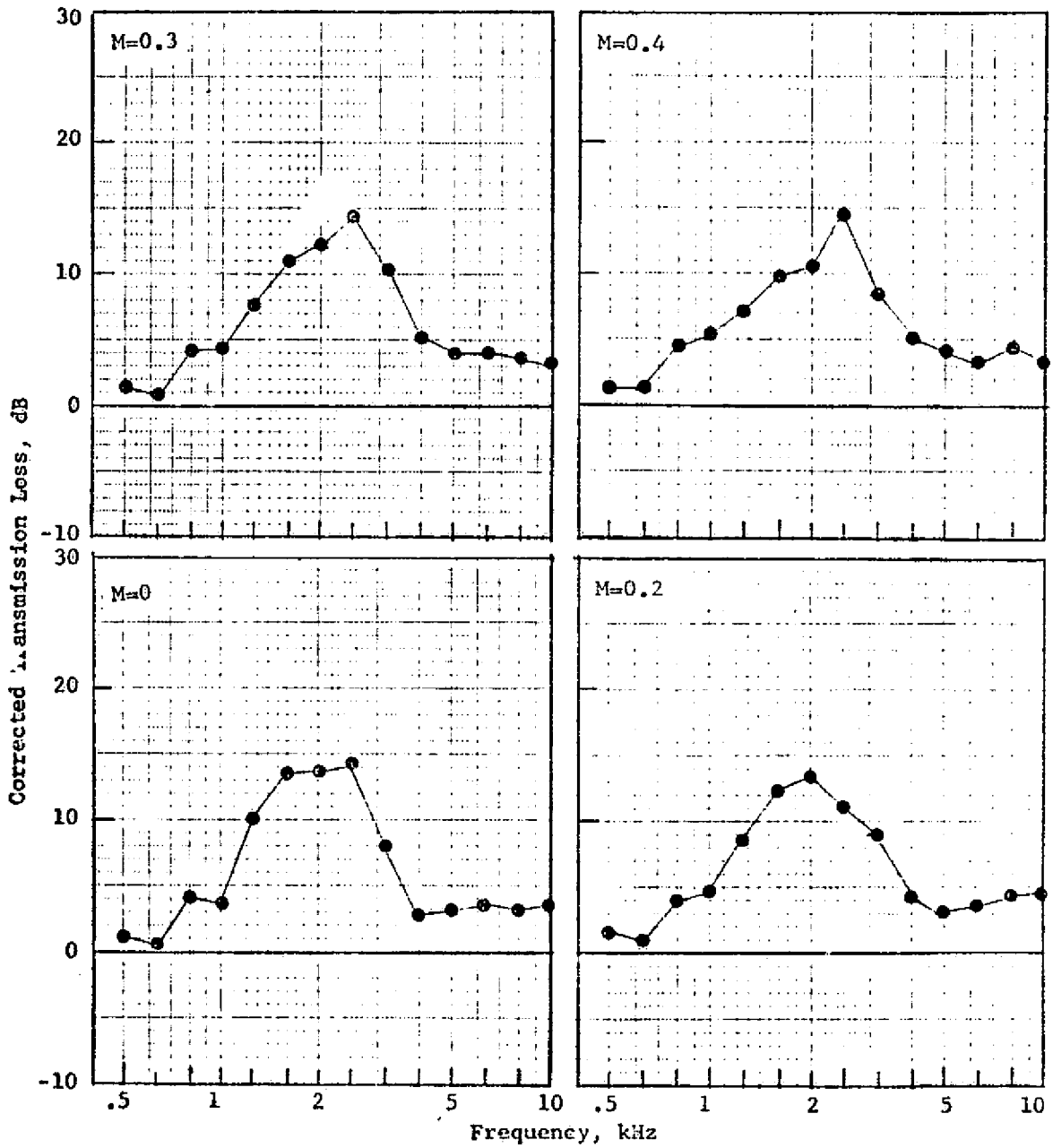

Figure 32. Measured Third-Octave Transmission Loss, Configuration 4.

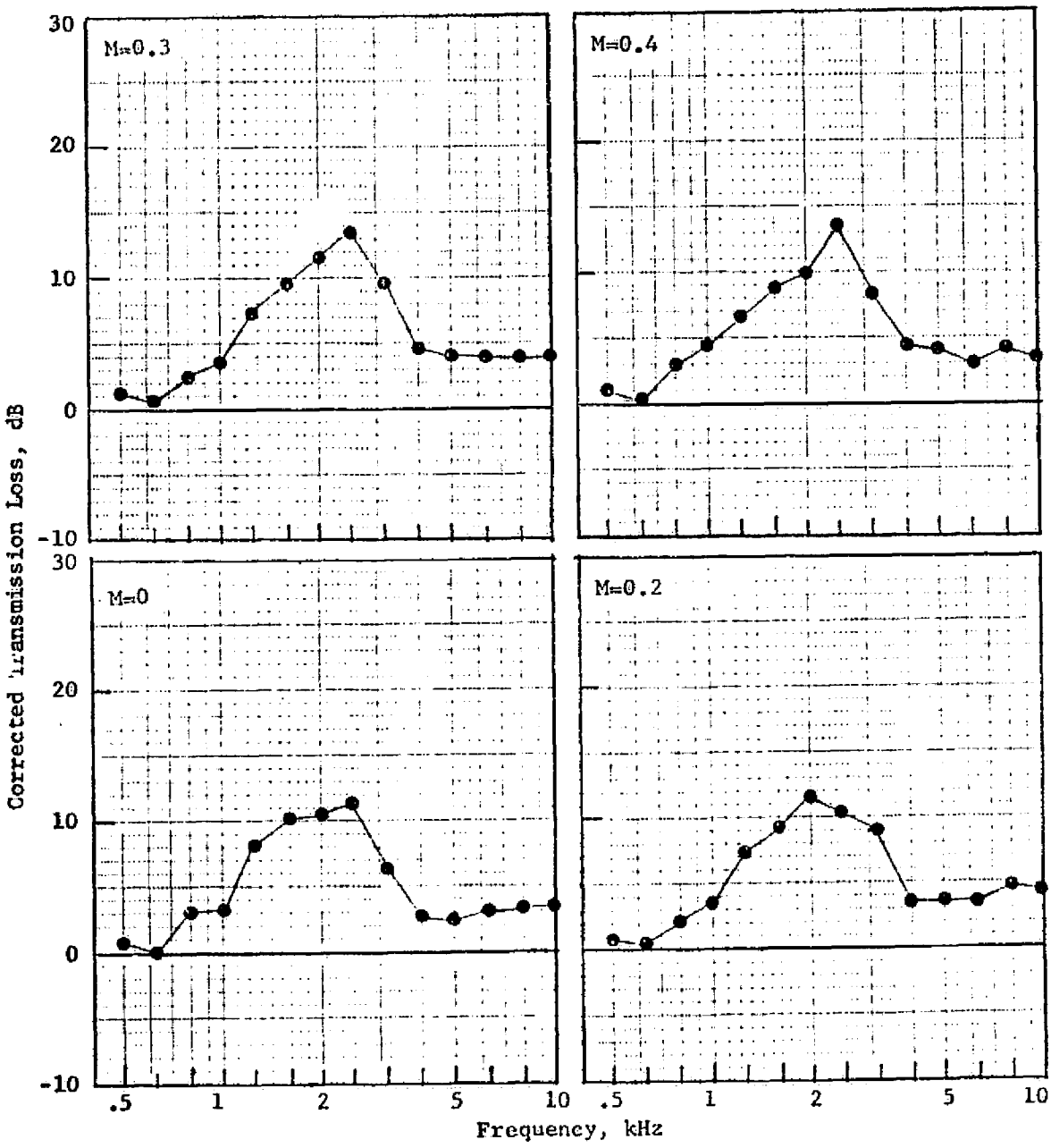

Figure 33. Measured Third-Octave Transmission Loss, Configuration 5.

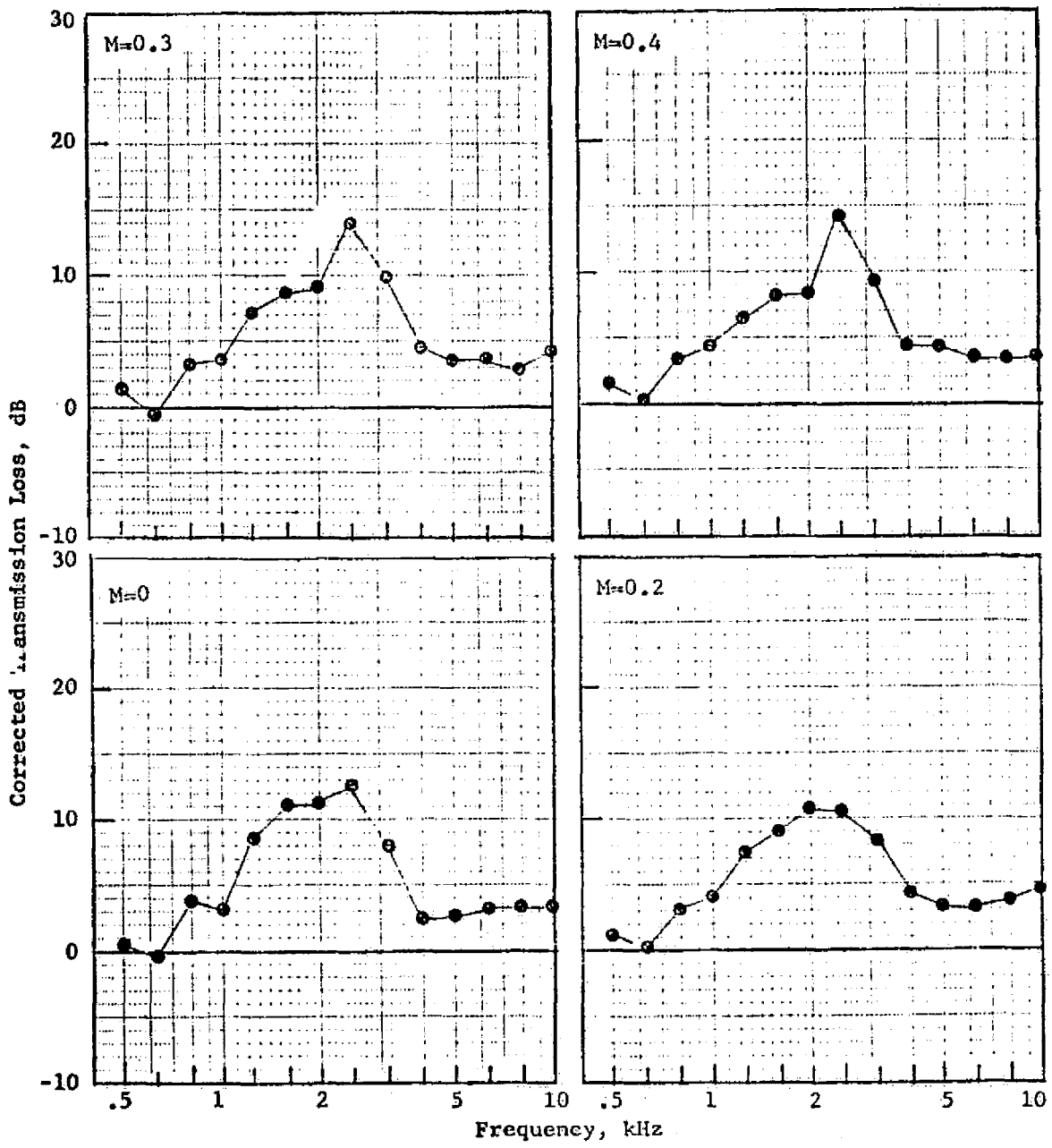

Figure 34. Measured Third-Octave Transmission Loss, Configuration 6.

Table IV. Phase I Test Results - Measured Narrowband Transmission Loss at Mach 0.3, 2000 Hz.

	SECTION 1	SECTION 2	ΔPWL, dB
Config. 1	(14%, 1.5 cm)	(10%, 2.3 cm)	-17.5
Config. 2	(14%, 1.5 cm)	(7.5%, 1.5 cm)	-11.0
Config. 3	(10%, 1.3 cm)	(7.5%, 1.5 cm)	-12.5
Config. 4	(10%, 1.3 cm)	(10%, 2.3 cm)	-19.0
Config. 5	(14%, 1.5 cm)	(14%, 2.3 cm)	-17.0
Config. 6	(22.7%, 1.5 cm)	(10%, 2.3 cm)	-13.5
Config. 4 (Repeat)	(10%, 1.3 cm)	(10%, 2.3 cm)	-21.5

In Figure 35 an empirically determined rectangular duct suppression prediction curve, based on the results of a large number of duct tests of single-element liners, is compared to the measured third-octave suppression for Configuration 4. Also plotted on the Mach 0.3 graph are the 2000 Hz narrowband and third-octave measurements made with the 2000 Hz third-octave source, which, as noted above, was different from the source used for the rest of the third-octave measurements. Note that the different source characteristics at 2000 Hz have given a difference in measured suppression of 3.5 dB. The narrowband measurement, made at only one frequency, shows an increase of 5.5 dB over the third-octace with the same source characteristics.

At Mach 0.0 and 0.2, the measured suppression agrees quite closely with the empirical prediction curves for single-element liners. At the design Mach number of 0.3, the two-element measured suppression using the 2000 Hz third-octave source characteristic (more representative of design conditions) exceeds the empirical prediction for the best single phase liner by about 3.5 dB. For third-octave frequencies above 2000 Hz, the measured suppression exceeds the empirical prediction by a substantial margin. At Mach 0.4, the high frequency enhancement of the two-element liner is still in evidence, although no improvement over the empirical data is noted at 2000 Hz.

One can conclude that in this case the two-element liner does not appear to offer a significant advantage over the single-element liners for frequencies lower than the design frequency, but provides significantly enhanced suppression for higher frequencies at Mach numbers equal to or greater than the design Mach number. Note that the narrowband suppression peak within the 2000 Hz third-octave, at the design condition, is very sharp with respect to the overall third-octave band suppression.

Configuration 4, which came closest to the predicted optimum suppression of 29.3 dB, was chosen for detailed modal measurements. A repeat narrowband ΔPWL measurement of this configuration gave a suppression of 21.5 dB overall (compared with 19.0 dB previously) and 8 dB over the first section of treatment only. The complex pressure profile at the upstream probe location is shown in Figure 36, and its expansion into duct modes in Figure 37. This variation in measurement was apparently caused by slight differences in modal content, as evidenced by somewhat different SPL traverse profiles for the two cases. In subsequent testing it was found that slight differences in modal content can be expected in the duct with each different test case, and that these small differences in modal content could produce ΔPWL variations of this magnitude. This effect is considered in more detail below.

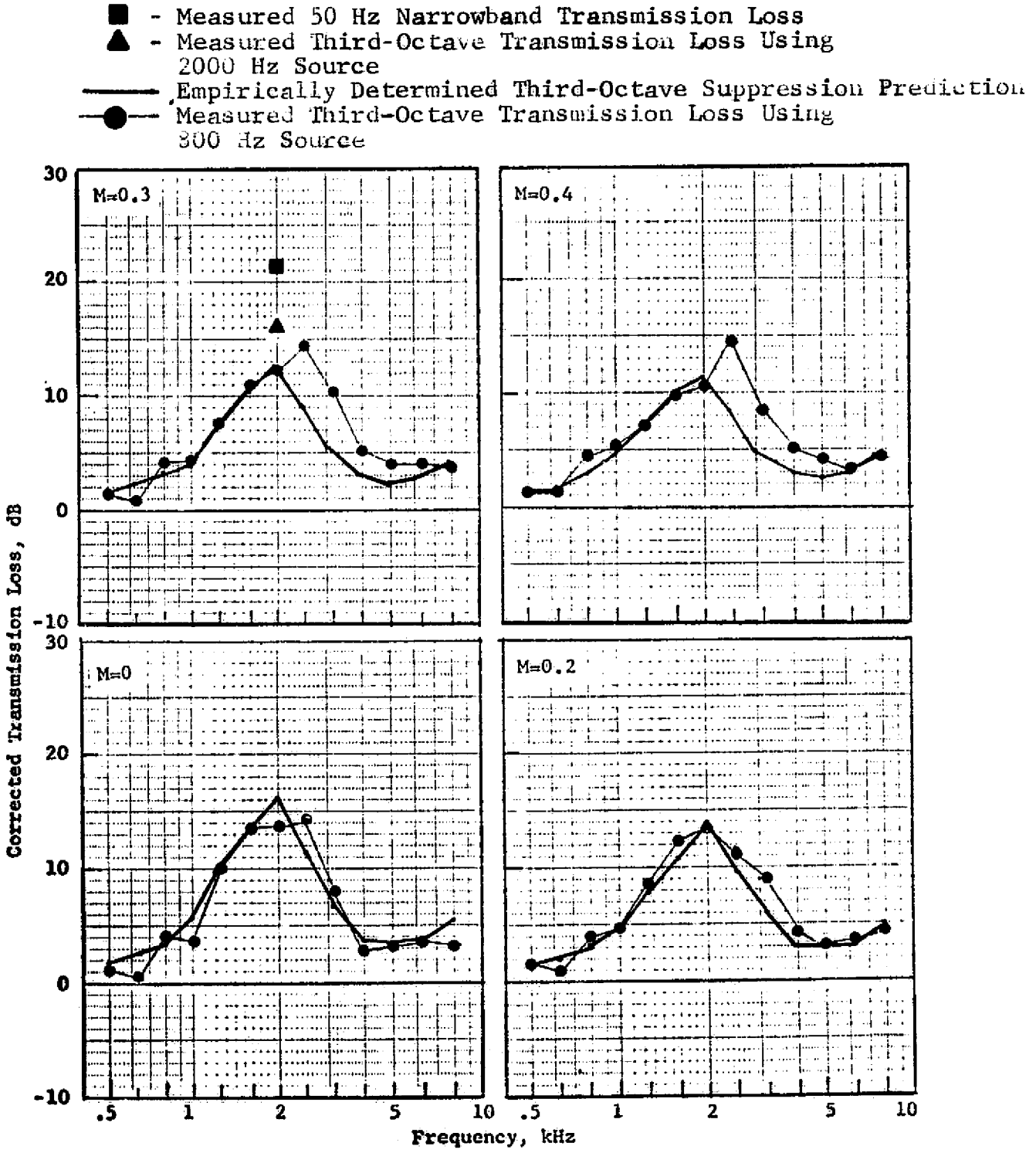

Figure 35. Measured Third-Octave Transmission Loss, Configuration 4, Compared to Empirical Prediction for Rectangular Duct.

Measured Third-Octave Data from Figure 32.

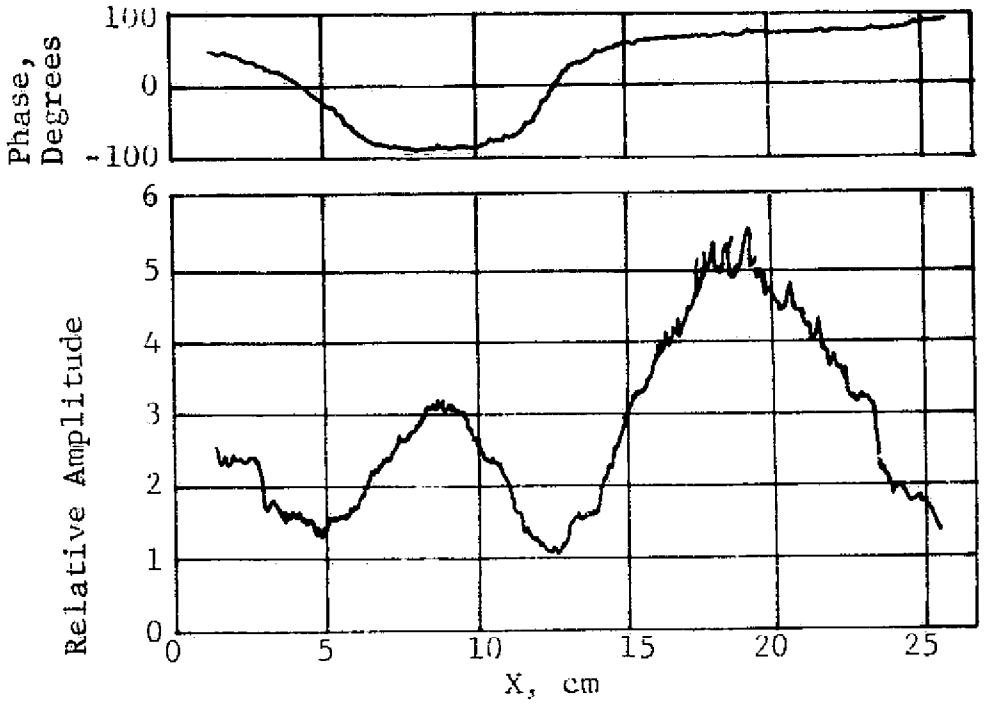

Figure 36. Complex Pressure Profile, Upstream Probe, Configuration 4, Mach 0.3, 2000 Hz.

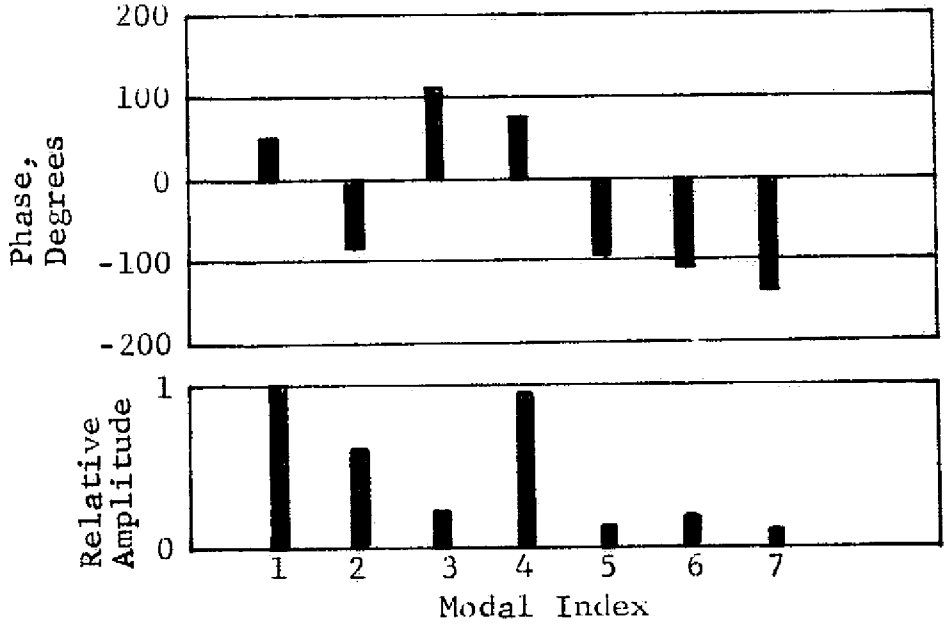

Figure 37. Modal Participation, Configuration 4, Mach 0.3, 2000 Hz.

4.3.4 Analytical Correlations

Based on the modal measurements taken at the plane of the upstream probe, an analytical prediction of the suppression was made. For these calculations at Mach 0.3, the liner impedances were taken to be (Equations 45 and 46):

Section 1 (10% porosity, 1.3 cm deep), $Z_1/\rho c = 0.9 - 1.4i$

Section 2 (10% porosity, 2.3 cm deep), $Z_2/\rho c = 0.9 - 0.7i$

The results are:

	Measured	Calculated
ΔPWL in Section 1	8 dB	6.0 dB
Overall ΔPWL	19 to 21.5 dB	20.6 dB

These results indicate that the suppression was predicted quite closely for the given modal input and liner impedance. Neither the modal input nor the liner impedance is exactly the same as the conditions used for the optimization analysis, which explains why the predicted 29.3 dB for the optimized case was not reached. Figure 38 shows a comparison of the modal content for the original set of optimization modes and those in the input signal to configuration 4. This variation in modal content is discussed below. Note for reference that the predicted uniform liner optimum suppression was 21.6 dB.

4.4 PHASE II DUCT TESTS

4.4.1 Phase II Test Objectives and Reoptimization of Design

The results of the Phase I testing indicated that the optimization conditions were not met in two respects; first, the modal content had changed, and second, the impedances differed from the optimum values. The objective for the second phase of the test program was to allow a second iteration at meeting the optimum design conditions. It was decided to reoptimize the design of the two-element liner based on the new modal content measured in Configuration 4 of the Phase I tests.

Using the modal input defined in Figure 37, the following design was found to maximize suppression for the two-segment liner with equal length segments at 2000 Hz, Mach 0.3,

Section 1 Impedance, $Z_1/\rho c = 0.6 - 1.2i$

Section 2 Impedance, $Z_2/\rho c = 0.7 - 0.5i$

Overall Attenuation $\Delta PWL = -35.9$ dB

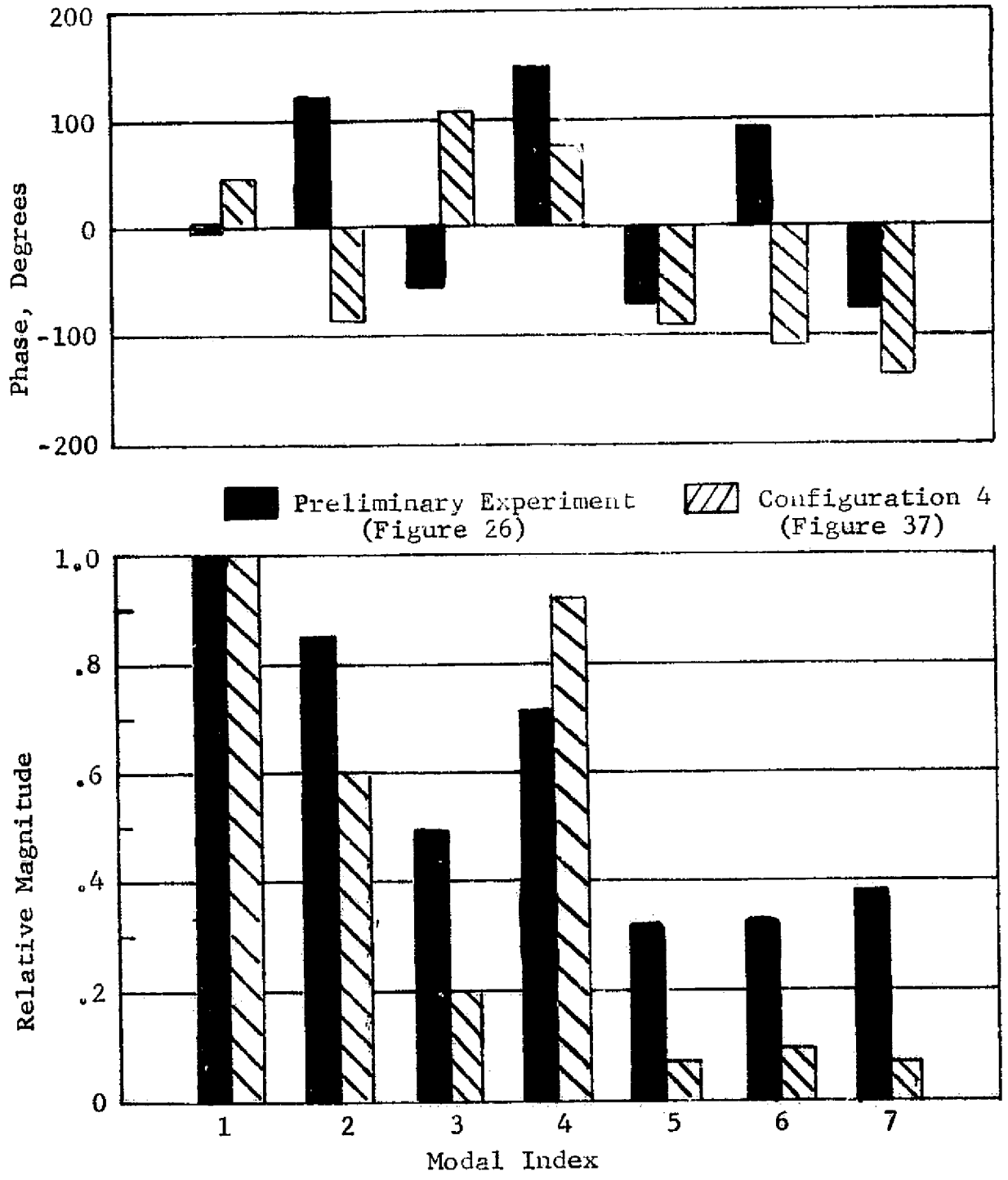

Figure 38. Comparison of Measured Modal Participation, Preliminary Experiment and Configuration 4, Mach 0.3, 2000 Hz.

Note that the impedance values are only slightly changed from the previous optimization case, but the predicted suppression has increased by over 7 dB. This variation is due to the difference in modal content between the two cases.

In addition to testing a treatment configuration to attempt to meet the revised optimization conditions, it was decided that other objectives of Phase II testing would be to investigate the repeatibility of the modal pattern and the sensitivity of the predicted attenuation to uncertainty of the impedance components. If the modal pattern varies appreciably with the treatment configuration, or is highly sensitive to frequency, it would be extremely difficult to obtain the optimum condition, particularly in view of the sensitivity of the peak suppression to the impedance components. The sensitivity to impedance changes about the optimum value is indicated in Table V in which ΔPWL's have been calculated for cases where each of the four specific impedance components has been varied independently by ±0.1 from the optimum value. Using the analytical models for determining the impedance components introduces an unknown amount of error relative to the actual impedance of the liners in the duct. The sensitivity of the predicted suppression to expected errors in impedance component determination was examined.

4.4.2 Phase II Test Configurations

For the Phase II duct tests, the two-element liner was designed to attempt to meet the revised optimization criteria. Based on the analytical impedance models, the following liner parameters were chosen:

Section 1 14% porosity, 1.8 cm (0.7 inch) cavity depth

Section 2 12% porosity, 2.5 cm (1.0 inch) cavity depth

Both sections of this configuration, denoted Configuration 7, had 0.08 cm (0.032 inch) faceplate thickness and 0.16 cm (0.0625 inch) hole diameter. In addition to this configuration, three other configurations were run as part of Phase II testing. The other configurations consisted of Configuration 7 with the order of the segments reversed, and two cases with the same cavity depths as Configuration 7, but with higher and lower porosity of the faceplates, respectively.

4.4.3 Phase II Test Results

A list of the Phase II test configurations with the measured narrowband suppressions for each case is presented in Table VI. The results of the source modal measurements for Configurations 7 to 10 are present in Figures 39 to 46. In evaluating the test results which follow, it is important to note the variation in modal content which occurred from one test configuration to the next. This variation was more than initially hoped, and made achieving the optimum conditions difficult.

Before measuring transmission loss at 2000 Hz for Configuration 7, it was decided to investigate the sensitivity of the tuning to frequency in a

Table V. Calculated Suppression for Two-Element Liner, Configuration 4.

- 2000 Hz
- Mach 0.3

IMPEDANCE Section 1	IMPEDANCE Section 2	△PWL, dB
.6 -1.2i	.7 -.5i	-35.9
.5 -1.2i	.7 -.5i	-30.1
.7 -1.2i	.7 -.5i	-27.5
.6 -1.1i	.7 -.5i	-29.9
.6 -1.3i	.7 -.5i	-27.5
.6 -1.2i	.8 -.5i	-31.9
.6 -1.2i	.6 -.5i	-31.4
.6 -1.2i	.7 -.4i	-30.1
.6 -1.2i	.7 -.6i	-34.7

NOTE: Modal input given by Figure 37.

Table VI. Phase II Test Configuration Defination.

Section	Configuration	Porosity %	Cavity Depth cm	Cavity Depth in.	Nominal Impedance $\%/_{0}c$
1	7	11	1.8	0.7	0.64 - 1.15i
	8	12	2.5	1.0	0.75 - 0.55i
	9	20	1.8	0.7	0.43 - 1.30i
	10	12	1.8	0.7	0.75 - 1.20i
2	7	12	2.5	1.0	0.75 - 0.55i
	8	11	1.8	0.7	0.64 - 1.15i
	9	14	2.5	1.0	0.64 - 0.60i
	10	10	2.5	1.0	0.90 - 0.55i

- 10, 12 and 14% Faceplates are 0.08 cm Thick, 0.16 cm Hole Diameter
- 20% Faceplate is 0.08 cm Thick, 0.08 cm Hole Diameter

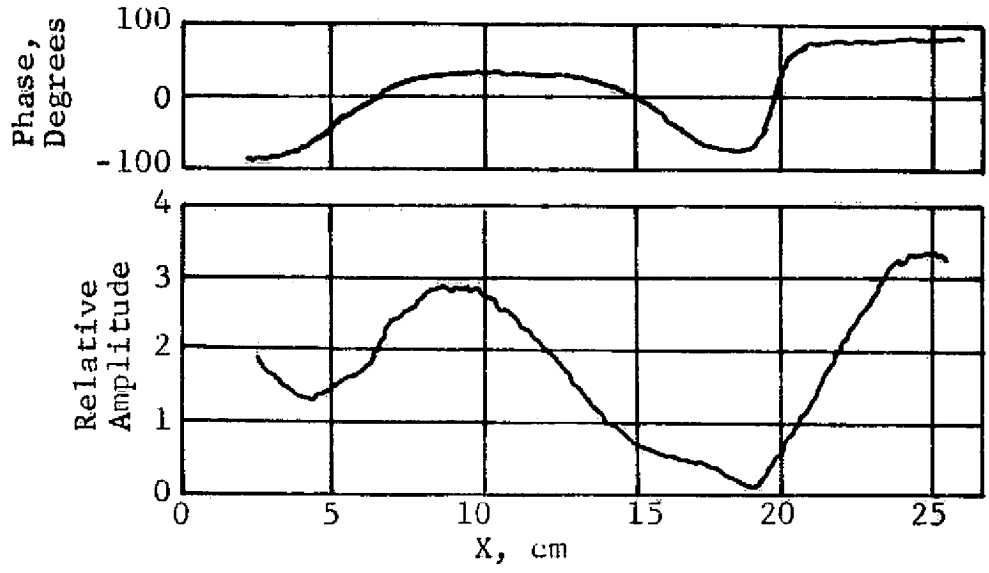

Figure 39. Complex Pressure Profile, Upstream Probe, Configuration 7, Mach 0.3, 1950 Hz.

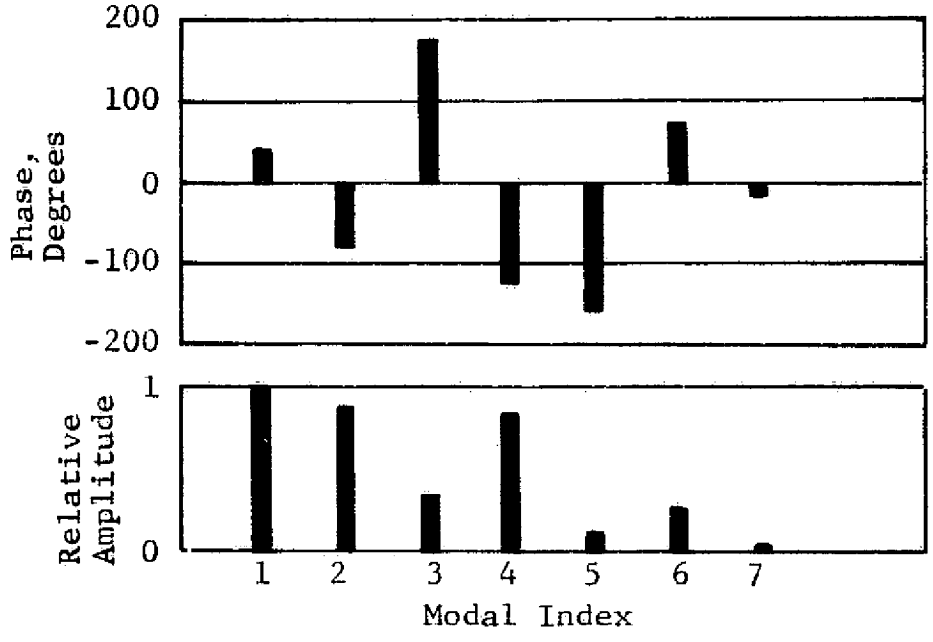

Figure 40. Modal Participation, Configuration 7, Mach 0.3, 1950 Hz.

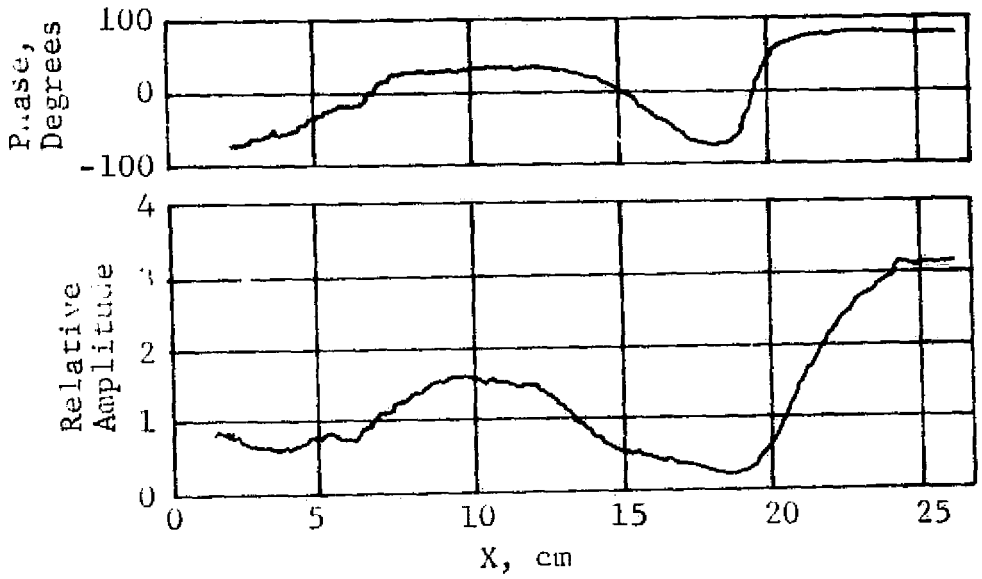

Figure 41. Complex Pressure Profile, Upstream Probe, Configuration 8, Mach 0.3, 1950 Hz.

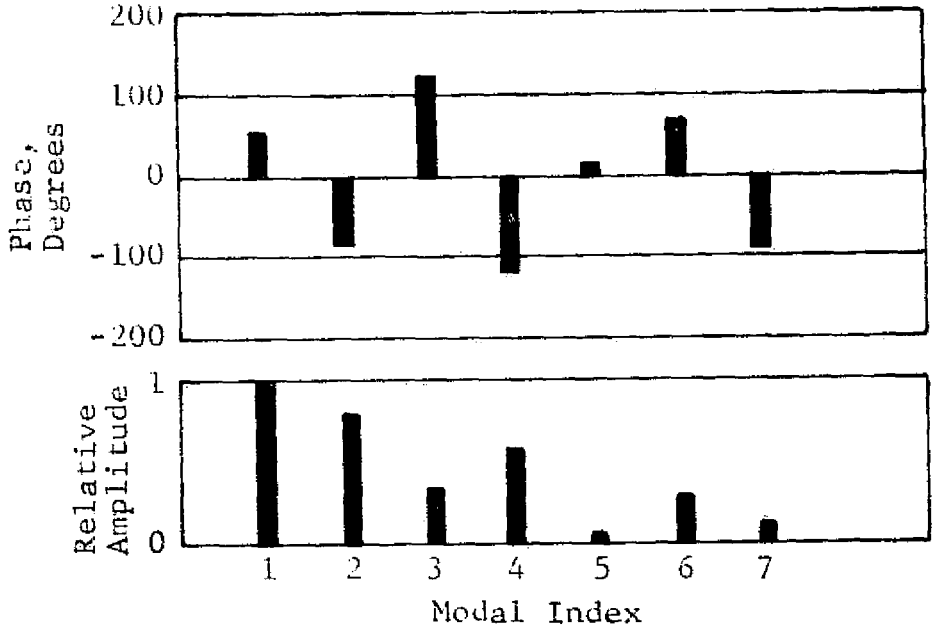

Figure 42. Modal Participation, Configuration 8, Mach 0.3, 1950 Hz.

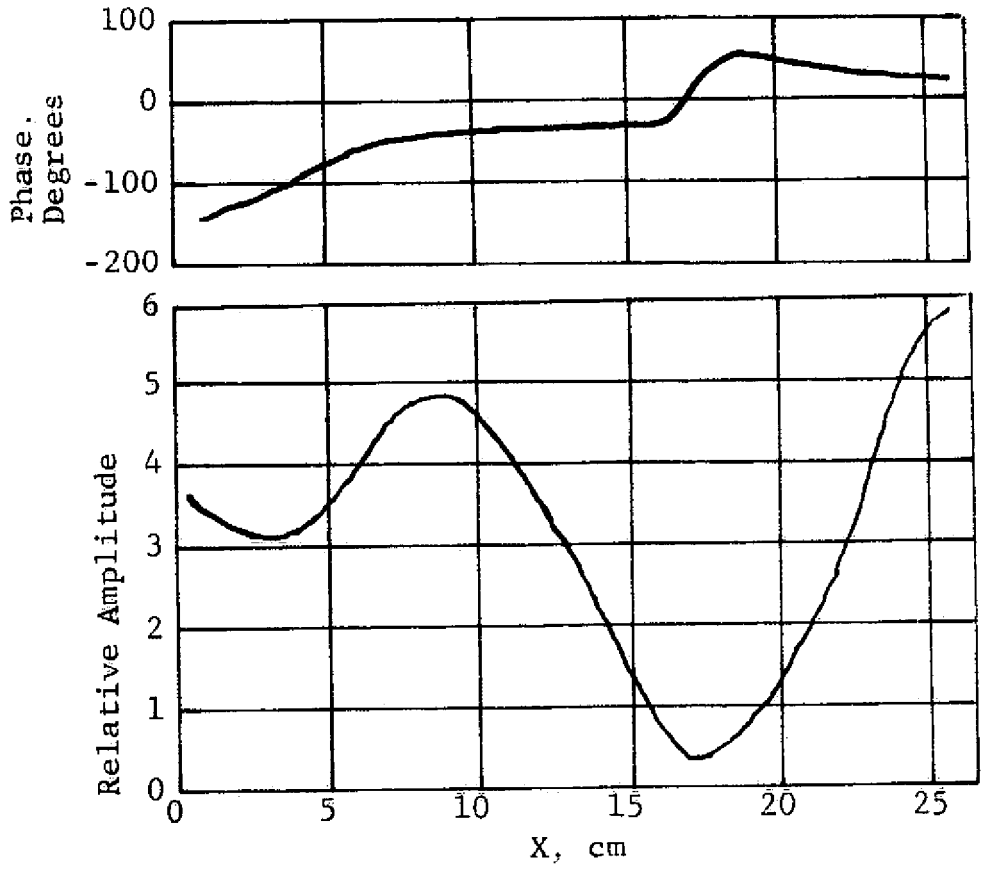

Figure 43. Complex Pressure Profile, Upstream Probe, Configuration 9, Mach 0.3, 1940 Hz.

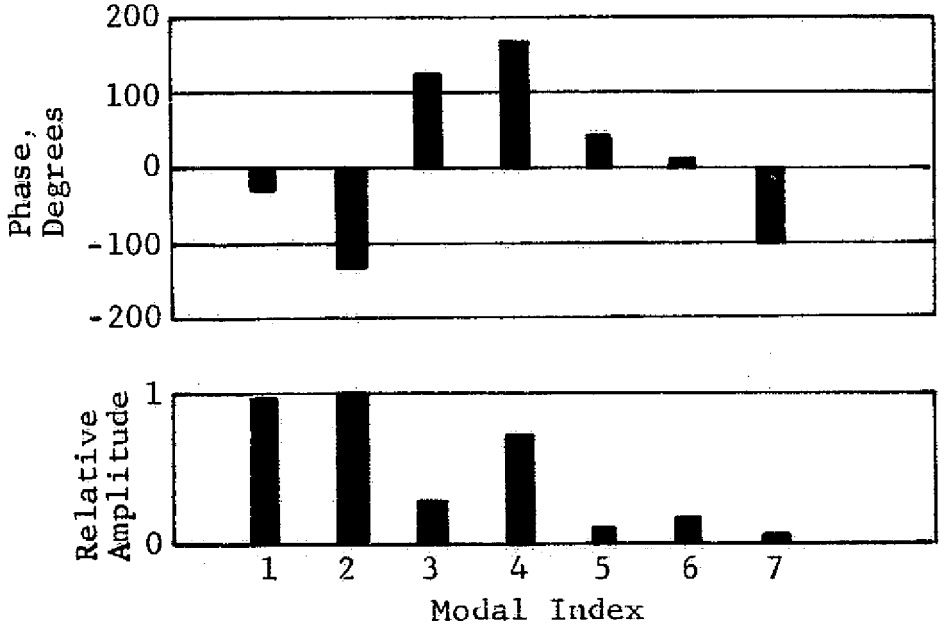

Figure 44. Modal Participation, Configuration 9, Mach 0.3, 1940 Hz.

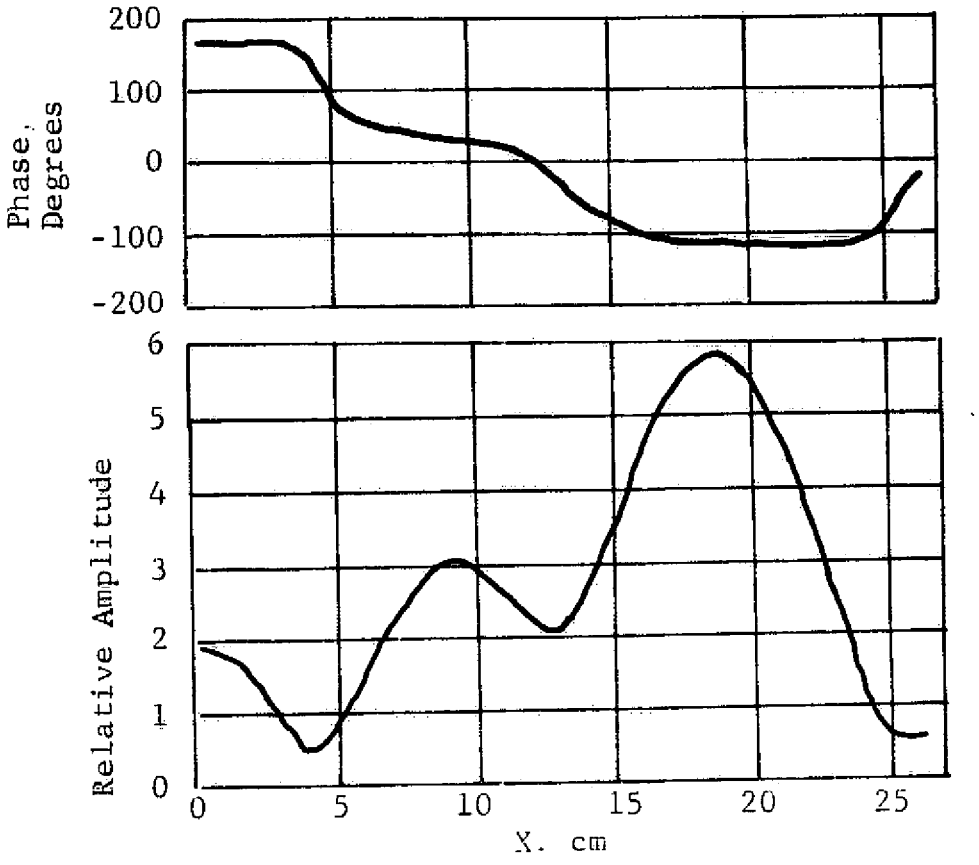

Figure 45. Complex Pressure Profile, Upstream Probe, Configuration 10, Mach 0.3, 1900 Hz.

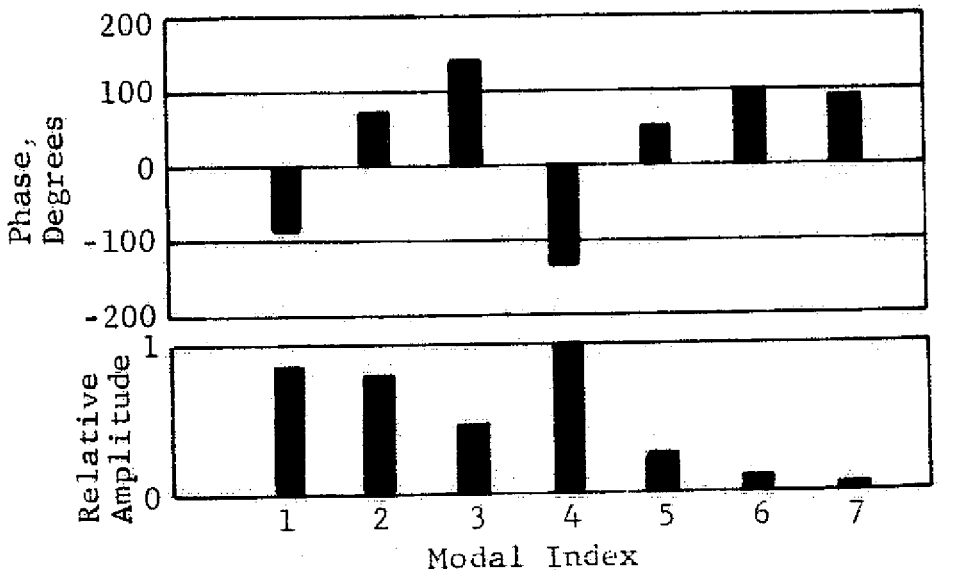

Figure 46. Modal Participation, Configuration 10, Mach 0.3, 1900 Hz.

range about 2000 Hz. To do this, an automatic level control device was connected to the input of the Ling driver such that the sound level at the input plane probe to the duct could be maintained at a constant level as input frequency was slowly swept from 1450 to 2350 Hz, using the upstream probe signal as a feedback control. With both probes in the fully retracted position (near the lower wall), the SPL signals from both probes were recorded in 20 Hz bandwidth during the frequency sweep.

Although the actual ΔPWL cannot be inferred from ΔSPL's at one immersion, from previous data it was felt that the ΔSPL at the lower wall would be representative of the ΔPWL, thus giving an indication of the best tuning frequency. Figure 47 is the result of this frequency sweep. Note that a high ΔSPL occurs at about 1950 Hz, but the ΔSPL right at 2000 Hz is much less. From this, it was decided to take the ΔPWL measurements in a narrowband about 1950 Hz for this configuration. In this and the following cases, the source was excited with a pure-tone and the measurement is in 20 Hz bandwidths.

Figure 48 is the measured narrowband SPL traverse for Configuration 7 for the upstream and downstream probes. The ΔPWL based on these measurements is -20 dB. This falls short of the predicted optimum attenuation by about 16 dB.

Using the modal input given for Configuration 7 by Figure 40, and the analytically determined impedances of

$$\frac{Z_1}{\rho c} = 0.64 - 1.15i$$

$$\frac{Z_2}{\rho c} = 0.75 - 0.55i$$

the suppression predicted for Configuration 7 is 28.3 dB. This overpredicts the measured suppression by over 8 dB. The most likely cause of this discrepancy between the measured and predicted suppression is the error in determining the impedance. An indication of the sensitivity of the analytical program to variations in impedance about the optimum value has already been indicated in Table V. The nominal value of the impedances of the liners in Configuration 7 are all within 0.05ρc of this optimum value, and are predicted to lose only 7.6 dB in suppression from the optimum value, even with the different modal content of Configuration 7, compared to that used for the optimum.

Since there is no way of determining precisely what the impedance components in the duct actually are, a study was made of the expected variation in the impedance components as functions of the independent variables in the analytical impedance expressions, and of the sensitivity of predicted suppression to typical variations of the impedance parameters. This error analysis also gives an indication of the practicality of designing a treatment panel to be optimized for the suppression of a pure-tone or narrowband signal.

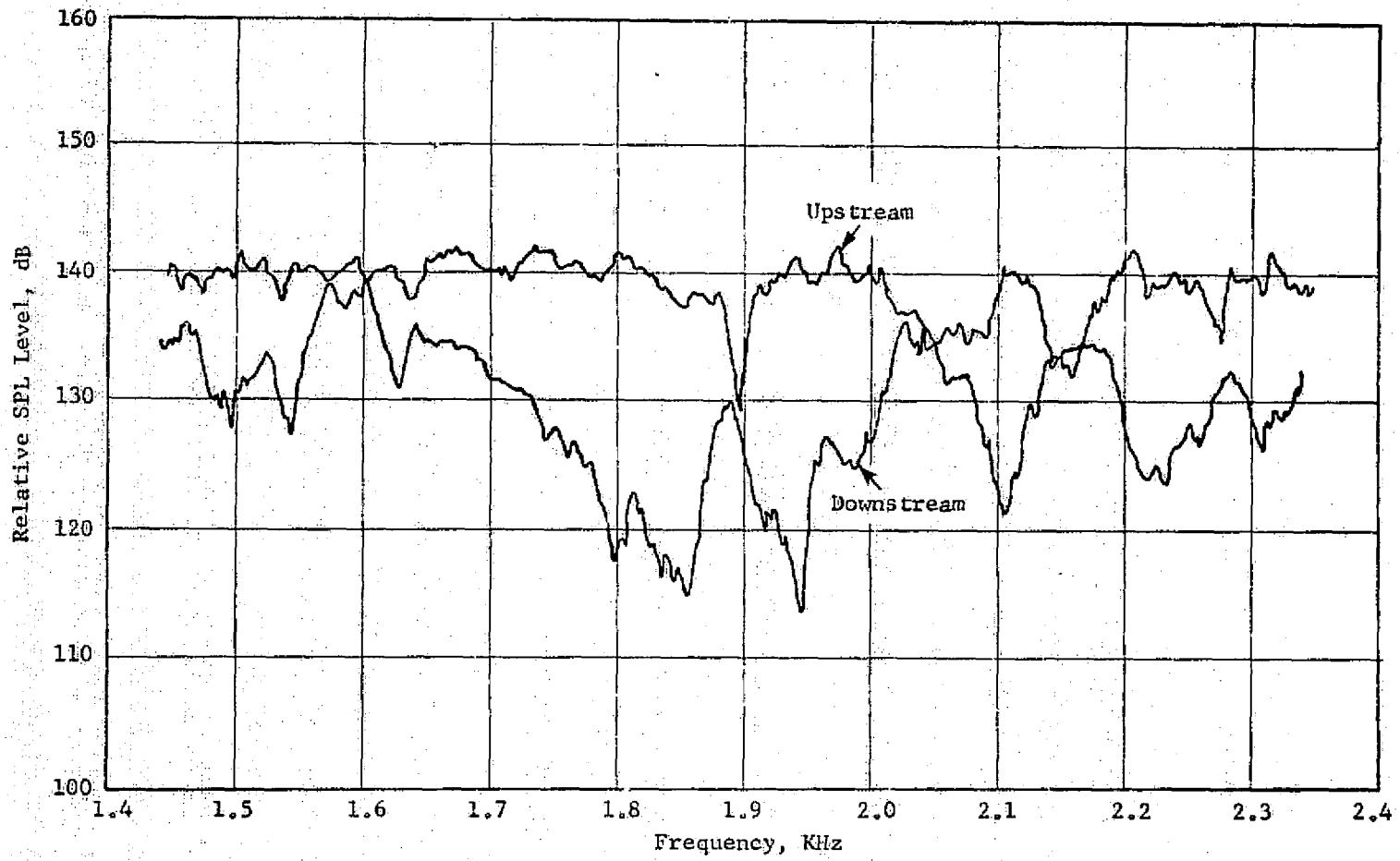

Figure 47. Comparison of Upstream and Downstream SPL Levels for Discrete Tone Frequency Sweep with Both Probes Immersed 1.3 cm into Duct, Configuration 7, Mach 0.3.

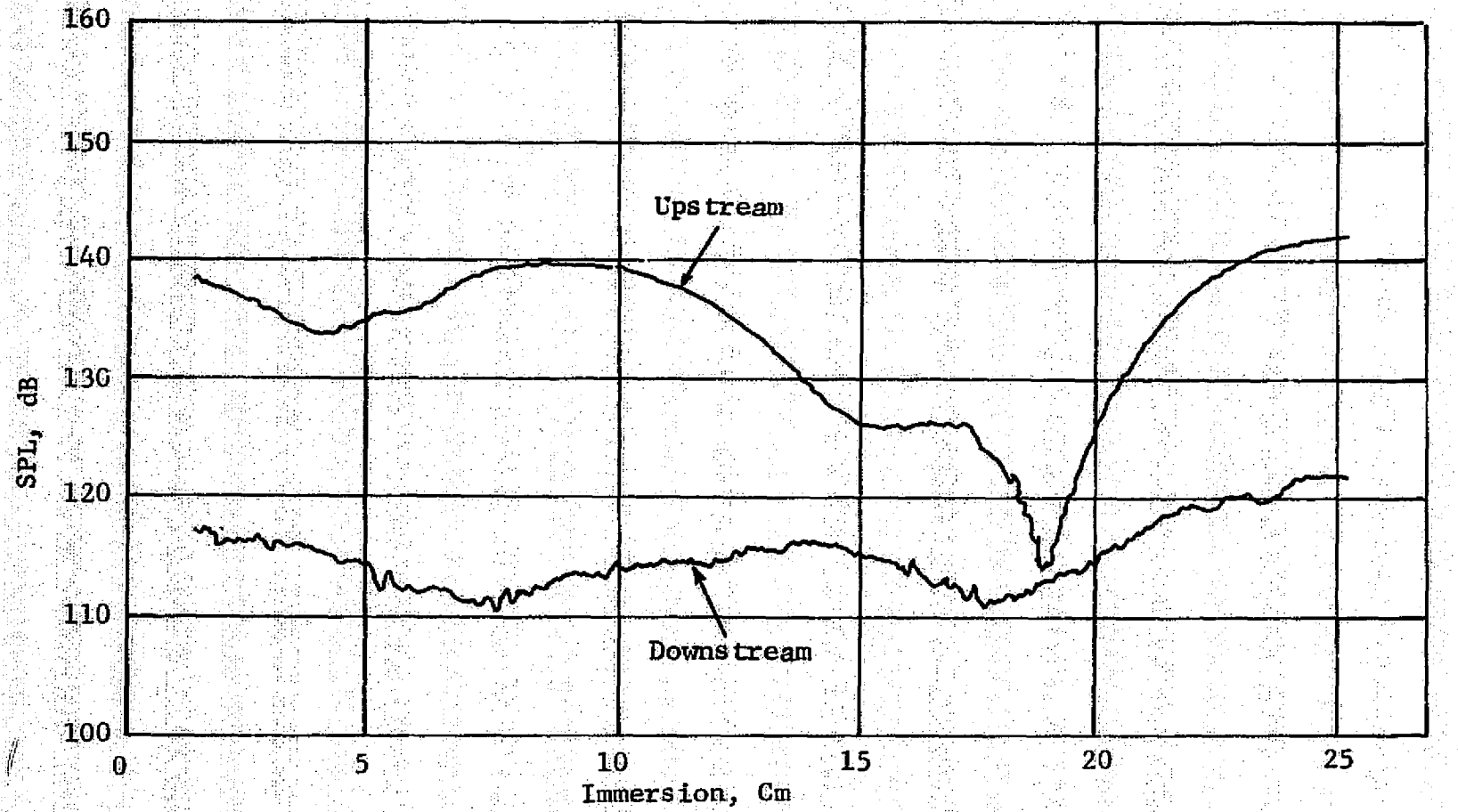

Figure 48. Narrowband (20 Hz Bandwidth) SPL Traverses, Configuration 7, Mach 0.3, 1950 Hz, ΔPWL = 20 dB.

By Equation 45, the significant variables for the resistance model are the Mach number M and the porosity σ. Figures 49 and 50 show the variation of $R/\rho c$ for the two liners over the expected variation in M and σ. The reactance depends upon the porosity; σ, the cavity depth; ℓ, the faceplate thickness; t_p, the frequency; ω, and the end correction δ, which in turn depends on the faceplate hole diameter and Mach number. Several of these variables can be eliminated as having relatively small effect. Figure 51 shows the empirical curve of the coefficient used in the end correction term as a function of M. Note that at Mach 0.3 δ is nearly zero and can be ignored. The error due to uncertainties in faceplate thickness should likewise be small. The variations of reactance for the 1.8 cm (0.7 inch) and 2.5 cm (1.0 inch) cavity depth liners due to expected variations in M, σ, ℓ, and ω are shown in Figures 52 and 53, respectively. Combining the largest of these variations for the two liners leads to rough "expected error" plots shown in Figures 54 and 55. Based on these plots, the expected variation in impedance for each impedance component for the suppression sensitivity study is taken to be $\pm 0.2\rho c$.

The variation in predicted suppression for Configuration 7 as a function of the variation in impedance components about the nominal values of

$$\frac{Z_1}{\rho c} = 0.64 - 1.15i$$

$$\frac{Z_2}{\rho c} = 0.75 - 0.55i$$

is presented in Figures 56 — 59 and in Table VII. The figures show the variation as the impedance components are varied independently, holding the other three constant. The table shows the results of varying a number of the components in various combinations, as noted.

The results show the suppression in this case to be particularly sensitive to the resistance of the first liner and the reactances of both liners. The values of predicted suppression obtained vary from a low of 15.7 dB for the case where both resistances are low and both reactances less negative to a high of 35.4 dB for the case where $X_2/\rho c$ is +0.2 from the nominal value and the rest of the components are nominal. Note that certain sets of impedances can be found which give higher suppressions than the "optimum" impedance for this case, which was based on the different modal content of Configuration 4. The most important conclusion from these results is that the measured suppression of 20 dB is within the range of expected error in the impedance components, and this is the most likely cause of disagreement in the predicted and measured values.

For Configuration 8, which is Configuration 7 with the panels reversed in axial position, the impedances used for calculation at 1950 Hz were

$$Z_1/\rho c = 0.75 - 0.55i \qquad Z_2/\rho c = 0.64 - 1.15i$$

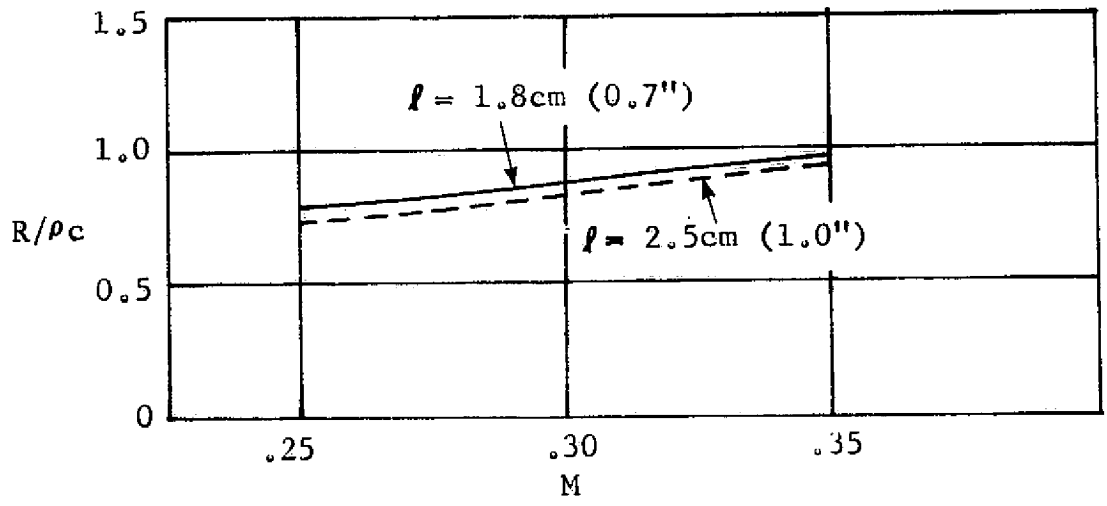

Figure 49. Variation of Resistance Ratio as a Function of Mach Number.

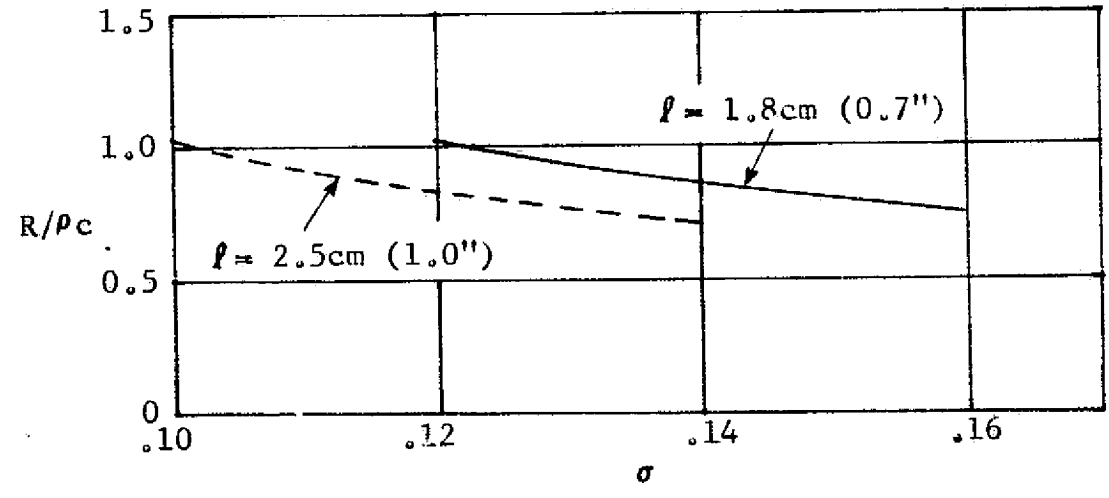

Figure 50. Variation of Resistance Ratio as a Function of Porosity.

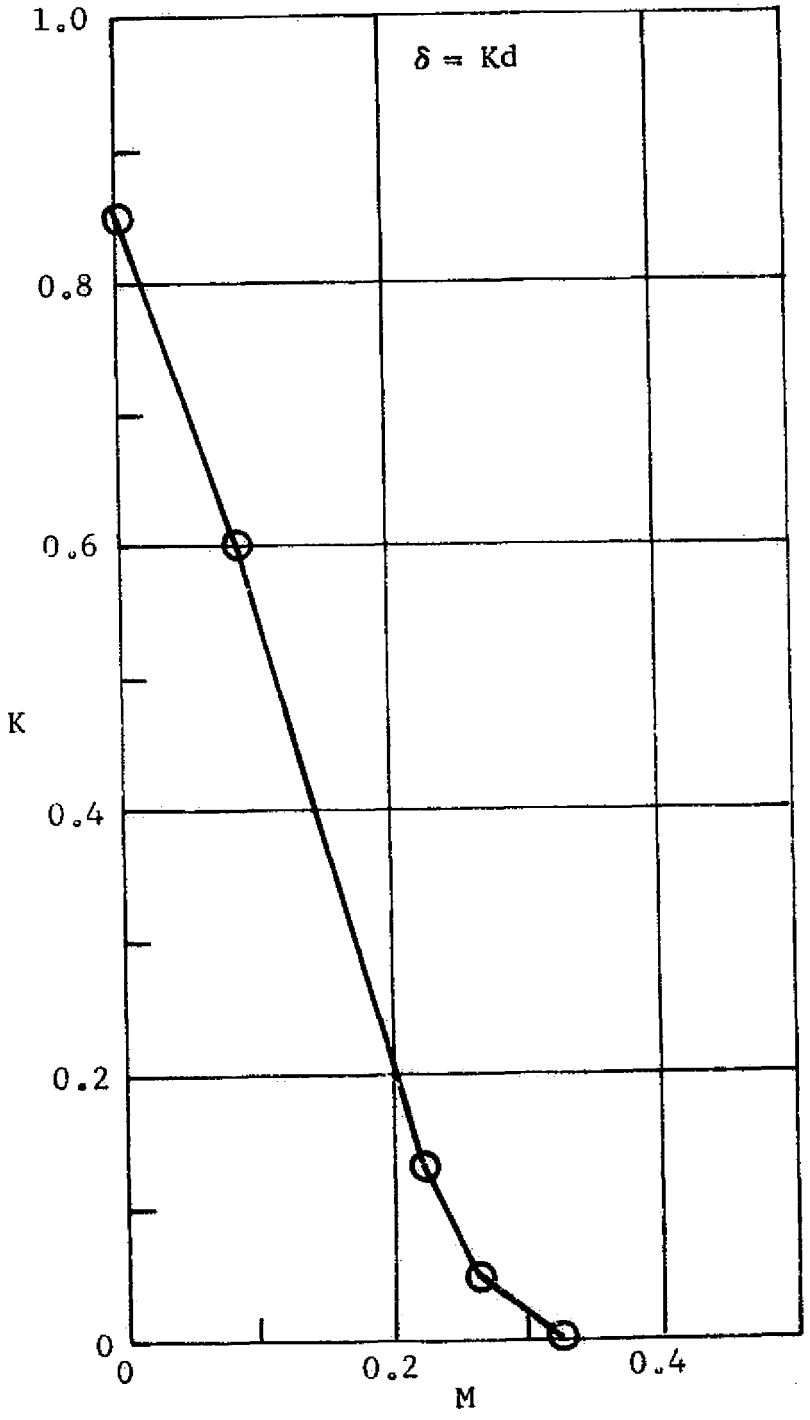

Figure 51. Dependance of End Correction Coefficient K on Mach Number.

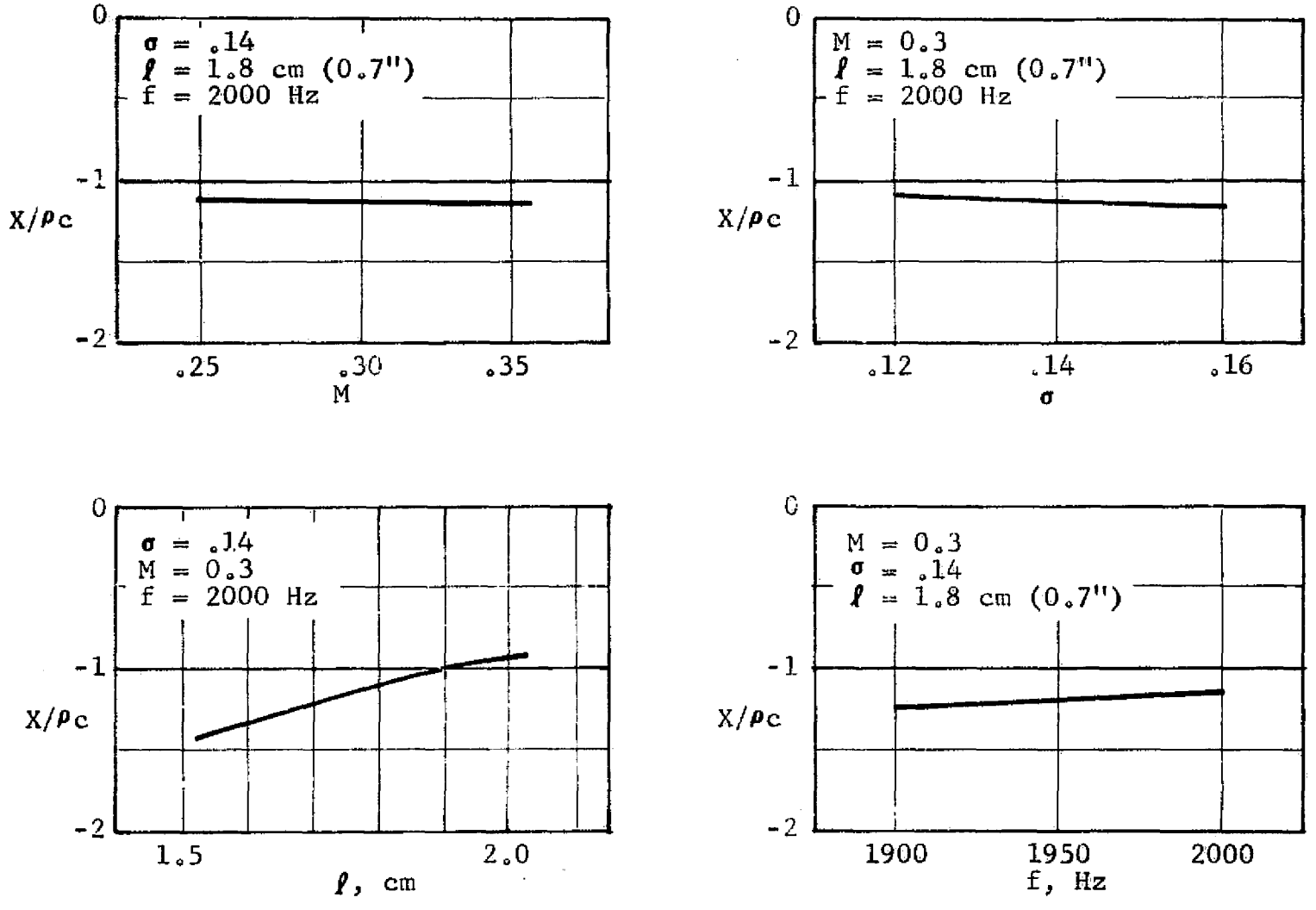

Figure 52. Variation of Reactance Ratio as a Function of Mach Number, Porosity, Cavity Depth, and Frequency for a 1.8 cm (0.7 in.) Nominal Depth Liner.

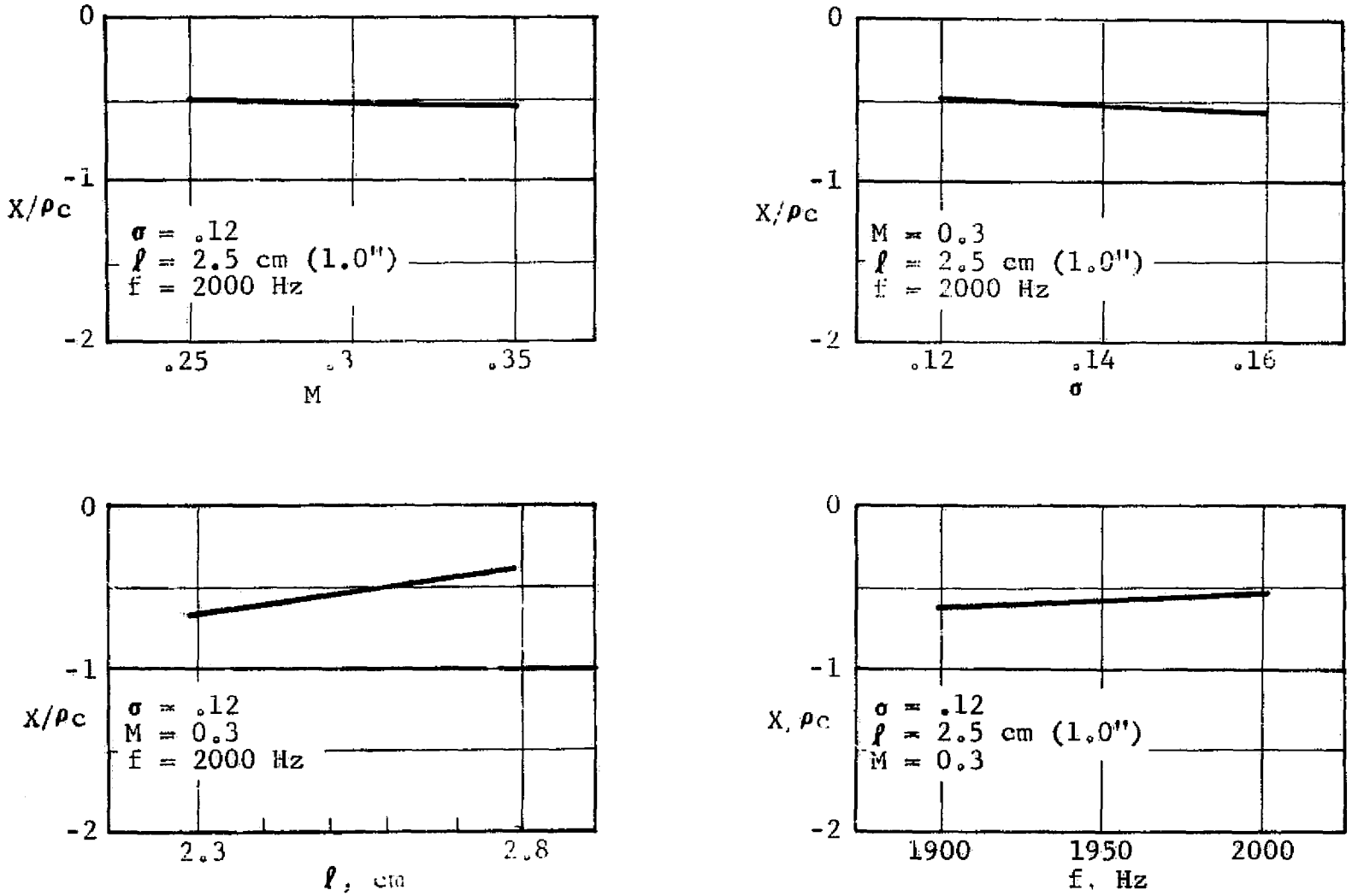

Figure 53. Variation of Reactance Ratio as a Function of Mach Number, Porosity, Cavity Depth, and Frequency for a 2.5 cm (1.0 in.) Nominal Depth Liner.

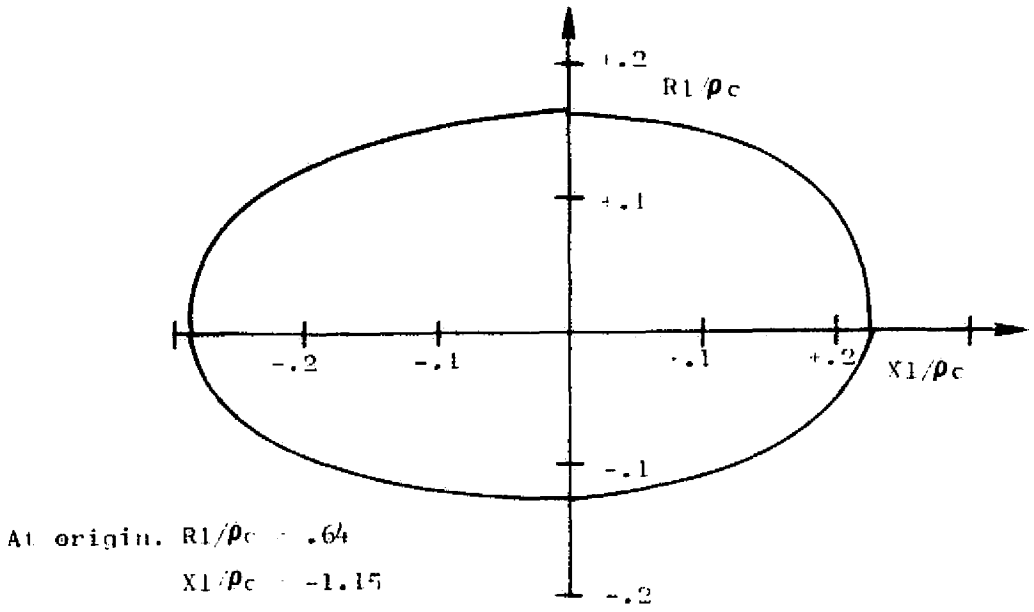

Figure 54. Expected Error in Determination of Impedance Components, 14% Porosity, 1.8 cm (0.7 in.) Deep Liner.

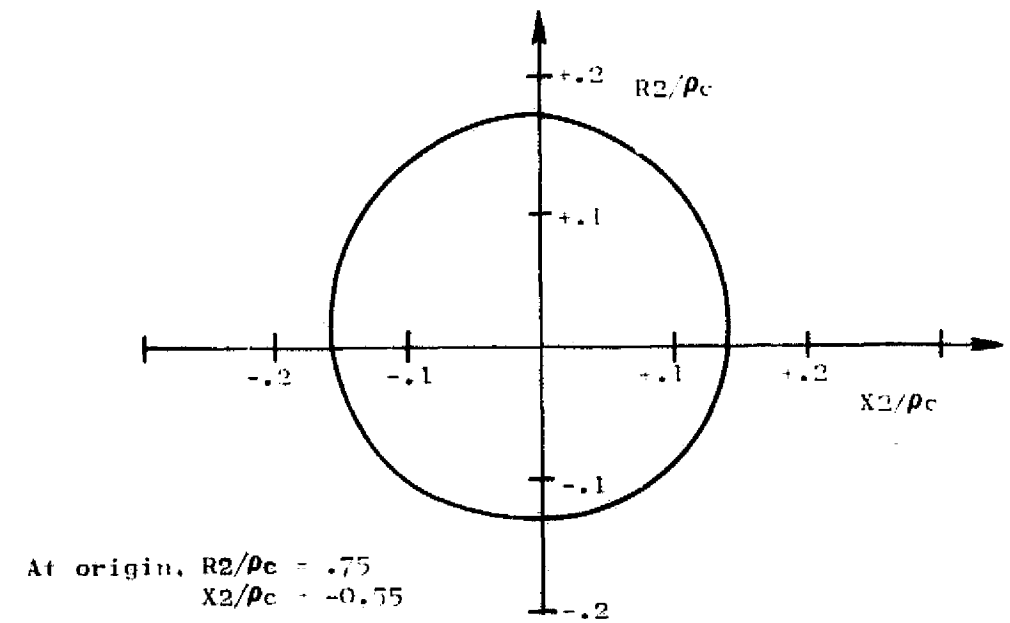

Figure 55. Expected Error in Determination of Impedance Components, 12% Porosity, 2.5 cm (1.0 in.) Deep Liner.

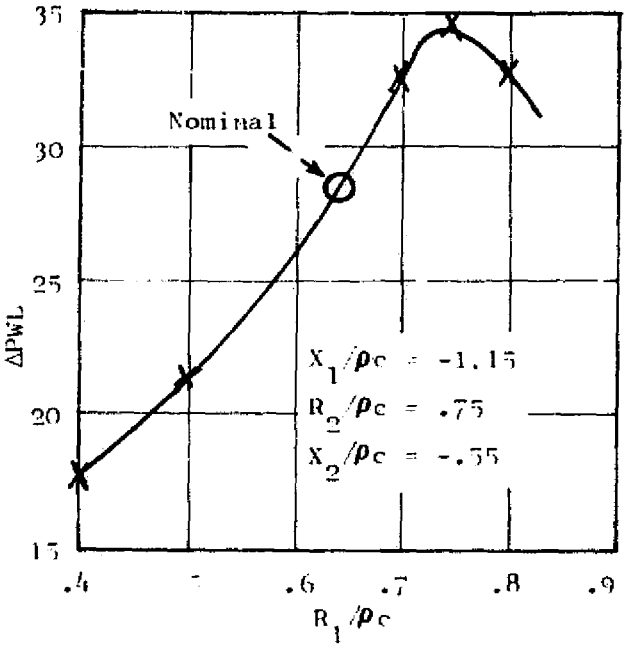

Figure 56. Variation of ΔPWL as a Function of $R_1/\rho c$, Configuration 7, 1950 Hz.

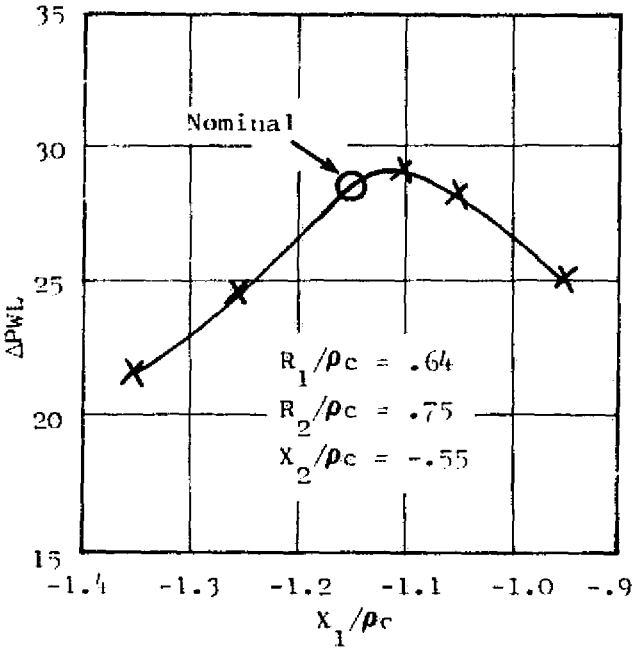

Figure 57. Variation of ΔPWL as a Function of $X_1/\rho c$, Configuration 7, 1950 Hz.

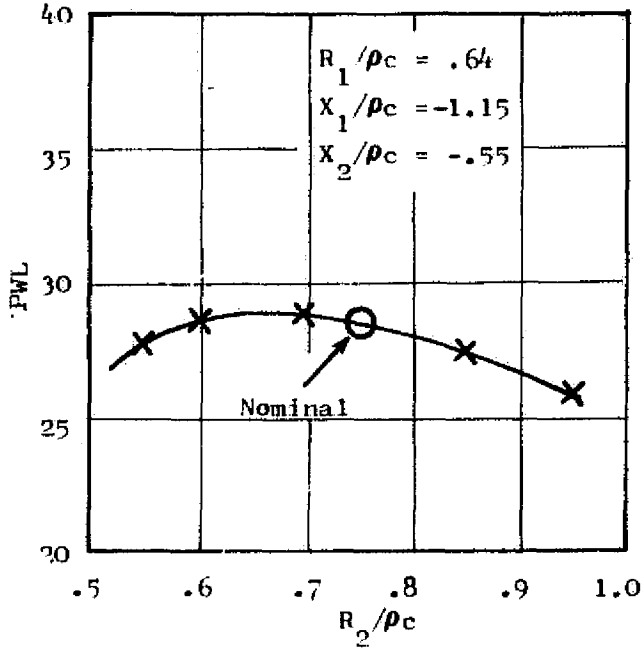

Figure 58. Variation of ΔPWL as a Function of $R_2/\rho c$, Configuration 7, 1950 Hz.

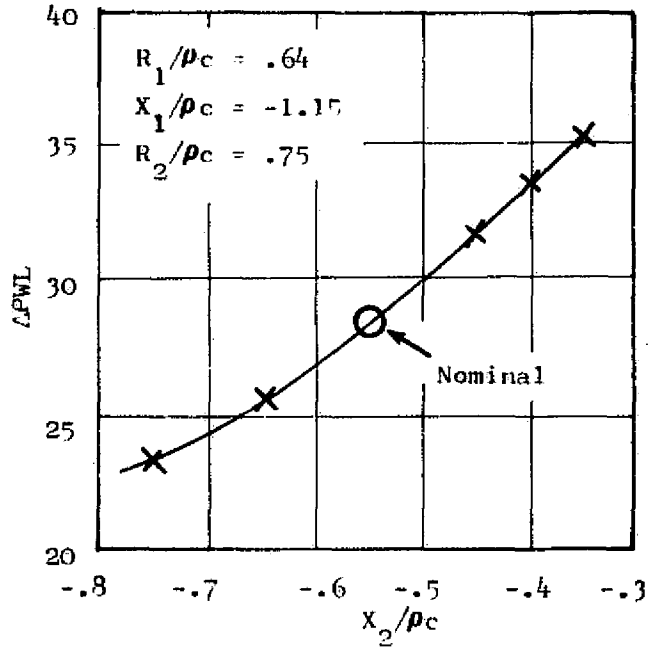

Figure 59. Variation of ΔPWL as a Function of $X_2/\rho c$, Configuration 7, 1950 Hz.

Table VII. Variation of Predicted ΔPWL for Configuration 7 with Combinations of Impedance Components.

DESCRIPTION OF VARIATION	IMPEDANCE OF FIRST SECTION $Z_1/\rho c$	IMPEDANCE OF SECOND SECTION $Z_2/\rho c$	PREDICTED ΔPWL dB
Nominal Case	.64 -1.15i	.75 -.55i	-28.3
Both resistances low	.40 -1.15	.55 -.55	-17.9
Both resistances high	.80 -1.15	.95 -.55	-26.2
Less negative reactances	.64 -0.95	.75 -.35	-25.4
More negative reactances	.64 -1.35	.75 -.75	-19.7
Both resistances low, both reactances less negative	.40 -0.95	.55 -.35	-17.0
Both resistances high, both reactances more negative	.80 -1.35	.95 -.75	-19.5
Both resistances low, both reactances more negative	.40 -1.35	.55 -.75	-15.7
Both resistances high, both reactances less negative	.80 -0.95	.95 -.35	-25.2

Using the measured modes from Figure 42 gave a predicted suppression of 17.7 dB, compared with a measured value (with the nominal impedances listed in Table VI) of 11.0 dB. Using a slightly higher restance of $0.4M/\sigma$ for comparison gives a predicted suppression of 15.4 dB in this case, overpredicting by 4.4 dB. Thus, reversing the order of the liners caused a substantial reduction in suppression.

The suppression for Configuration 9, with higher porosity liners, was measured at 1940 Hz. For the prediction in this case, the impedance components were taken to be

$$Z_1/\rho c = 0.43 - 1.3i$$

$$Z_2/\rho c = 0.64 - 0.6i$$

Using the modes from Figure 44, the suppression is predicted to be 17.6 dB, which compares favorably with the measured value of 16.5 dB.

For Configuration 10, the porosities of the liners were decreased. In this case, to better define the variation in suppression around 2000 Hz, a series of narrowband ΔPWL measurements were made every 20 Hz from 1880 Hz to 2100 Hz, using pure tone excitation and 20 Hz bandwidth data reduction. The results of these measurements are shown in Figure 60. The 26.2 dB suppression measured at 1900 Hz is the highest measured so far, and was chosen for modal measurement, as shown in Figure 46. In addition, a repeat of the narrowband ΔPWL measurement gave a value of 26.1 dB suppression.

The nominal value of the impedance in this case is

$$Z_1/\rho c = 0.75 - 1.2i$$

$$Z_2/\rho c = 0.9 - 0.55i$$

This results in a predicted attenuation of 33.5 dB, overpredicting the measured value of 26.2 dB by 7.3 dB. It is suspected that the same problems with errors in impedance occur here as for Configuration 7.

Third-octave transmission loss measurements were also made for Configuration 10. The results are shown in Figure 61, compared to the empirical duct test prediction for single-element liners. This configuration shows a slight improvement in third-octave suppression over Configuration 4 (Figure 32) at 2000 Hz. The enhancement over the single-element liner prediction, however, occurs mainly for frequencies below 2000 Hz. This is most likely to be caused by the slight increase in cavity depths for Configuration 10 compared to Configuration 4, which would tend to lower the third-octave tuning frequency.

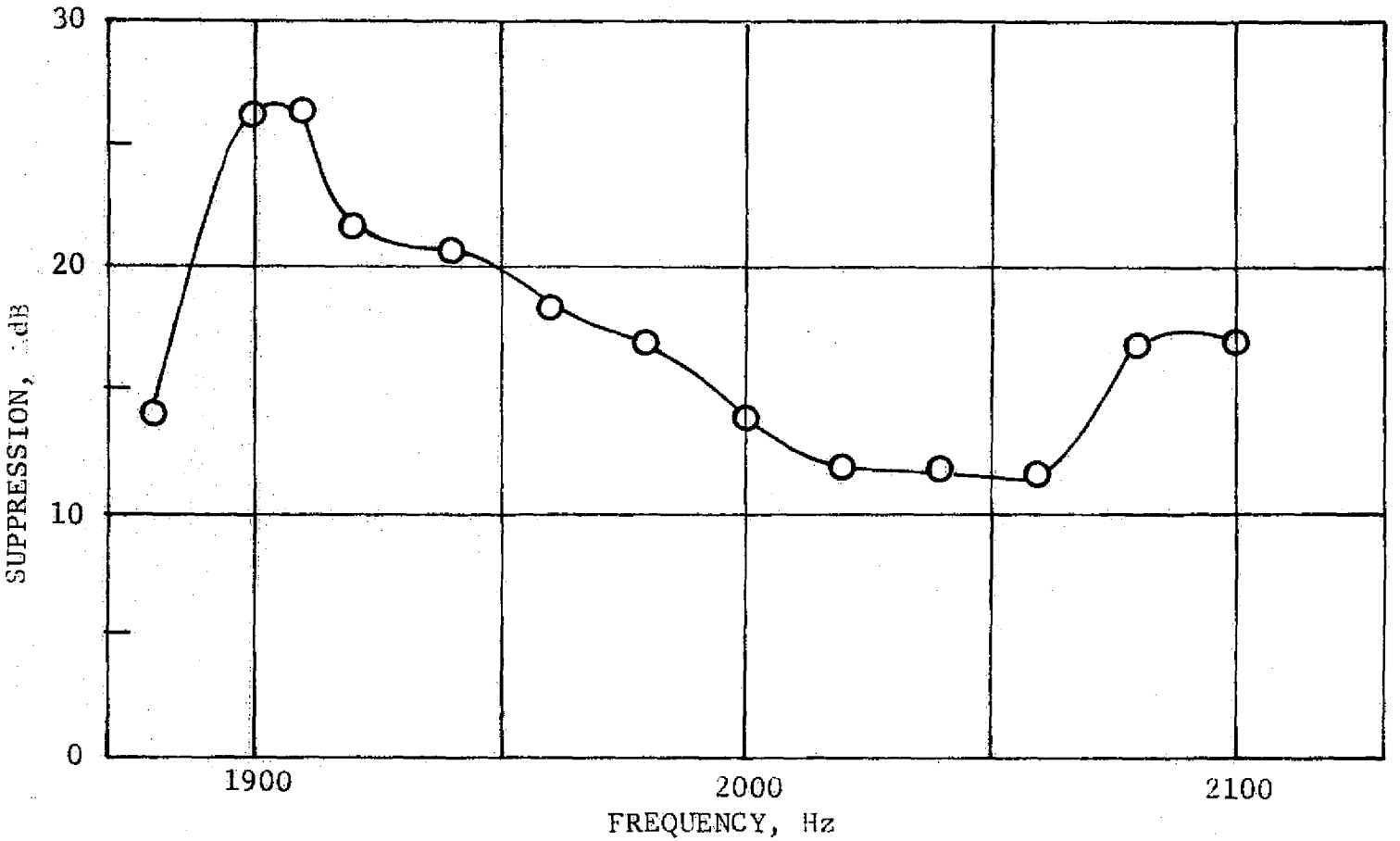

Figure 60. Frequency Dependance of 20 Hz Bandwidth Narrowband Suppression, Configuration 10, Mach 0.3.

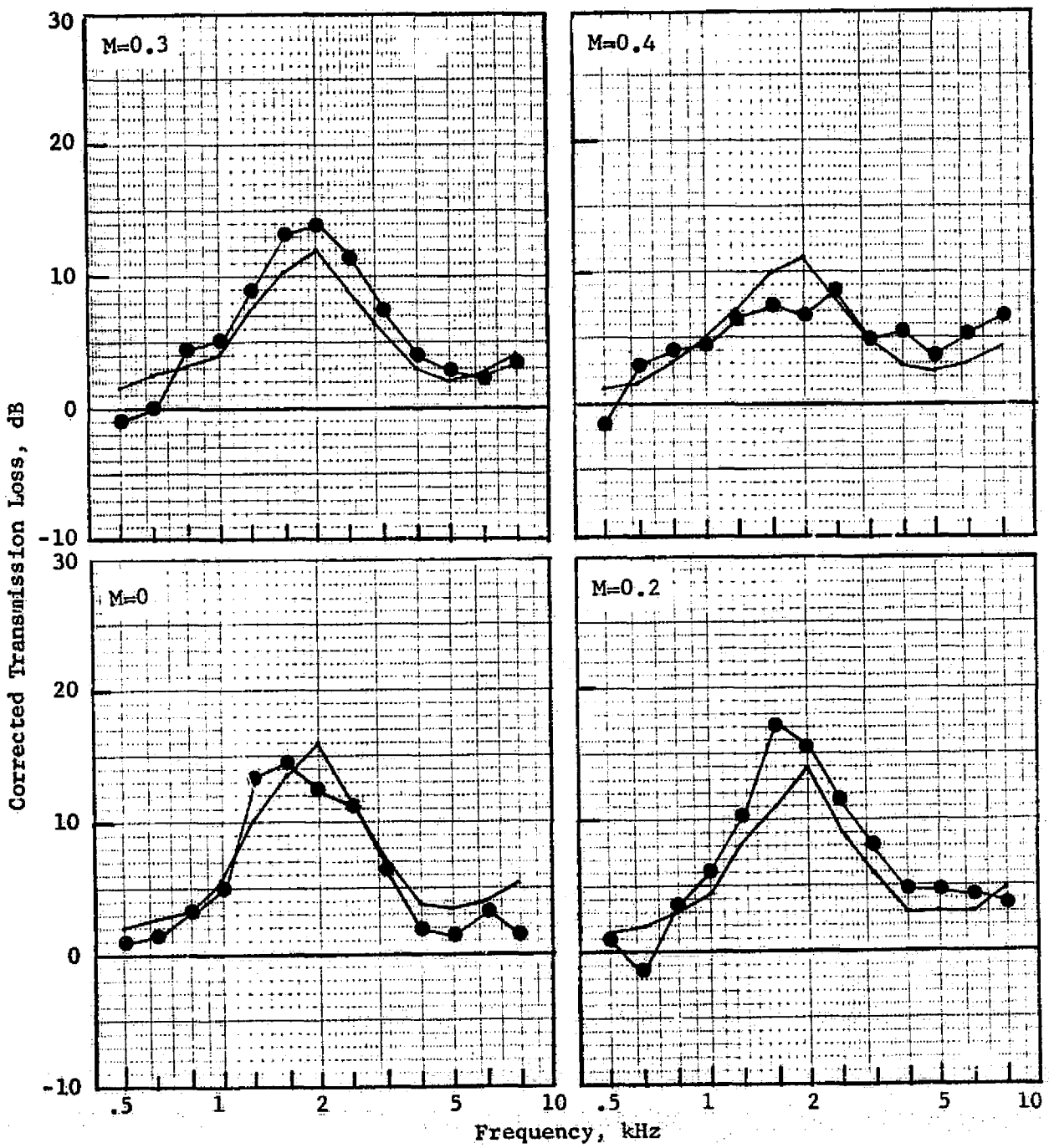

Figure 61. Measured Third-Octave Transmission Loss, Configuration 10, Compared to Empirical Prediction for Rectangular Duct.

4.4.4 Modal Explanation of Difference in Suppression

Further insight to the process of modal attenuation can be gained by examining the details of the modal solutions for the experimental correlation cases, Configurations 4, 7, 8, 9, and 10. Figure 62 shows the plane numbering system used for the analytical model. For convenience, the upstream treatment section will be referred to as the "first section", and the downstream treated section as the "second section".

Figures 63 through 72 present tabulations of the magnitude and phases of the solution modal coefficients for the forward and backward waves at each plane. The order of the coefficients can be identified with the following modes at each plane:

1 - First symmetric
2 - First antisymmetric
3 - Second symmetric
4 - Second antisymmetric
5 - Third symmetric
6 - Third antisymmetric
7 - Forth symmetric

Plotted alongside the modal coefficients at each plane are the (analytical) complex acoustic pressure profiles at each plane.

Table VIII is a list of the attenuations of individual modes in the first and second sections of each configuration. Only the first four modes are included. Table IX is a list of the forward and backward traveling energy at each plane and the suppression of forward traveling energy in the first and second sections for each configuration.

The differences in suppression among each of these configurations can be explained by considering:

a. The relative modal weighting at the source plane,

b. The modal redistributions in the forward traveling wave between Planes 2 and 3 and Planes 5 and 6,

c. The individual modal attenuation rates in Sections 1 and 2,

d. The overall energy attenuations in Sections 1 and 2.

While some of the effects have obvious explanations, others are the result of a very subtle combination of modal redistribution and attenuation properties.

At the source of Configuration 4, most of the energy is in modes 1, 2, and 4, with 1 dominating. Passing into the first section, at plane 3, the energy is redistributed predominatly into mode 3. Mode 3 is still dominant at the end of the first section, and remains so at the end of the second section at plane 6.

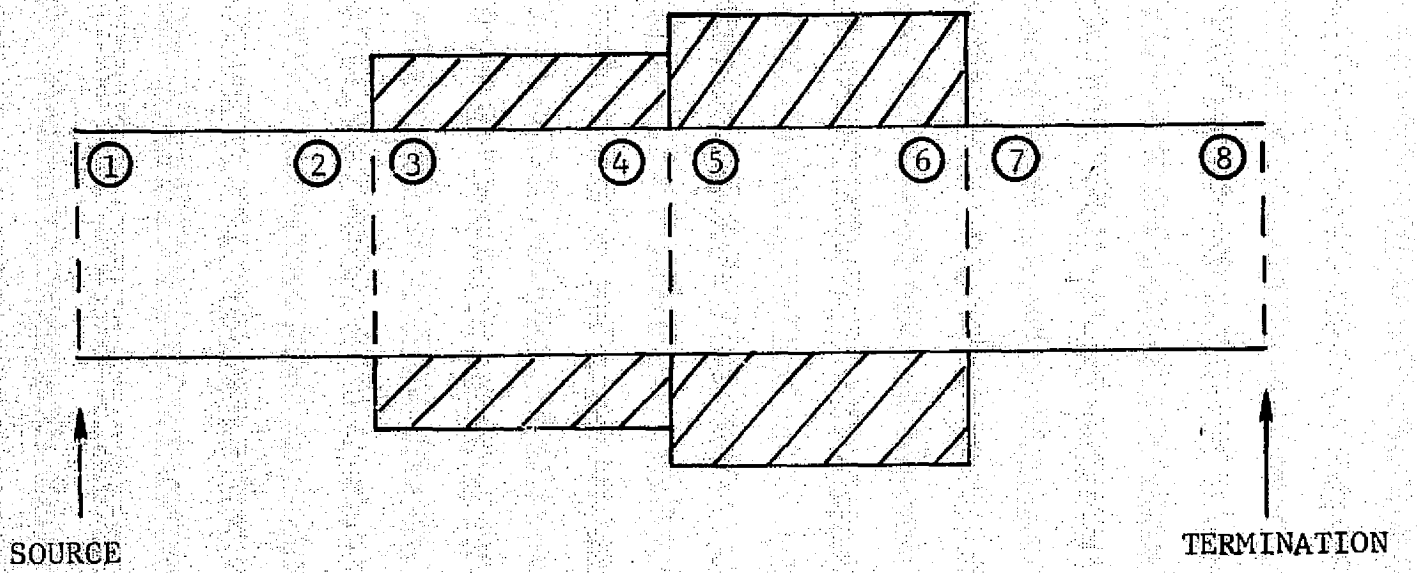

Figure 62. Analytical Model Plane Number Designations.

PLANE	FORWARD WAVE		BACKWARD WAVE	
	MAGNITUDE	PHASE	MAGNITUDE	PHASE
1	1.3109A6E 00	-8.1622A7E 01	2.A549015-02	1.2182A0E 02
	8.3370A0E-01	1.4838A6E 02	3.4460546-02	-7.0214A7E 01
	1.3961736-01	5.4037A7E 01	1.1339A6E-01	1.1200A5E 02
	9.3005496-01	-5.5558116 01	3.8A9A4AE-01	-1.0020A1E 02
	2.0664226-01	-8.2771A1E 01	1.3405416-02	-1.4A1A36E 02
	4.9004806-02	9.2337316 01	2.2954246-03	7.0734426 01
	4.9206206-02	1.3211706 02	3.6033326-04	-1.5734956 02
2	1.3109A8E 00	3.9834A4E 01	2.A549016-02	-1.0373596 02
	8.3370A0E-01	-9.8742546 01	3.4460566-02	7.2804146 01
	1.3961736-01	1.3792116 02	1.1339686-01	-7.5488076 01
	9.3005506-01	-4.4761056 01	3.A49644E-01	1.3A852A6 02
	2.2110036-02	-1.3482506 02	1.2900876-01	1.5480326 02
	1.3395606-03	4.0284066 01	8.4047176-02	1.A6812A6 01
	4.1950636-04	8.0063826 01	9.2265466-02	1.5054736 02
3	8.4713166-01	6.5444A36 01	1.6860066-01	-1.4563576 02
	5.1424066-01	-9.5242276 01	2.2247A46-07	-6.0785A16 01
	1.1349396 00	3.5534206 01	5.7459056-13	0.
	2.7083826-01	-3.9204A76 01	3.5247736-02	-6.2840236 01
	1.2867416-01	1.8516A26 01	2.0A0701E-06	-9.9044556 01
	6.1188816-02	-9.6565A76 01	3.1463756-11	-1.1015256 02
	2.3763416-02	-1.6258A86 02	1.0262466-14	0.
4	2.1801586-01	-6.2636136 01	2.1932506-01	1.0709236 01
	1.8231336-01	-6.4203676 01	7.8194666-02	-6.4444806 01
	5.3502666-01	7.5228466 01	2.3693366-07	1.6018046 02
	6.7743636-02	-1.3390126 02	1.0489256-01	-5.A11797E 01
	6.7578966-06	1.1737426 02	8.9530876-02	9.6139406 01
	1.2783406-10	7.6374246 01	2.9400406-02	1.4359036 02
	3.1480616-10	1.2369016 02	2.8791106-02	3.9064896 01
5	1.9650576-01	-1.6586026 02	2.0819356-02	-1.2700886 00
	1.3702156-01	-1.3657246 02	8.6032626-03	7.7886966 01
	6.2266026-01	7.6090606 01	1.3636646-10	-1.5338856 02
	2.2979416-01	1.1180306 02	2.7353116-08	-7.0710236 01
	7.2398006-02	1.2052316 02	4.4747156-05	-1.2745056 02
	2.4532816-02	1.4053386 02	1.5322816-12	1.6357166 02
	1.4970166-02	1.2819426 02	0.	0.
6	5.1273236-02	1.2127206 02	2.5823516-02	1.0374556 02
	1.0826696-02	-1.0845336 02	2.9766616-02	6.6278736 01
	9.3981856-02	7.6797606 01	8.9809086-03	1.5705366 02
	2.1514066-02	1.3229726 02	6.6433676-02	-1.6396696 02
	8.6740246-00	-3.0429226 01	9.0963066-02	-1.5120516 02
	3.4519486-10	-1.3243106 02	1.8180296-02	-5.6844436 01
	2.8019406-11	1.7253986 02	9.1098546-03	8.3065466 01
7	1.2197656-01	9.4299216 01	0.	0.
	3.8220926-02	-3.2278926 01	0.	0.
	9.0268566-02	-1.7746926 02	0.	0.
	2.5057096-02	-4.5863166 01	0.	0.
	2.3473496-02	1.1408976 02	0.	0.
	4.3193716-03	-1.3405306 02	0.	0.
	8.4534576-03	1.3598156 02	0.	0.
8	1.2197656-01	-2.2745786 01	0.	0.
	3.8220926-02	-1.0654006 02	0.	0.
	9.0268566-02	-9.6929456 00	0.	0.
	2.5057096-02	-2.4304326 01	0.	0.
	2.6973146-04	1.4983246 01	0.	0.
	3.2218116-06	1.2174406 02	0.	0.
	6.1402876-07	3.1675106 01	0.	0.

Figure 63. Modal Participation in First Seven Modes at Each Plane, Configuration 4.

C-2

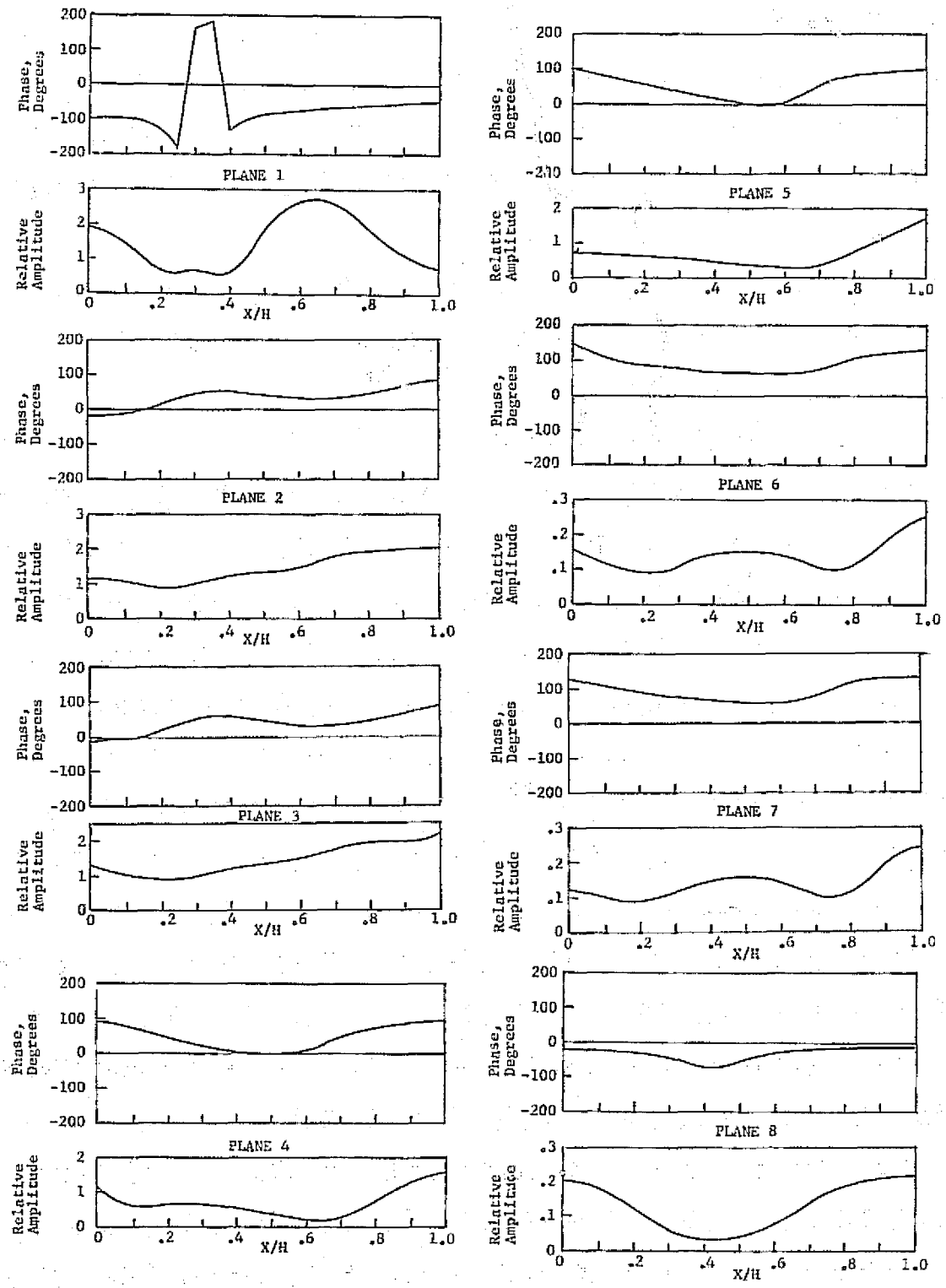

Figure 64. Complex Pressure Profiles at Each Plane, Configuration 4.

PLANE	FORWARD WAVE		BACKWARD WAVE	
	MAGNITUDE	PHASE	MAGNITUDE	PHASE
1	55.941577E-02	33.775287E+00	21.072766E-03	-97.943680E+00
	48.387880E-02	-80.327441E+00	18.245924E-03	-42.029193E+00
	17.298555E-02	16.933965E+01	57.244806E-03	-11.714665E+01
	45.568630E-02	-12.372494E+01	10.851150E-02	-14.890393E+01
	37.363083E-03	-15.865421E+01	65.524407E-04	-28.93623BE+00
	12.708112E-02	65.895600E+00	86.745042E-06	-28.705824E+00
	74.464757E-04	-14.782726E+00	19.007685E-05	-37.131572E+00
2	55.941577E-02	15.201417E+01	23.072766E-03	42.469830E+00
	48.387880E-02	29.076904E+00	18.245924E-03	10.721885E+01
	17.298555E-02	-11.131273E+01	57.244806E-03	42.158122E+00
	45.568630E-02	-12.548362E+01	10.851150E-02	91.707138E+00
	35.998307E-04	15.867198E+01	68.008583E-03	-79.610044E+00
	32.490590E-04	15.221794E+00	33.928767E-04	-79.379631E+00
	60.384538E-06	-65.456532E+00	23.439819E-03	-87.805378E+00
3	23.194307E-02	15.707198E+01	26.707533E-04	47.691493E+00
	25.058215E-02	14.175474E+00	42.068200E-12	-43.475217E-01
	43.130071E-02	14.575188E+01	70.871498E-12	37.584533E+00
	31.827497E-02	-13.285388E+01	39.972262E-04	74.274590E+00
	55.115082E-03	13.654666E+01	12.197006E-07	-37.207382E+00
	19.273784E-03	-10.631602E+01	11.274257E-12	-12.760535E+01
	12.993444E-03	-37.078509E+00	.0	.0
4	12.125139E-02	24.432884E+00	32.263466E-04	-12.150346E+01
	72.441643E-03	53.794076E+00	16.041748E-03	63.963264E+00
	15.655702E-02	-16.694293E+01	27.722901E-03	98.495808E+00
	81.721633E-03	12.565618E+01	11.611036E-03	15.918266E+01
	29.220347E-07	-12.853569E+01	29.615720E-03	15.805830E+01
	85.081106E-12	-64.691064E+00	77.059703E-04	94.443258E+00
	34.167466E-15	.0	12.906066E-03	15.272409E+01
5	58.051046E-03	-33.667579E+00	20.169572E-05	-86.191340E+00
	54.494710E-03	12.980690E+01	12.963623E-04	-96.886969E+00
	19.251763E-02	72.296590E-01	40.794682E-13	-10.717749E+01
	62.504040E-03	-12.718245E+01	15.156659E-10	14.216416E+01
	34.220822E-03	-13.326830E+01	23.301674E-07	-33.405123E-01
	64.986262E-04	-51.356217E+00	28.125440E-15	.0
	68.207176E-04	-12.334147E+01	.0	.0
6	23.419381E-03	-11.164222E+01	24.208306E-05	95.027307E+00
	37.982250E-04	18.967488E+01	37.366891E-04	-71.085894E+00
	81.667745E-04	12.176613E+01	19.632916E-04	-35.688043E+00
	26.192616E-04	-11.267638E+01	43.534622E-04	-16.003996E+01
	40.559612E-07	90.242448E+00	23.017259E-04	37.134342E+00
	61.220645E-12	54.814262E+00	25.014081E-04	-24.109614E+00
	37.219958E-15	.0	11.637685E-04	-87.379626E+00
7	22.753287E-03	-11.022738E+01	.0	.0
	55.502412E-04	33.651284E+00	.0	.0
	18.832394E-03	14.743232E+00	.0	.0
	12.312752E-03	98.190315E+00	.0	.0
	16.751708E-04	-42.008331E+00	.0	.0
	12.760282E-04	10.515744E+01	.0	.0
	63.047754E-05	-32.388652E+00	.0	.0
8	22.753287E-03	12.625033E+01	.0	.0
	55.502412E-04	-10.754003E+01	.0	.0
	18.832394E-03	-16.656154E+01	.0	.0
	12.312752E-03	94.262959E+00	.0	.0
	15.550341E-06	-14.335594E+01	.0	.0
	83.409097E-08	38.098240E-01	.0	.0
	41.459070E-09	-13.373626E+01	.0	.0

Figure 65. Modal Participation in First Seven Modes at Each Plane, Configuration 7.

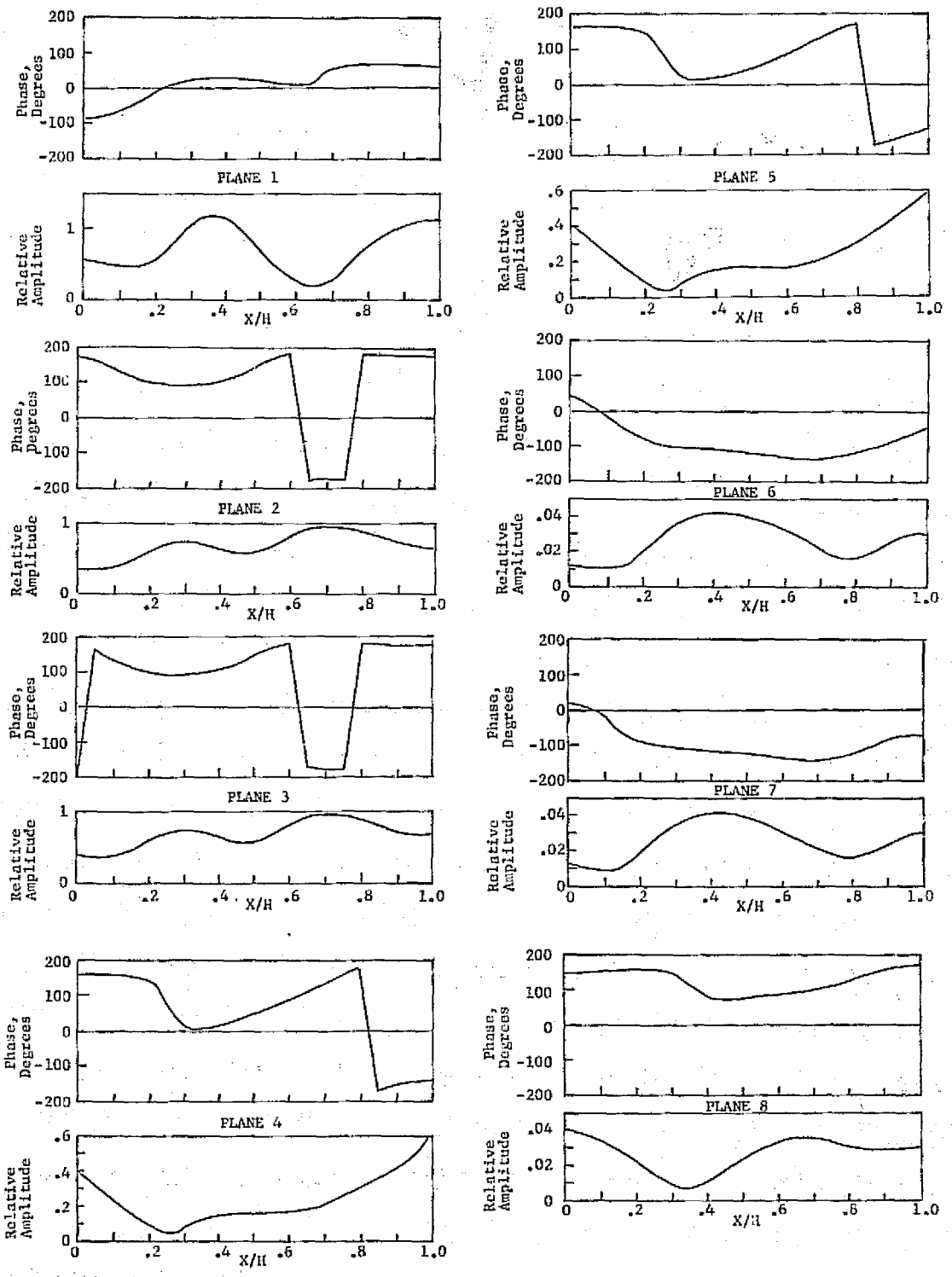

Figure 66. Complex Pressure Profiles at Each Plane, Configuration 7.

PLANE	FORWARD WAVE		BACKWARD WAVE	
	MAGNITUDE	PHASE	MAGNITUDE	PHASE
1	48.500412E-02	50.270057E+00	25.112014E-03	-72.119846E+00
	37.401973E-02	-85.768132E+00	14.976612E-03	15.086236E+00
	14.983324E-02	11.742015E+01	80.677107E-03	-10.959028E+01
	26.974247E-02	-11.523504E+01	76.476314E-03	-13.281566E+01
	11.021797E-03	11.513831E+00	88.887202E-04	-32.798406E-01
	11.496521E-02	64.772351E+00	10.257373E-05	15.263294E+01
	38.610491E-03	-91.335671E+00	25.357403E-05	-14.459322E+00
2	48.500412E-02	16.850894E+01	25.112014E-03	68.293465E+00
	37.401973E-02	23.636212E+00	14.976612E-03	16.433428E+01
	14.983324E-02	-16.323224E+01	80.677107E-03	69.714494E+00
	26.974247E-02	-11.719372E+01	76.476314E-03	12.777751E+01
	10.619199E-04	-39.159975E+00	92.257114E-03	-53.953646E+00
	29.392940E-04	14.098545E+00	40.119875E-04	10.195914E+01
	31.309800E-05	-14.200948E+01	31.270138E-03	-61.133128E+00
3	38.615938E-02	-16.394378E+01	24.351936E-04	-11.149824E+01
	25.371551E-02	-12.586371E+01	14.609993E-05	37.889587E+00
	38.167347E-02	-47.939552E+00	28.113030E-12	-16.536506E+01
	22.989972E-02	17.123965E+01	59.721504E-11	-92.350140E+00
	10.845193E-02	16.787227E+01	17.482287E-06	-64.338005E+00
	22.923871E-03	10.926851E+01	.0	.0
	19.854684E-03	16.251496E+01	.0	.0
4	15.578726E-02	11.808158E+01	29.228142E-04	69.720410E+00
	17.683709E-03	-14.599573E+01	42.112456E-05	63.699661E+00
	16.195938E-03	-53.95155CE+00	13.529723E-03	-93.875614E+00
	96.340576E-04	-17.425429E+01	17.153867E-04	-34.554261E+00
	12.854069E-06	31.393015E+00	17.268902E-03	-23.863151E+00
	21.592727E-11	-14.456100E+01	98.511664E-05	97.477020E+00
	10.832939E-14	.0	78.802324E-04	-14.390284E+01
5	14.260060E-02	10.396375E+01	16.023004E-04	10.296759E+01
	99.254976E-04	34.360486E+00	67.681089E-13	12.650685E+01
	91.339106E-03	14.195274E+01	43.566771E-12	98.173741E+00
	18.401889E-03	-15.449669E+01	70.408909E-05	-15.822748E+01
	14.207737E-03	57.703266E+00	72.525203E-08	23.224593E+00
	35.722092E-05	51.075529E+00	18.768535E-13	-12.116231E+00
	30.029311E-04	-10.109127E+01	.0	.0
6	74.546397E-03	-28.675340E+00	19.356248E-04	-66.227367E+00
	28.693958E-04	73.979089E+00	25.808639E-04	-17.387741E+01
	33.155008E-03	-17.074207E+01	17.042073E-03	15.708302E+01
	47.249471E-04	10.801337E+01	20.452193E-04	-73.319405E+00
	75.325115E-08	15.262092E+01	17.609946E-03	-14.150973E+01
	15.769099E-13	90.500526E+00	12.828319E-04	-15.006763E+01
	.0	.0	77.540749E-04	-14.622067E+01
7	45.419743E-04	-54.000148E+00	.0	.0
	42.199772E-04	45.596361E+00	.0	.0
	12.558163E-02	15.754969E+01	.0	.0
	11.425136E-03	10.151127E+01	.0	.0
	17.371591E-03	12.858192E+01	.0	.0
	10.094246E-04	10.020558E+01	.0	.0
	66.682466E-04	14.447975E+01	.0	.0
8	45.419743E-04	-17.752219E+01	.0	.0
	42.199772E-04	-95.594952E+00	.0	.0
	12.558163E-02	-43.755077E+00	.0	.0
	11.425136E-03	97.593915E+00	.0	.0
	16.125691E-05	27.234310E+00	.0	.0
	65.902234E-08	-11.420346E-01	.0	.0
	43.849192E-08	43.13213ME+00	.0	.0

Figure 67. Modal Participation in First Seven Modes at Each Plane, Configuration 8.

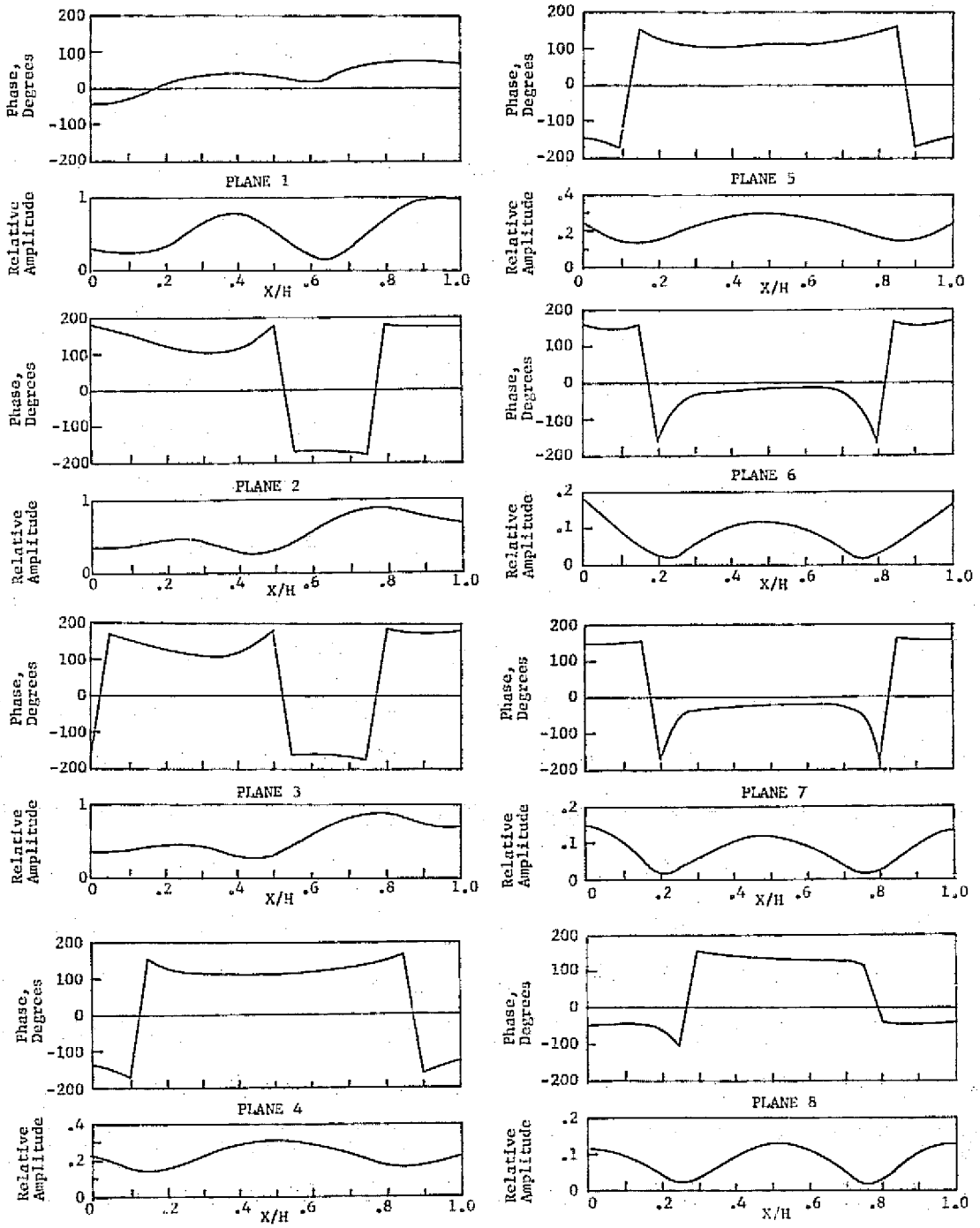

Figure 68. Complex Pressure Profiles at Each Plane, Configuration 8.

PLANE	FORWARD WAVE		BACKWARD WAVE	
	MAGNITUDE	PHASE	MAGNITUDE	PHASE
1	1.117727E-01	-2.842227E 01	2.320167E-02	1.285984E 02
	1.120500E-01	-1.339191E 02	1.830891E-01	-7.658992E 01
	2.915476E-02	1.209634E 02	2.307637E-02	-1.344131E 02
	2.055651E-01	1.186479E 02	1.468030E-01	-4.414772E 01
	8.280097E-03	3.714007E 01	9.287029E-04	-1.054291E 02
	1.495660E-02	4.986534E 00	4.784127E-04	-1.348497E 02
	2.319483E-03	-9.743141E 01	3.019234E-05	-1.215296E 02
2	1.117727E-01	8.939151E 01	2.320167E-02	-9.019866E 01
	1.120500E-01	-2.497548E 01	1.830891E-01	7.384124E 01
	2.915476E-02	-1.602944E 02	2.307637E-02	4.586579E 01
	2.055651E-01	1.077721E 02	1.468030E-01	-1.412052E 02
	7.872302E-04	-1.330493E 01	9.768108E-03	-1.559207E 02
	3.791571E-04	-4.550529E 01	1.887193E-02	1.746068E 02
	1.868764E-05	-1.479250E 02	3.747428E-05	-1.720216E 02
3	4.930928E-02	8.758216E 01	3.655971E-01	-6.175166E 01
	4.245780E-02	-2.586776E 01	0.	0.
	8.478483E-02	8.632900E 01	0.	0.
	1.058042E-01	1.285809E 02	1.340333E-01	3.367010E 01
	1.129137E-02	-1.111105E 02	4.475875E-04	3.608147E 01
	6.487171E-03	1.527715E 02	7.946336E-11	8.809683E 01
	2.705731E-03	-1.141708E 02	0.	0.
4	3.328934E-02	-5.260984E 01	4.178371E-01	1.373039E 02
	4.971784E-02	1.907066E 01	8.479265E-07	-1.003496E 02
	4.514957E-02	1.419205E 02	1.910356E-12	-1.205085E 02
	4.552098E-02	1.946375E 01	2.750618E-01	1.415290E 02
	5.179619E-07	-5.781425E 01	1.177623E-01	-6.322178E 01
	5.549144E-11	6.639557E 00	3.866082E-04	-2.040038E 01
	2.182787E-11	0.	5.299033E-05	-1.754630E 02
5	2.751869E-02	-1.007177E 02	1.232591E-02	-1.010426E 02
	3.839662E-02	-1.017673E 01	4.720174E-03	6.511843E 01
	5.502536E-02	-4.852372E 01	2.808819E-13	0.
	2.748691E-02	-1.716376E 02	0.	0.
	9.919216E-03	1.570358E 02	3.205063E-06	1.767492E 02
	8.033215E-03	-1.789545E 02	1.149465E-10	-1.621885E 02
	2.022957E-03	-3.985879E 00	0.	0.
6	1.282951E-02	1.690777E 02	1.446533E-02	8.622563E 01
	4.390848E-03	-3.150976E 01	1.197529E-02	1.059484E 02
	2.664236E-03	-8.149702E 00	4.592278E-04	-2.383419E 01
	1.252165E-03	-1.210349E 02	2.122712E-03	7.641526E 01
	1.677175E-06	-8.150686E 00	3.854048E-03	-8.897393E 01
	8.850281E-11	-8.181431E 01	9.458576E-04	-6.511160E 01
	7.275958E-11	-1.288699E 02	2.019632E-03	1.005394E 02
7	1.370248E-02	-1.750433E 02	0.	0.
	2.397659E-03	1.626672E 02	0.	0.
	1.562676E-02	-4.749972E 01	0.	0.
	9.570784E-03	-5.357626E 01	0.	0.
	2.263527E-03	-1.049148E 02	0.	0.
	4.446374E-04	4.010738E 00	0.	0.
	8.460926E-04	-9.388804E 01	0.	0.
8	1.370248E-02	6.058427E 01	0.	0.
	2.397659E-03	2.055837E 01	0.	0.
	1.562676E-02	1.049801E 02	0.	0.
	9.570784E-03	-5.142787E 01	0.	0.
	2.046060E-05	1.495602E 02	0.	0.
	2.857449E-07	-9.697250E 01	0.	0.
	5.492179E-08	1.651283E 02	0.	0.

Figure 69. Modal Participation in First Seven Modes at Each Plane, Configuration 9.

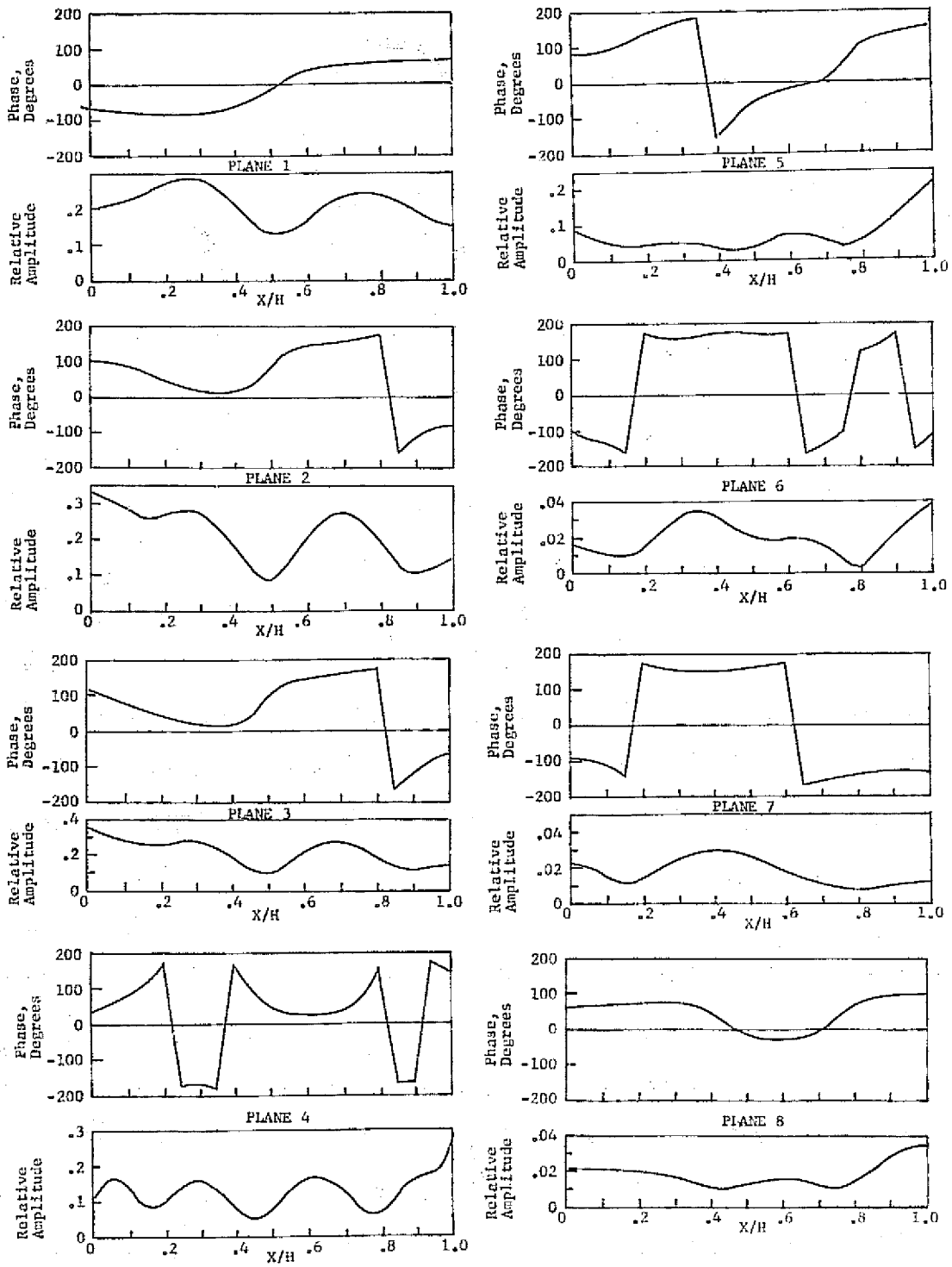

Figure 70. Complex Pressure Profiles at Each Plane, Configuration 9.

PLANE	FORWARD WAVE		BACKWARD WAVE	
	MAGNITUDE	PHASE	MAGNITUDE	PHASE
1	2.460187E 00	-9.241501E 01	5.568585E-02	1.637306E 02
	2.339682E 00	7.171101E 01	4.037629E-01	-5.420850E 00
	1.327528E 00	1.422738E 02	1.524753E-01	1.555360E 00
	2.927076E 00	-1.282710E 02	1.972718E 00	1.136818E 02
	7.300728E-01	4.920463E 01	8.050440E-03	1.585294E 02
	2.550728E-01	1.009839E 02	5.317366E-03	-2.949597E 01
	8.030435E-02	8.940352E 01	2.965041E-04	1.576010E 02
2	2.460187E 00	2.296882E 01	5.568585E-02	-5.055519E 01
	2.339682E 00	1.780304E 02	4.037629E-01	1.493590E 02
	1.327528E 00	-1.420983E 02	1.524753E-01	-1.729737E 02
	2.927076E 00	-1.459054E 02	1.972718E 00	3.241490E 01
	6.448157E-02	-2.459316E-01	9.114864E-02	1.090789E 02
	6.165606E-03	5.193319E 01	2.199817E-01	-7.890653E 01
	6.238798E-04	3.995296E 01	3.816531E-02	1.081504E 02
3	1.756770E 00	4.450668E 01	1.032089E 00	4.874894E 01
	1.644428E 00	1.776518E 02	1.222491E-08	1.660502E 02
	1.946693E 00	6.321428E 00	1.265051E-12	-2.897560E 00
	2.571236E-01	-1.451251E 02	1.993428E-01	1.485057E 02
	8.488087E-02	-8.541905E 01	1.920186E-06	-1.098765E 02
	1.589440E-01	1.672994E 02	1.895126E-11	-5.746945E 01
	2.847602E-02	1.495851E 02	1.322520E-14	0.
4	8.250871E-01	-1.167918E 02	1.311840E 00	-8.586274E 01
	4.290034E-01	-1.742857E 02	1.670468E-01	-7.190253E 01
	7.659869E-01	2.526611E 01	1.092287E-06	-1.064417E 02
	5.115857E-02	6.735745E 01	8.178519E-01	-7.417493E 01
	1.573152E-06	1.278221E 01	1.693638E-01	8.926494E 01
	6.525836E-10	7.056712E 01	3.415014E-02	-1.762086E 02
	8.597107E-10	8.197276E 01	5.342273E-02	9.371051E 00
5	3.539309E-01	1.331314E 02	1.063064E-02	3.109833E 01
	1.316454E-01	1.288843E 02	4.739509E-03	-8.600842E 01
	9.775333E-01	-1.516403E 02	4.405662E-06	9.018823E 01
	4.875903E-01	8.911875E 00	1.705167E-08	1.100899E 02
	1.600658E-01	8.451835E 01	2.509133E-11	3.652618E 01
	5.113155E-02	9.418946E 01	3.559496E-14	0.
	3.605603E-02	9.300138E 01	0.	0.
6	9.679411E-02	5.673053E 01	1.843936E-02	-1.148532E 02
	4.830850E-03	4.916766E 01	1.908468E-02	-2.447327E 01
	1.879812E-02	1.193575E 02	9.437726E-03	8.723833E 01
	3.256805E-02	-2.509310E 01	1.886403E-02	1.242555E 02
	4.602258E-06	-5.687558E 01	3.136295E-03	1.358566E 02
	2.301432E-10	-1.391077E 02	1.850947E-03	2.692314E 01
	8.540732E-11	-5.124951E 01	3.906620E-03	-1.241526E 02
7	2.884681E-02	9.098699E 01	0.	0.
	5.116847E-02	1.611572E 02	0.	0.
	8.132762E-02	-7.759724E 01	0.	0.
	3.658192E-02	-1.598060E 02	0.	0.
	1.370042E-02	-8.917188E 01	0.	0.
	5.540417E-03	-1.798186E 02	0.	0.
	4.950718E-03	-8.965341E 01	0.	0.
8	2.884682E-02	-7.824376E 01	0.	0.
	5.116847E-02	1.379519E 01	0.	0.
	8.132762E-02	1.285853E 01	0.	0.
	3.658192E-02	1.649245E 02	0.	0.
	1.068742E-04	-1.680730E 02	0.	0.
	3.237172E-06	8.128031E 01	0.	0.
	2.988078E-07	-1.485545E 02	0.	0.

Figure 71. Modal Participation in First Seven Modes at Each Plane, Configuration 10.

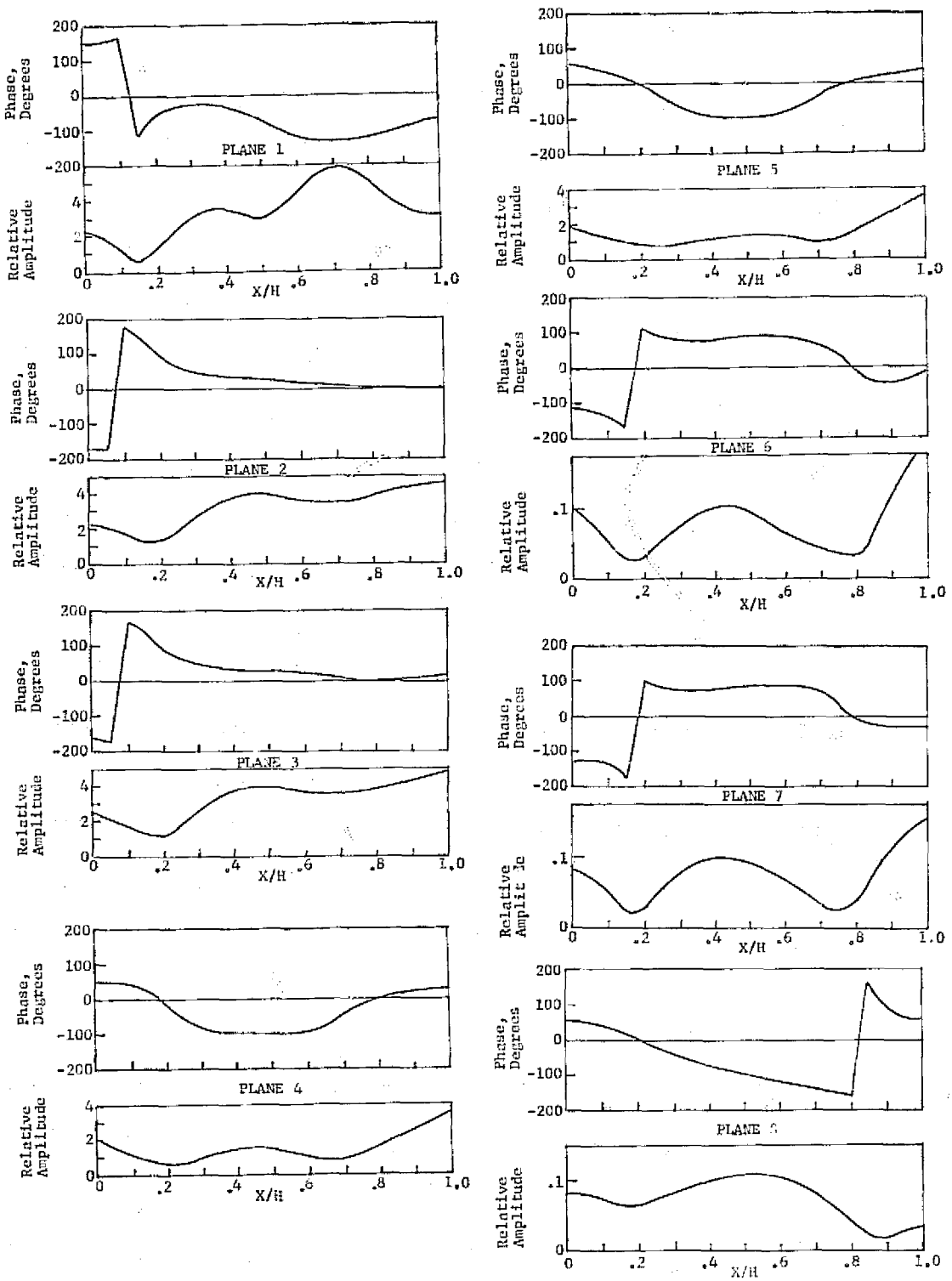

Figure 72. Complex Pressure Profiles at Each Plane, Configuration 10.

Table VIII. Attentuation of Individual Forward-Propagating Modes in Treated Sections.

CONFIGURATION 4

Mode	Section 1 (ΔdB)	Section 2
1	6.2	11.7
2	9.0	22.1
3	10.1	16.4
4	12.0	20.6

Overall Suppression, 20.6 dB

CONFIGURATION 7

Mode	Section 1 (ΔdB)	Section 2
1	5.6	7.9
2	10.8	23.1
3	8.8	27.4
4	11.8	27.5

Overall Suppression, 28.3 dB

CONFIGURATION 8

Mode	Section 1 (ΔdB)	Section 2
1	7.9	5.6
2	23.1	10.8
3	27.4	8.8
4	27.5	11.8

Overall Suppression, 17.7 dB

CONFIGURATION 9

Mode	Section 1 (ΔdB)	Section 2
1	3.4	6.6
2	6.7	18.8
3	5.5	26.3
4	7.3	26.8

Overall Suppression, 17.6 dB

CONFIGURATION 10

Mode	Section 1 (ΔdB)	Section 2
1	6.6	11.3
2	10.5	28.7
3	8.1	21.9
4	14.0	23.5

Overall Suppression, 33.5 dB

Table IX. Forward- and Backward-Travelling Energy at Duct Planes.

CONFIGURATION 4

Plane Number	Forward Energy Flux	Backward Energy Flux
1	0.5978	-3.618E-3
2	0.5978	-3.618E-3
3	0.5928	-4.529E-5
4	0.1483	-5.361E-5
5	0.1522	-5.508E-6
6	5.136E-3	-3.504E-6
7	5.112E-3	0.0
8	5.112E-3	0.0

FORWARD ΔPWL

Section 1 -6.0 dB
Section 2 -14.7 dB

CONFIGURATION 9

Plane Number	Forward Energy Flux	Backward Energy Flux
1	6.1216E-3	-1.7302E-3
2	6.1216E-3	-1.7302E-3
3	5.9902E-3	-1,8433E-4
4	1.2684E-3	-3.1554E-4
5	1.2931E-3	-1.5061E-6
6	7.7558E-5	-4.5399E-6
7	7.6962E-5	0.0
8	7.6962E-5	0.0

FORWARD ΔPWL

Section 1 -6.8
Section 2 -12.2

CONFIGURATION 7

Plane Number	Forward Energy Flux	Backward Energy Flux
1	12.496E-2	-36.79E-5
2	12.496E-2	-36.79E-5
3	12.4614E-2	-10.806E-7
4	17.4547E-3	-49.9589E-6
5	17.4175E-3	-23.1133E-9
6	18.4635E-5	-10.5437E-7
7	18.4154E-5	0.0
8	18.4154E-5	0.0

FORWARD ΔPWL

Section 1 -8.5
Section 2 -19.7

CONFIGURATION 8

Plane Number	Forward Energy Flux	Backward Energy Flux
1	87.3618E-3	-38.4946E-5
2	87.3618E-3	-38.4946E-5
3	87.0438E-3	-54.4828E-8
4	12.5082E-3	-89.6023E-7
5	12.4874E-3	-24.7554E-8
6	14.8182E-4	-11.1900E-6
7	14.1931E-4	0.0
8	14.1931E-4	0.0

FORWARD ΔPWL

Section 1 -8.4
Section 2 -9.4

CONFIGURATION 10

Plane Number	Forward Energy Flux	Backward Energy Flux
1	2.6626	-5.3427E-2
2	2.6626	-5.3427E-2
3	2.6057	-1.3690E-3
4	5.8379E-1	-1.9853E-3
5	0.5900	-2.0164E-6
6	1.1755E-3	-3.6073E-5
7	1.1560E-3	0.0
8	1.1560E-3	0.0

FORWARD ΔPWL

Section 1 -6.6
Section 2 -27.0

At the source of Configuration 7, modes 1, 2, and 4 dominate evenly. The energy redistributes into modes 3 and 4 at Plane 3, with 3 dominating. At the end of the first section, modes 1 and 3 dominate evenly. The energy is dominated by mode 3 at Plane 5, but mode 1 dominates by the end of the second section.

Configuration 8 starts with modes 1 and 2 about even at the source. The energy redistributes into the first four modes at Plane 3, with 1 and 3 dominating. At Plane 4, only mode 1 retains significant energy. The energy redistributes into modes 1 and 3 entering the second section, and is left in modes 1 and 3 at Plane 6, with mode 1 dominating.

For Configuration 9, the energy starts out in modes 1, 2, and 4, with 4 dominant. It redistributes into modes 3 and 4 at Plane 3. By Plane 4, the energy is in modes 1, 3, and 4. It then redistributes into modes 2 and 3 at Plane 5, with 3 dominant. At the end of the second section, mode 1 dominates.

Modes 1, 2, and 4 dominate evenly at the source of Configuration 10. These redistribute into modes 1, 2, and 3 at the entrance to Section 1. At the end of the first section, the energy is in modes 1, 2, and 3, with 1 and 3 dominating evenly. At Plane 5, the energy goes into modes 3 and 4, with most in mode 3. At the end of the second section, modes 1 and 3 dominate.

For all configurations except Configuration 9, the effect of reflected waves on the overall attenuation is small. In Configuration 9, there is appreciable reflected energy at the source plane, accounting for about a 1.5 dB drop in the effective (measured) suppression.

The suppression characteristics in the first section are remarkably similar for all configurations, varying from a low of -6.0 dB to a high of -8.6 dB in ΔPWL. Two points worth noting: Configuration 10, which gives the most overall ΔPWL, provides only -6.6 dB in the first section, and the first section of Configuration 8 (which gave -19.7 dB in its reversed position in Configuration 7) provides only -8.4 dB when it leads.

Comparing the "least effective suppressor", Configuration 8, to the rest, it is apparent that the performance is controlled by the dominant participation of the lowest order mode. The redistribution of modes coming off the hardwall section is not as advantageous to suppression at it was when coming off the "set-up" treatment section in the arrangement of Configuration 7. The second section of Configuration 8 is then ineffective in redistributing and suppressing the pattern coming from the first section.

Differences among Configurations 4, 7, 9, and 10 can be explained by considering individual mode attenuation rates in the second sections. In the second section of Configuration 4, mode 1 has the highest attenuation rate of all sections, but at the expense of mode 3, which dominates. In Configuration 9, mode 3 has a high attenuation rate in the second section, but mode 1 has a low attenuation rate. Thus, even though the third mode dominates at the entrance to Section 2, the suppression is controlled by

mode 1. For Configuration 7, the overall suppression is aided by a high ΔPWL in the first section. In the second section of Configuration 7, the situation is similar to Configuration 9 except that the mode 1 rate is slightly higher. In Configuration 10, the high suppression in the second section appears to be caused by obtaining just the right tradeoff in attenuation rates of the first and third modes. At the end of the second section, in this case, modes 1 and 3 are left with approximately equal amplitude, which approaches the optimum situation.

From the above, it appears that the action of the first treated segment is to "set-up" a particular pressure profile which the second section can effectively "wipe-out" at about 4 times the suppression rate of the first segment. A possible indication of this trends is apparent from the amplitude plots of the pressure profiles at Plane 5. For the two high suppression configurations, 7 and 10, there is a pronounced skew in level toward the outer wall of the duct. The skew toward the outer wall is less pronounced but nevertheless present in Configurations 4 and 9. In the worst performer, Configuration 8, the outer wall skew is very slight, such that most of the energy in concentrated at the center of the duct. This suggests a physical explanation of the operation of a two-element suppressor is that the first section distributes the energy flux to the outer walls of the duct, and the second section takes advantage of this situation, as discussed in Reference 8.

4.4.5 Evaluation of Test Results and Correlation

Table X summarizes the test configurations for which modal measurements were taken and compares the measured and predicted results using nominal impedance values. The correlation is good for Configurations 4 and 9, but over-predicts for Configurations 7, 8, and 10.

The inability to come within 10 dB of the predicted optimum attenuation is disappointing, and can be traced to two main problems. First, the modal content in the source signal appears to be dependent upon the treatment present and is quite sensitive to slight changes in frequency. Second, the predicted attenuation is very sensitive to changes in impedance, particularly near the optimum condition.

The dependence of the source modal content on the treated section could possibly be explained by changes in modal pattern at the source plane due to modes reflected from the leading edge of the treatment interacting with forward-traveling modes. The analytical results, however, indicate that the backward-traveling energy (PWL) at the source plane, at these frequencies, is typically 25 dB or more below the forward-traveling energy (PWL), indicating that their effects should be negligible. It is possible that the acoustic "loading" presented by the duct upon the source may cause the radiation efficiency of different modes to vary from configuration to configuration.

The sensitivity of the suppression to the changes in modal content which were experienced for the different configurations was investigated by calculating the suppression for a number of different measured sources holding the

Table X. Summary of Measured and Predicted Suppressions.

Config.	Liner Characteristics		Impedances $\bar{Z}/\rho c$	Measured ΔPWL, dB	Predicted ΔPWL, dB
4	Section 1	10% Porosity, 1.3cm deep	.90 -1.4i	-19,-21.5	-20.6
	Section 2	10% Porosity, 2.3cm deep	.90 -1.7i		
7	Section 1	14% Porosity, 1.8cm deep	.64 -1.15i	-20.0	-28.3
	Section 2	12% Porosity, 2.5cm deep	.75 -0.55i		
8	Section 1	12% Porosity, 2.5cm deep	.75 -0.55i	-11.0	-17.7
	Section 2	14% Porosity, 1.8cm deep	.64 -1.15i		
9	Section 1	20% Porosity, 1.8cm deep	.43 -1.3i	-16.5	-17.6
	Section 2	14% Porosity, 2.5cm deep	.64 -0.6i		
10	Section 1	12% Porosity, 1.8cm deep	.75 -1.2i	-26.1,-26.2	-33.5
	Section 2	10% Porosity, 2.5cm deep	.90 -0.55i		

impedance components of the treatment constant at the theoretical optimum values for the modal content of Configuration 4. Table XI lists the predicted suppressions for these cases, all calculated at 2000 Hz. For these samples, anywhere from 2.6 dB to 12.7 dB would be lost due to changes in modal content alone if Z/ρc were not changed.

The optimum value of suppression occurs at the top of a very sharp peak in the four parameter impedance space of the two liners. This is indicated in Table V which shows that variations in any one of the impedance components values by 0.1 can cause the suppression to fall off anywhere from 1.2 to 8.4 dB from the peak value. Combinations of variations from the optimum impedance components could be expected to give further reductions from the peak value.

Based on the results of the sensitivity studies, it can be concluded that the maximum value of suppression practically obtainable under the given two-element panel design constraints has been closely approached. The "sharpness" of the attenuation peak would seem to indicate that it will be of greater practical value to investigate effects of broadband frequency suppression than to attempt to refine the pure-tone optimum design.

Table XI. Predicted Suppressions for Varying Modal Input, Holding Impedance Constant at Optimum Value, Mach 0.3, 2000 Hz.

MODES OBTAINED FROM CONFIGURATION:		PREDICTED ΔPWL dB
4	(Figure 37)	-35.9
7	(Figure 40)	-27.9
8	(Figure 42)	-23.2
9	(Figure 44)	-28.2
10	(Figure 46)	-23.0

In all cases

$$Z_1/\rho c = .6 - 1.2i$$

$$Z_2/\rho c = .7 - .5i$$

SECTION 5.0

ANALYTICAL PARAMETRIC STUDIES

Results of systematic optimization studies of uniform treatment and of two-segment treatment were previously discussed only for a single value of η and a single L/H value. In the above two-segment liner configuration the segments were of equal length, i.e., $L_1 = L_2$. It was deemed desirable to carry out additional parametric studies. These analytical optimization studies included:

- The effect of η (ratio of duct height-to-wavelength, H/λ) on the optimum sound suppression in an acoustically lined rectangular duct.
- The effect of variation of liner segment length ratio on optimum sound suppression when the total length of the two-element treatment is kept constant.

The following is a discussion of the results of these parametric studies.

5.1 The Effect of η Variation on Optimum Attenuation

The effect of variation of η on the maximum suppression was explored for the following conditions:

- Rectangular duct geometry modeled in two dimensions.
- Duct height-to-wavelength ratios, η, ranging from 0.5 to 10.
- Constant total wall liner length with a corresponding L/H of 3.43.
- In the two-segment liner configuration, a 1:1 ratio of the panel lengths was maintained.
- Exhaust conditions, i.e., flow and sound propagating in the same direction.
- Uniform profile flow of Mach 0.3.
- Continuity of particle displacement wall boundary conditions.
- Plane wave source modal input.
- Three modes used in calculation.

The iterative optimization procedure was described in Section 3.2.

Table XII summarizes the results of the optimization of uniform treatment and of two-segment treatment for a range of η values from 0.5 to 10. In that range of η, optimum sound suppression was predicted for negative reactance values. In all cases, the criteria for judging the validity of the computer runs was the balance of energy flux at section interfaces.

Figure 73 graphically depicts the peak suppression and associated optimum resistance and reactance ratios as a function of η for the case of single-element treatment. The negative optimum reactance ratio decreases monotonically with increasing η, i.e., with increasing frequency. It decreases from about -0.1, at η of 0.5, to -3.6 at an η of 10. The corresponding resistance ratio increases moderately with η. Optimum suppression of the uniform liner decreases markedly with increasing η.

Optimum suppression predicted for the two-segment treatment and the associated liner segment impedance components are shown in Figure 74 as a function of η. The optimum resistance of the upstream liner segment is relatively small. Its value ranges from about 0.6 ρc shown to 0.005 ρc for high values of η. The optimum resistance of the downstream (second) liner increases with η, i.e., it increases with frequency. The negative reactance of both liner segments increase in absolute value with η. The absolute value of the reactance of the first segment increases at a faster rate than that of the second segment. For η larger than 1, the negative reactance of the first liner segment is larger, in absolute value, than that of the second liner segment. This suggests a smaller cavity depth for the first than that of the second optimized liner segment.

The two-phase treatment optimum suppression also decreases with increase in η. Its decrease, however, is not as monotonic as that of the uniform treatment. The two-phase treatment suppression and the uniform treatment suppression are compared graphically in Figure 75. For all considered η values the two-phase treatment suppression exceeds that of the single-phase liner. The largest beneficial phasing effect of about 10 dB is shown for an η of about 1.5, and about 1.0 dB for η values lower than 1.0.

At the η values of 0.5 and 1.0 there is little difference in impedance components between the optimized single-element and two-element configurations. The optimization becomes extremely difficult in this η region due to the high sensitivity of calculated suppression to small changes (on the order of 0.01 ρc in the impedance. From practical considerations, it appears doubtful that liners could be manufactured to the tolerances required to take advantage of the multiphasing effect for these low η values. Cases at these low η values were particularly prone to energy flux unbalances, requiring many runs to be discarded. The cause of these mismatches requires further investigation.

Lester and Posey[12] have determined an optimized suppression curve for a two-element, equal-length liner configuration in a cylindrical geometry duct. These curves exhibit a "knee" phenomenon in the two-element liner configuration similar to that of Figure 75, such that the major multiphase enhancement occurs in the midrange of η values.

Table XII. Summary of Optimization Results for Several η Values.

$L_1 = L_2 = 45.72$cm (18 Inches)

$M = 0.3$

$L = L_1 + L_2$

$L/H = 3.43$

Plane Wave Source

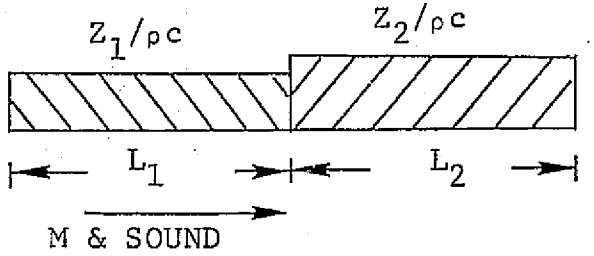

		Uniform Liner		Two-Segment Liner		
f, Hz	η	$Z_1/\rho c = Z_2/\rho c$*	$-\Delta$dB**	$Z_1/\rho c$	$Z_2/\rho c$	$-\Delta$dB
650	0.5	0.31 -0.1i	70.6	.32 -0.09i	0.3 -0.10i	71.4
1303	1.0	0.65 -0.5i	39.2	.60 -0.47i	0.72-0.50i	41.4
2000	1.535	0.85 -1.0i	22.6	.67 -1.37i	0.60-0.62i	34.3
2606	2.0	0.90 -1.4i	14.3	.50 -1.60i	1.20-0.90i	22.9
6514	5.0	0.85 -2.45i	4.0	.005-2.90i	1.00-1.75i	6.1
13029	10.0	1.40 -3.6i	2.3	.05 -4.40i	2.00-3.00i	2.8

* $Z_1/\rho c$ = impedance ratio of upstream segment
$Z_2/\rho c$ = impedance ratio of downstream segment

** $-\Delta$dB = suppression in dB's

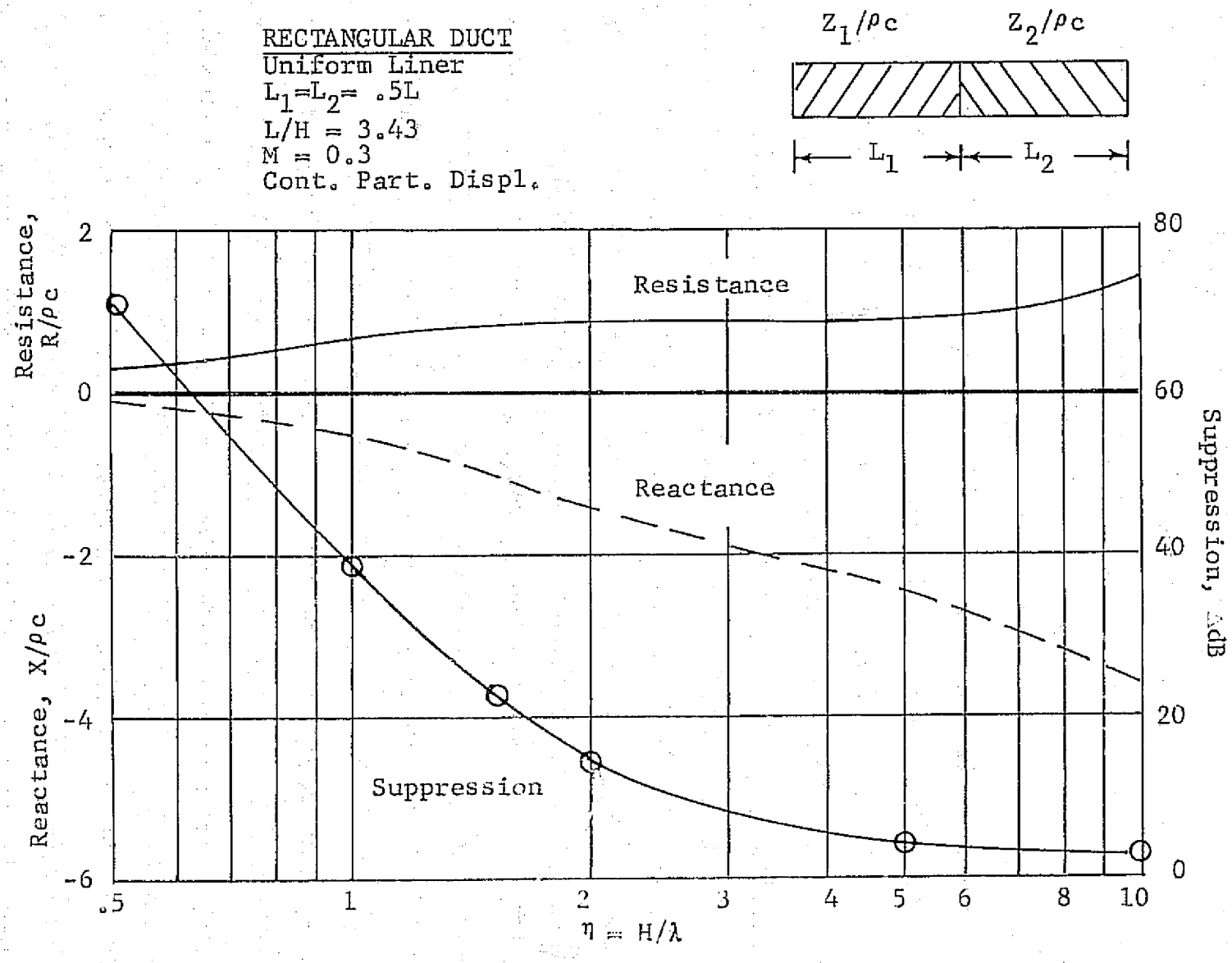

Figure 73. Optimum Impedance Components and Associated Suppression as a Function of η in a Uniformly Lined Rectangular Duct, Mach 0.3.

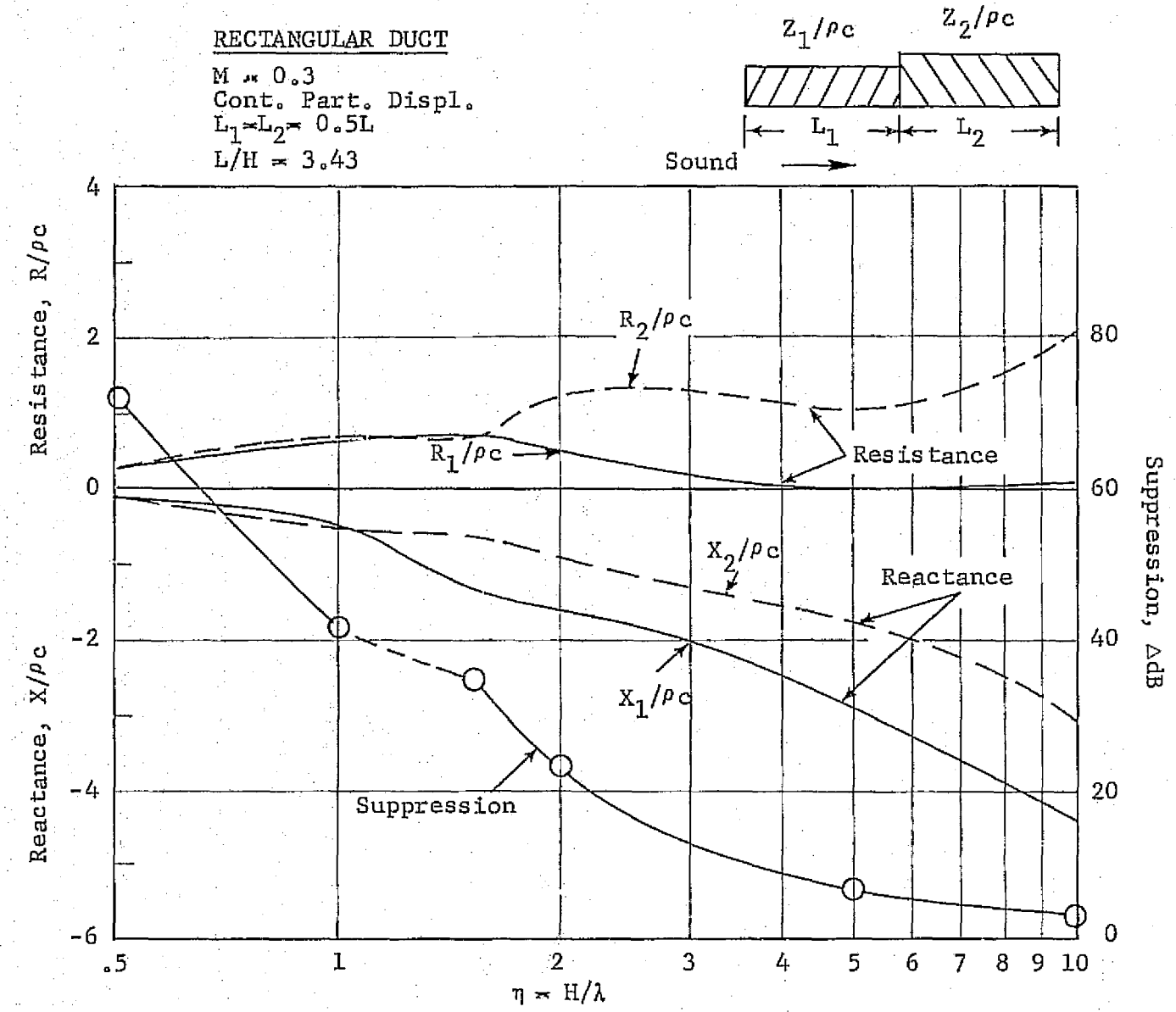

Figure 74. Optimum Impedance Components and Associated Suppression as a Function of η (H/λ) in an Acoustically Treated Rectangular Duct, Mach 0.3.

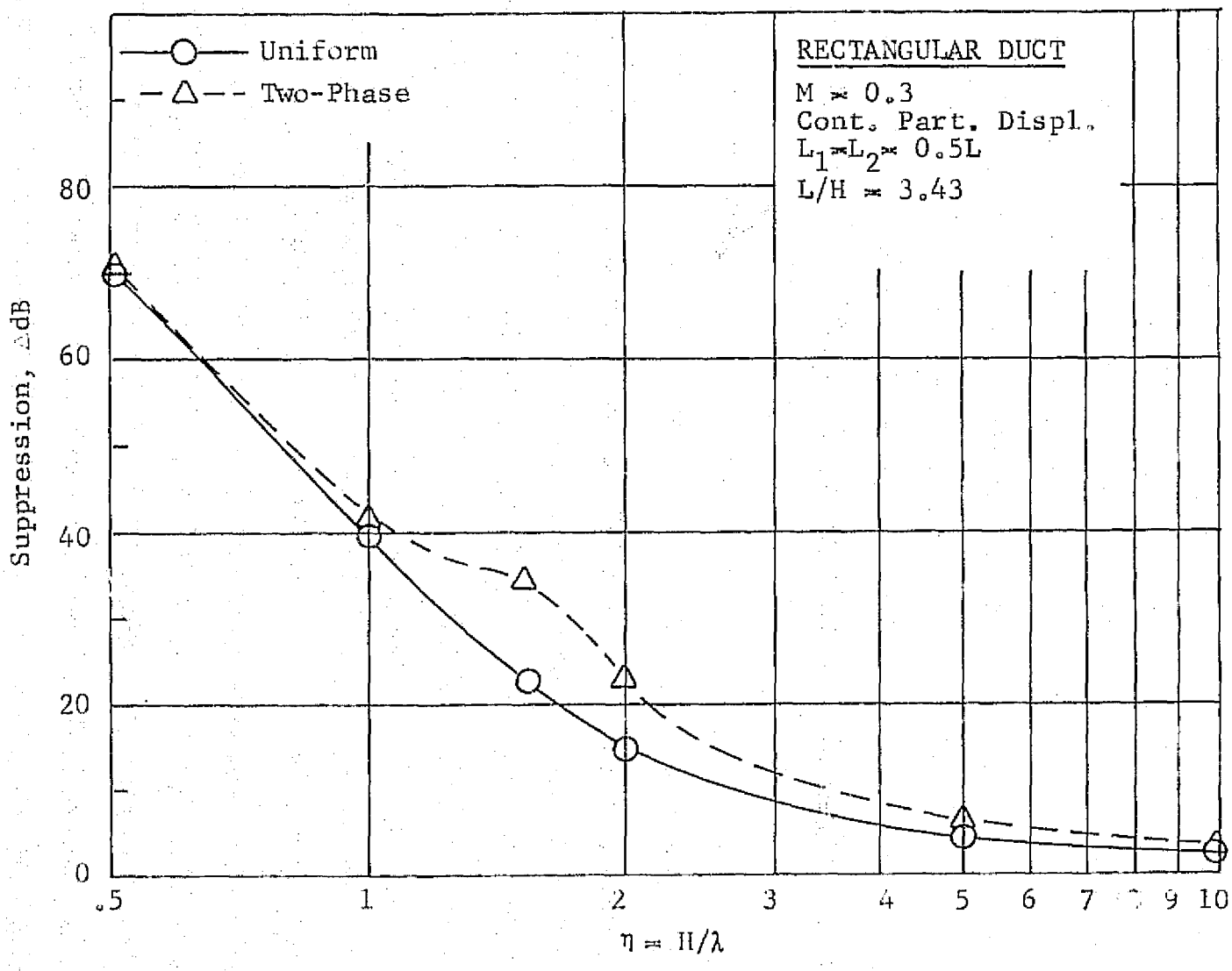

Figure 75. Maximum Predicted Sound Power Suppression in a Rectangular Duct with Uniform and Two-Phase Treatment, Mach 0.3.

5.2 EFFECT OF SEGMENT LENGTH RATIO VARIATION

The conditions in this part of the parametric optimization investigation were the same as those in the study of the η effect, except as noted below:

- Duct height-to-wavelength ratio, η was 1.535.
- The ratio of the upstream liner segment length (L_1) to that of the downstream segment (L_2) was varied over a range of values from 1:7 to 2:1, holding the overall length, $L_1 + L_2$, constant. The duct geometry is depicted schematically in Figure 76.
- The source modal distribution was based on measured modal information from Configuration 4 at Mach 0.3. The modal expansion coefficients used here (amplitude and phase) are shown in Figure 77.
- The five lowest transverse modes were used.

The effect of variation of the ratio of the lengths of the two liner segments, with the total liner length kept unchanged, is summarized in Table XIII and shown graphically in Figures 78 and 79. In addition to the optimized total suppression, Table XIII and Figure 73 show the associated suppressions due to each of the two liner segments. The respective optimized resistance and reactance ratios (impedance components) are also included in Table XIII and are depicted graphically in Figure 79. Figures 78 and 79 show the respective calculated point values with the smooth curves drawn through them. The uniform (single-phase) liner information included in Table XIII and Figures 78 and 79 were taken from Table II. They were obtained for a slightly different source modal input and seven transverse modes.

Table XIII and Figure 78 show an increase in total suppression with increase in the liner segment length ratio from zero to slightly over one. The former corresponds to a uniform (one-segment) liner. The length ratio of one corresponds to equal lengths of the liner segments. Total optimum suppression undergoes little change for the range of segment length ratios between 1.0 and 2.0. It appears to have reached its maximum ($\sim$ 36.0 dB) at the segment length ratio of about 1.0, i.e., for the two liner segments of equal lengths, as Table XIII indicates. Figure 78 shows that it is a broad suppression maximum and it extends from the point of length ratio (L_1/L_2) of 1.0 to about 1.25, at which the two liner segments have approximately the same resistance. For liner segment length ratio above about 1.25, total suppression decreases with the increase in the segment length ratio.

Within the considered range, up to the L_1/L_2 ratio of 2.0, the downstream liner segment suppression far exceeds that due to the upstream segment. Even at the highest considered ratio of 2, i.e., when the upstream liner segment is twice as long as the downstream segment, over twice as much predicted suppression is due to the latter ($\sim$ 24 dB) as that to the former ($\sim$ 10 dB). The suppression due to the upstream liner segment increases very moderately with increase in its length at the expense of the length of the

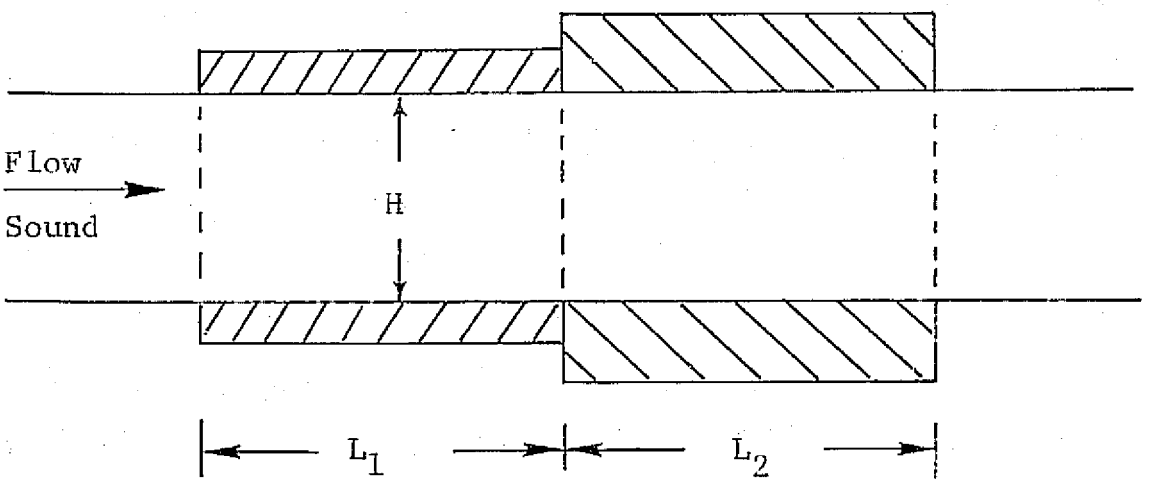

f = 2000 Hz
M = 0.3
L = L_1+L_2 = 91.44cm (36 In.)
H = 26.67cm (10.5 In.)
H/λ = 1.535

Figure 76. Schematic View of the Rectangular Duct in Studies of Segment Length Ratio Effect.

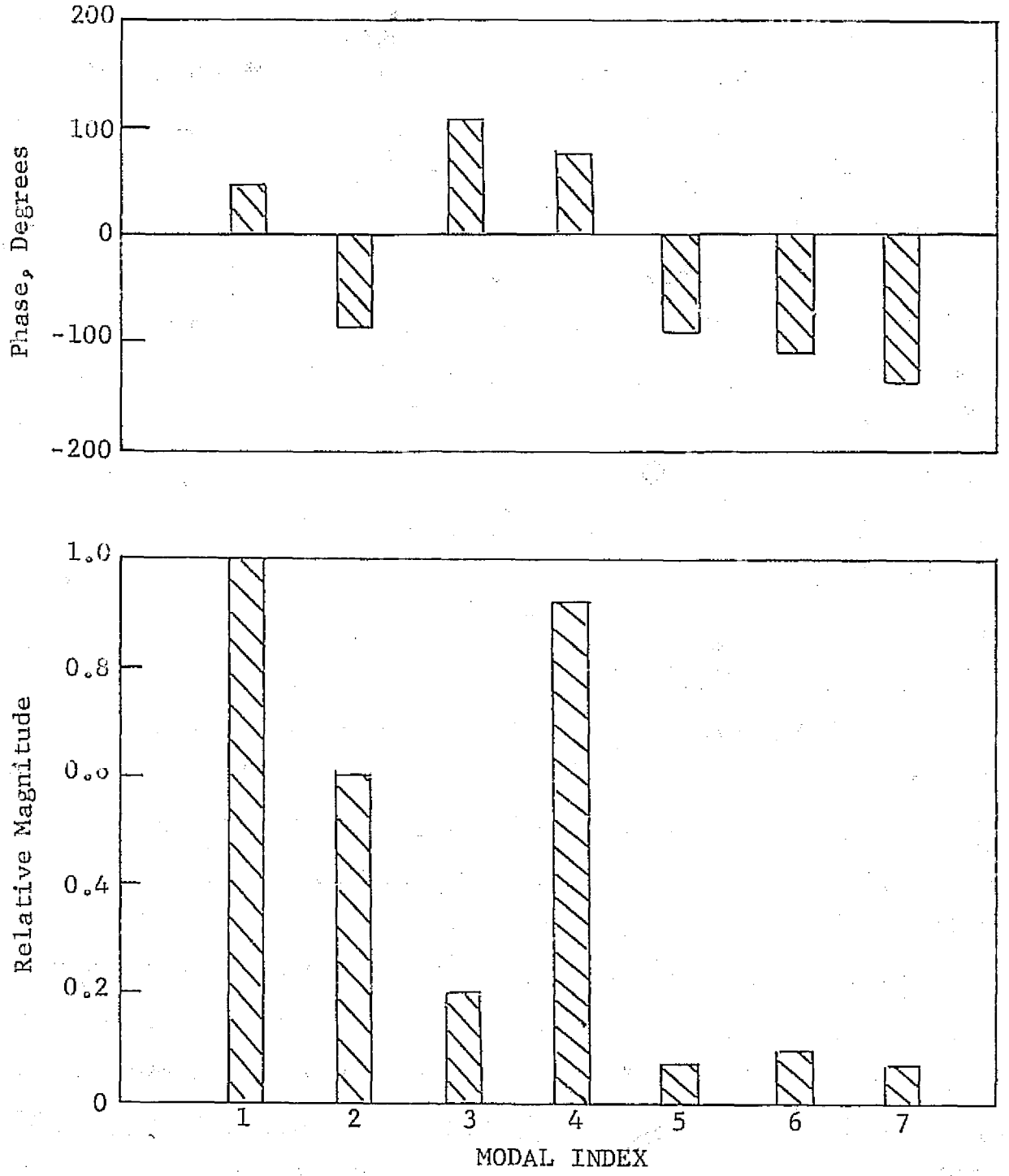

Figure 77. Source Modal Coefficients used in the Studies of Liner Segment Length Ratio Effect.

Table XIII. Calculated Effect of Liner Segment Length Ratio Variation.

$L_1+L_2 = L = 91.44cm$ (36 Inches)

$M = 0.3$

$H/\lambda = 1.535$

$L/H = 3.43$

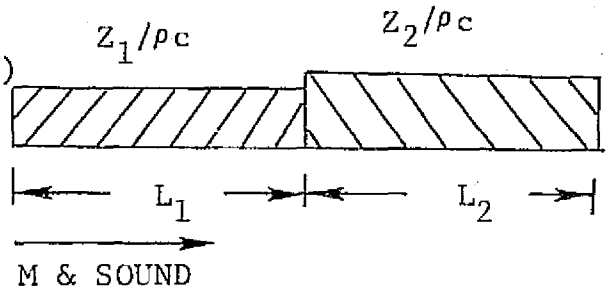

L_1/L_2	$Z_1/\rho c$	$Z_2/\rho c$	$-\Delta dB_1$	$-\Delta dB_2$	$-\Delta dB$
0*	.90 -1.0i	.90 -1.0i	-	-	21.6
1/7	.04 -0.9i	.75 -0.87i	0.2	28.0	28.2
1/3	.17 -1.17i	.75 -0.77i	1.2	29.9	31.1
1/2	.30 -1.20i	.75 -0.68i	2.8	29.6	32.4
1/1	.60 -1.20i	.70 -0.5i	7.0	28.9	35.9
2/1	.77 -1.17i	.60 -0.42i	10.4	23.9	34.3

* Uniform Liner

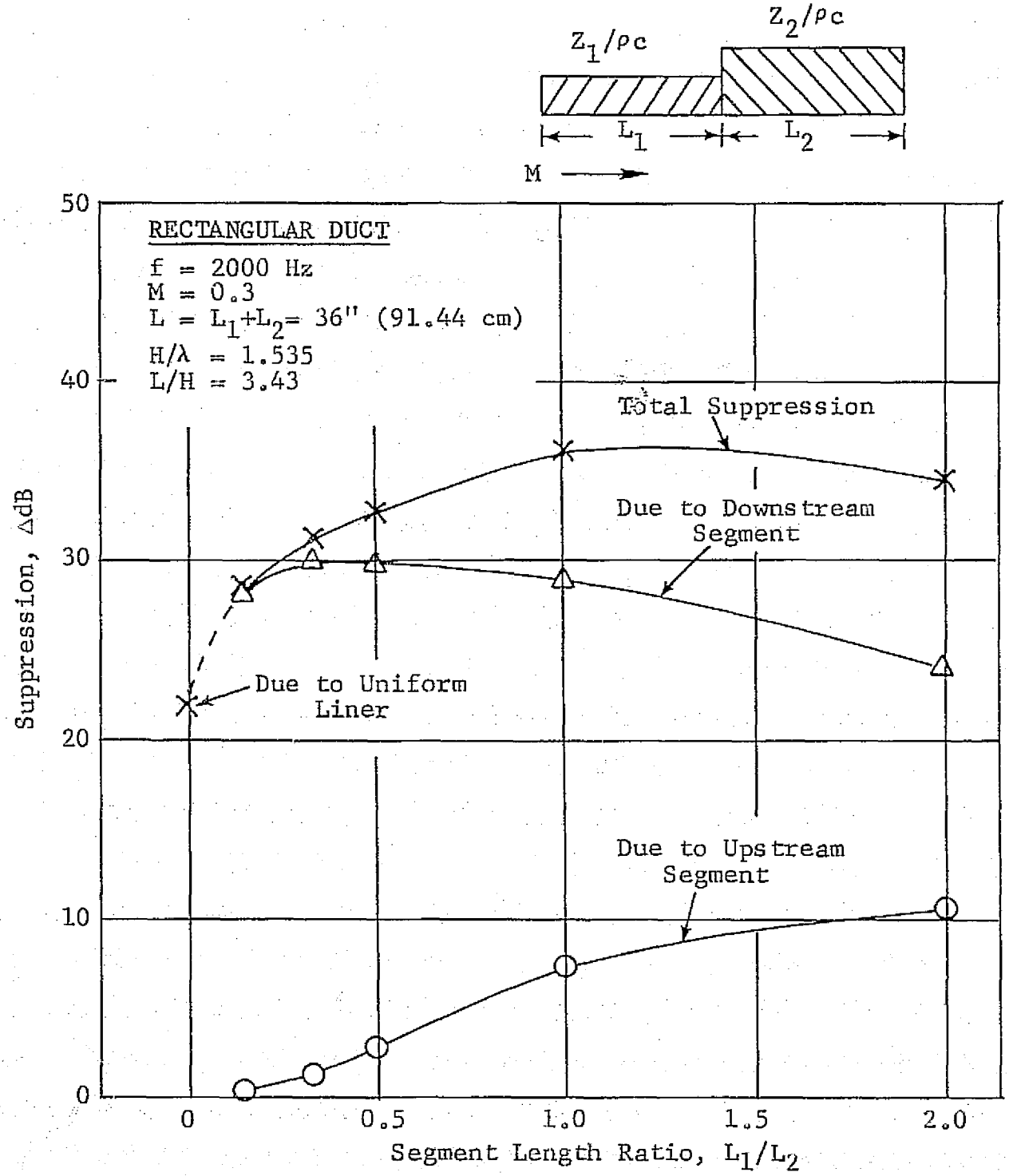

Figure 78. Predicted Effect of Liner Segment Length Ratio on Optimum Sound Suppression.

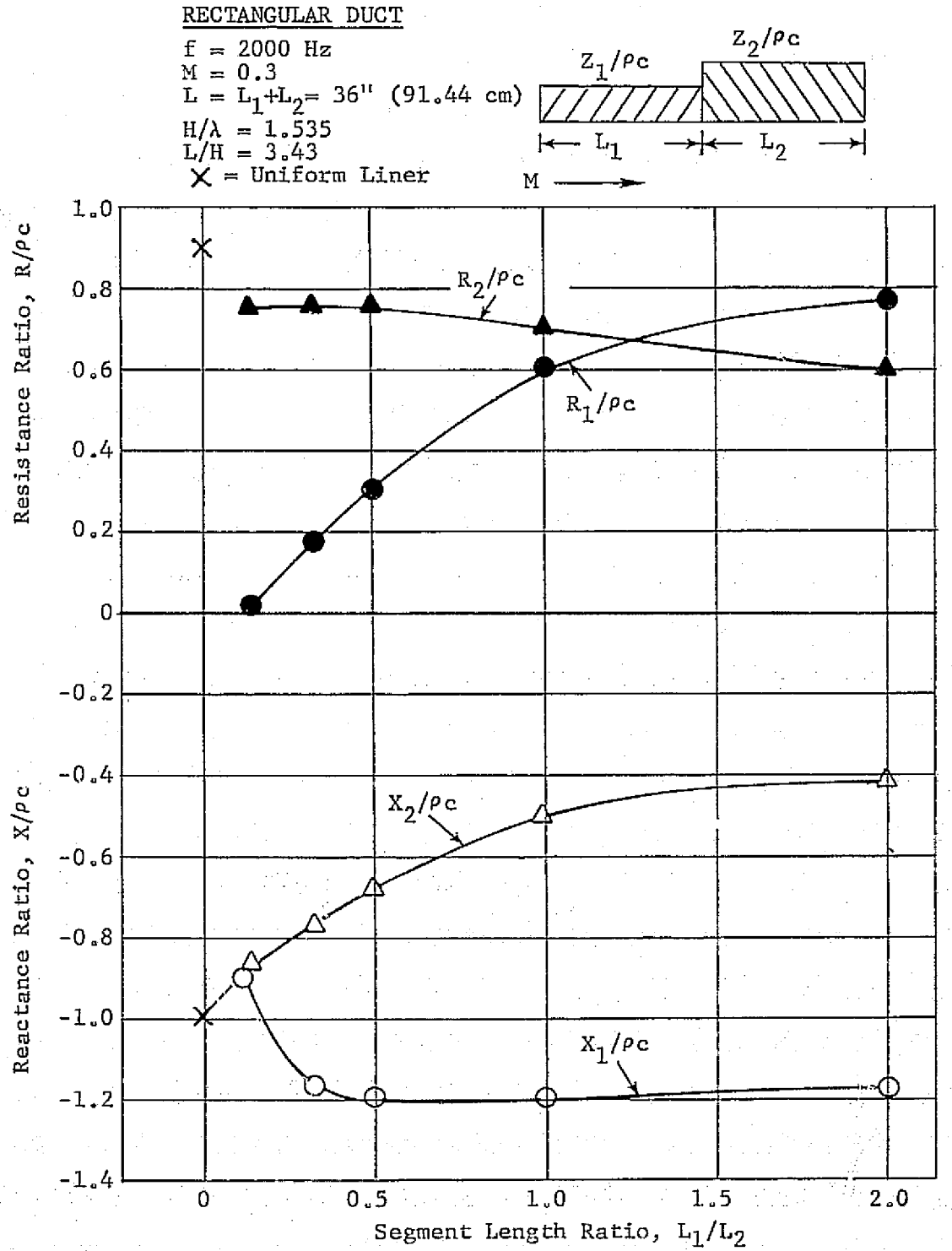

Figure 79. Predicted Effect of Liner Segment Length Ratio on the Optimized Impedance Ratio Components of the Two Liner Segments.

downstream segment. In contrast, the suppression due to the downstream liner segment increases rapidly as the single-phase liner is replaced with the two-element treatment, even though the first (upstream) element constitutes only one-seventh of the length of the downstream liner segment. That increase continues until the upstream segment length is about 25% of the total treatment length, i.e., is about one-third as long as the downstream liner panel.

The optimized liner segment resistance and reactance ratios are shown graphically in Figure 79. The optimized reactances of both liner segments are negative for the considered segment length ratios. The optimum resistance of the upstream segment increases with its length, i.e., with the increase of the L_1/L_2 ratio. The optimum resistance of the downstream segment decreases very moderately with the decrease in its length (L_2), i.e., with the increase in the L_1/L_2 ratio. The two resistance curves intersect at an L_1/L_2 ratio of about 1.25. As already mentioned, this resistance value appears to be quite close to the maximum suppression of the two-element treatment at the considered conditions.

The optimum reactance ratio of the upstream segment is larger, in absolute value, than the corresponding reactance ratio of the downstream panel. This indicates a smaller core depth for the upstream liner segment than that for the downstream segment in an optimized two-phase liner configuration.

SECTION 6.0

CONCLUSIONS

An analysis for calculating the propagation of acoustic waves in rectangular flow ducts has been developed to be used in conjunction with in-duct modal measurements. The method has been used to design and test a two-element optimized treatment configuration.

It has been shown that duct acoustic modes can be measured successfully in engine environment flow and sound conditions, and used to accurately predict sound attenuation for various treatment configurations in the presence of many modes. Of the five treatment configurations tested, the prediction was quite close for two cases, but an undetermined source of error caused overpredictions in the other three.

The discrete frequency optimum liner designs were found to possess very narrow suppression peaks, being quite sensitive to variations in impedance components or modal content. This is true for both single-element and two-element optimum treatment designs. The sensitivity to impedance components and modal content implies a strong dependence of peak suppression on frequency variations, as well. At the design Mach number, the measured third-octave suppression data for Configurations 4 and 10, however, indicated an enhancement of broadband suppression for the two-element liner as compared with suppression bandwidth curves for single-element liners obtained by normal design procedures, but whether the enhancement was great enough to warrant using the two-element design for suppression at a single frequency is questionable.

The highest measured narrowband suppression came within 10 dB of the predicted optimum peak suppression of about 36 dB. The combined effects of changing source modal characteristics and the inability to precisely achieve optimum impedance components accounted for this difference. The two effects can be considered to contribute a roughly equal amount to the loss in peak suppression. The results of the sensitivity studies indicate that the prediction technique correlates well with the measured suppression within the uncertainty caused by expected errors in the impedance components. Thus, the analysis has been shown to be adequate for the purposes of analytical parametric studies.

The narrowband attenuation obtained for Configuration 10 is likely to be as close as the predicted discrete frequency optimum can be approached in practical cases. It will be quite difficult to achieve the predicted high suppressions within 5 to 10 dB due to the "sharpness" of the attenuation peaks near optimum, particularly at lower η values. In future studies, it will prove more useful to develop this approach for broadband suppression rather than refine the discrete frequency development.

The results of the analytical study indicate that the two-element liner offers enhanced suppression over a single-element liner with the same total length. The most practical use of this enhancement occurs over an approximate range of frequency parameter η (H/λ) from 1 to 5. For the considered conditions, the maximum increase in suppression for the two-segment treatment compared to the single-element treatment was predicted to occur at an η value of about 1.5. Analysis of the computer runs indicates that the primary two-phase mechanism causing the enhanced suppression at this η value is modal redistribution from one plane to the next. The effect of energy reflection at the interfaces is negligible.

Comparison of the experimental results for Configurations 7 and 8, with the same panels in reversed positions, indicate that the two liners do work in conjunction with one another. The design of the upstream treatment section is dependent on the design of the second; that is, one could not optimize the design of the first section for a given modal input, then use the output of the first section to optimize the design of the second section and expect to get the maximum suppression of both sections taken together. The optimization studies have indicated that several sequential iterations on both sections are necessary before the overall suppression converges to the peak value. The studies have indicated that, holding all other parameters except the two liner impedances constant, there is a unique set of the four impedance components which maximizes overall suppression.

Results of the analytical parametric studies have shown that maximum sound attentuation due to a two-segment liner of a given length depends upon the relative length of the liner segments. Optimum suppression increases with increase from zero to slightly over one in the ratio of the length of the upstream liner segment to that of the downstream segment. Maximum optimized suppression is attained at or slightly above the segment length ratio of 1.0, i.e., when the two liner segments are approximately of the same length. For the considered conditions, up to the L_1/L_2 ratio of 2, the downstream liner segment suppression by far exceeded the suppression due to the upstream segment.

The modal content of the duct source varies rapidly with frequency for pure tone excitation. Further investigation is needed to determine whether the change of the source modal content with frequency and in the presence of different treatment configurations was just a characteristic of the rectangular duct apparatus or whether it is of significance in engine ducts as well.

The analytical prediction procedure using measured modal content has been shown to be an adequate design device for discrete frequencies. In future studies, it is recommended that the method be adapted for predictions over a broadband range of frequencies. This would be of particular importance in investigating such effects as the enhanced high frequency two-element liner suppression measured in this study. It would be useful for the development of broadband treatment design criteria.

SECTION 7.0

REFERENCES

1. Nayfeh, A.H., Kaiser, J.E., and Telionis, D.P., "The Acoustics of Aircraft Engine Duct Systems", AIAA Paper No. 73-1153, October, 1973.

2. Yurkovich, R., "Attenuation of Acoustic Modes in Circular and Annular Ducts in the Presence of Uniform Flow", AIAA Paper No. 74-552, June, 1974.

3. Morse, P.M., and Ingard, U., Theoretical Acoustics, McGraw-Hill, New York (1968).

4. McCalla, Thomas Richard, Introduction to Numerical Methods and FORTRAN Programming, John Wiley & Sons, New York, 1967.

5. Zorumski, W.E., Mason, J.P., "Multiple Eigenvalues of Sound Absorbing Circular and Annular Ducts", Journal of the Acoustical Society of America, Vol. 55, No. 6, June, 1974.

6. Zorumski, W.E., "Acoustic Theory of Axisymmetric Multisectioned Ducts", NASA TR R-419, May 1974.

7. Morfey, C.L., "Sound Transmission and Generation in Ducts with Flow", J. Sound and Vibration, (1971) 14 (1), pp. 37-55.

8. Baumeister, Kenneth J., "Generalized Wave Envelope Analysis of Sound Propagation in Ducts With Stepped Noise Source Profiles and Variable Axial Impedance", AIAA Paper 75-518, Hampton, Virginia, 1975.

9. Groeneweg, John F., "Current Understanding of Helmholtz Resonator Arrays as Duct Boundary Conditions", NASA SP-207 (1969).

10. Armstrong, D.L., Beckemeyer, R.T., and Olsen, R.F., "Impedance Measurements of Acoustic Duct Liners With Grazing Flow", 87th Meeting ASA, New York, April 23-26, 1974.

11. Phillips, Bert, "Effects of High Wave Amplitude and Mean Flow on a Helmholts Resonator", NASA TMX-1582, May 1968.

12. Lester, H.C., and Posey, J.W., "Duct Liner Optimization for Turbomachinery Noise Sources", NASA TMX-72789, November 1975.

SECTION 8.0

LIST OF SYMBOLS

$A_m^{\pm}$	=	modal expansion coefficients
$\left\{A^{\pm j}\right\}$	=	modal solution vector at plane j
c	=	speed of sound in stationary medium
C_j	=	$A_j^+ + A_j^-$
$E_z^{\pm}(m,n)$	=	modal energy flux
f	=	frequency, Hz
F	=	general function
H	=	duct height
i	=	$\sqrt{-1}$
I_z	=	the axial component of the acoustic intensity vector
k	=	the wave number in free space
ℓ	=	liner cavity depth
M	=	axial flow Mach number
n	=	index indicating type of boundary condition
NM	=	number of transverse modes in the expansion
p(x,z,t)	=	the acoustic pressure at point (x,z) and time t
{Q}	=	the stacked modal source vector
R/ρc	=	resistance ratio
$R^{+(j+1)}$	=	reflection matrix at plane j + 1 of the forward traveling wave
S(ω,x)	=	cross-spectral density
[S]	=	the system matrix
t	=	time
t_p	=	face plate thickness
$\left[T^{+(j+1),+j}\right]$	=	transmission matrix from plane j to plane j + 1 for the forward propagating wave
U	=	mean flow velocity in the axial direction
[U]	=	uniform section transmission matrix

LIST OF SYMBOLS (Concluded)

v_z	=	axial component of acoustic velocity
x,z	=	Carthesian Coordinates in two-dimensions
$X/\rho c$	=	reactance ratio
$Z/\rho c$	=	impedance ratio
β	=	admittance ratio
γ_m	=	eigenvalue of the M-th transverse mode
δ	=	empirical liner hole end correction
δ_{IJ}	=	the Kronecker Delta
$\eta = H/\lambda$	=	duct height-to-wavelength ratio
$K_m^{\pm}$	=	axial propagation constant for the M-th mode
λ	=	wavelength
ρ, ρ_o	=	density of air
σ	=	faceplate open area ratio
σ_m	=	real part of propagation constant, m^{th} mode
τ_m	=	imaginary part of propagation constant, m^{th} mode
ϕ_m	=	M-th mode eigenfunction
$\{\phi^{\pm j}\}$	=	vector of eigenfunction at plane j
ω	=	$2\pi f$ = circular frequency
∇^2	=	the Laplacian Operator

Subscripts and Superscrits

j,j+1	=	axial station indices
m	=	transverse mode number
p	=	referring to probe
r	=	referring to reference microphone
T	=	designating a transpose matrix
$\pm$	=	superscript sign denoting the direction of wave propagation
*	=	designates complex conjugate
< >	=	brackets designating time average